FLOATING BARE TETHER

AS UPPER-ATMOSPHERE PROBE

Final Report for ESTEC Contract No. 17384/03/NL/LvH/bj

Juan R. Sanmartín
Mario Charro
Sergio Elaskar
Jesús Peláez
Ignacio Tinao

March 12, 2004

Prepared for:

Alain Hilgers
European Space Agency
ESTEC

Escuela Técnica Superior de Ingenieros Aeronáuticos
Universidad Politécnica de Madrid
Pl. Cardenal Cisneros, 3
28040 Madrid
Spain

FLOATING BARE TETHER AS UPPER-ATMOSPHERE PROBE

Final Report

J. R. Sanmartín

Mario Charro

Sergio Elaskar

Jesús Peláez

Ignacio Tinao

Introducción

Chapter

FLOATING BARE TETHER AS UPPER-ATMOSPHERE PROBE

FINAL REPORT

Introduction

This study purports to investigate whether a conductive tether left uninsulated and electrically floating in LEO could serve as an effective e-beam source to produce artificial auroras. Standard electron beams emitted from satellites are marred by satellite charging problems. Also, standard e-beams have small cross-sections (with radius about one electron-gyroradius at typical KeV energies) and require ground observation, which is made possible by a beam energy-flux two orders of magnitude greater than in the strong IBC Type-IV natural auroras. The strong flux compensates for the thinness of the emitting layer (10 m against, say, 10 km for natural auroras) but it results in gross beam distortions by nonlinear plasma effects. In addition, the gross perturbations produced by intense beam emission in the space plasma around the spacecraft affect emission itself, and the luminous glow arising from the electron bombardment in the return current contaminates sensitive optical instruments.

An electrically floating tether comes out biased highly negative over most of its length. Ambient ions impacting it with KeV energies liberate secondary electrons, which are locally accelerated through the 2D tether voltage-bias, race down magnetic lines, and result in peak auroral emissions at about 120-160 km altitude. Since no current flows at either tether end, a bare-tether e-beam is fully free of spacecraft charging problems. Also, the beam is free of plasma interaction effects: its very large cross section (about twice electron-gyroradius times tether length) results in energy flux over 10^3 times weaker than in standard beam sources. In addition, emission of such a weak flux has no significant effect on the local plasma, and takes place far from any instrument (*Martinez-Sanchez* and *Sanmartin*, J. Geophys. Research, 1997; *Sanmartin,*

Ahedo and *Martinez-Sanchez*, Proc. 7th Space. Charging Tech. Conf., 2001). Beyond auroral effects proper, a floating bare-tether could provide values of neutral density along its E-layer footprint track, of interest in full numerical simulations of the atmosphere lying below, and in orbit decay and reentry predictions. Central to this study will be the possible determination of the neutral-density vertical profile from emission brightness measurements.

The tether would operate at night-time, to ease observations, with both a power supply and a plasma contactor off for electrical floating. Since the current induced in the floating tether results in magnetic drag, long-time operation will require solar power; power and plasma contactor would be on at daytime so as to reverse the direction of current to produce thrust, reboosting the spacecraft once per orbit. A tether system might provide an autonomous, effective e-beam source for continuous observation of its E-layer emissions. Alternatively, an electric thruster might be used for reboost in order to uncouple tether design to optimize observations from cross-section considerations.

Conductive tethers are best deployed if being preceded by a low-tension non-metallic segment. For the present application, however, it might be convenient that the full tether be conductive; deployment under such condition and the dynamics of a tether thrusting in an upper segment and dragging in the rest (at daytime) need be considered. It must be ensured that the drag/thrust cycle, and the low currents attained during nighttime, make the tether not only stable against the skip-rope instability (recently discussed in the literature) but as straight as might be required by observational considerations.

Beam propagation and beam-atmosphere interactions need be modelled in a simple but quantitative way so as to allow a satisfactory discussion of observational options and their feasibility. The evolution in the energy spectrum of secondary

electrons, their pitch distribution, and beam broadening due to collisions with neutrals, which would result in a broader but weaker tether footprint in the E-layer, need be modelled. Relations between particle flux and energy values, and ionization and accompanying emission rates, must be considered. The dependence of E-layer emissions on plasma environment at the F-layer and on the (carefully preflight-calibrated) tether-yield of secondary electrons, as well as the short beam dwell-time at any atmospheric point, must be considered too.

In principle, ground observation could directly provide vertical resolution; sideways observation could be made continuous by using a cluster of 2-3 coorbiting microsatellites. However, the low flux reaching the emitting layer and the layer thinness result in very low luminosity and a signal masked in the night sky by a background energy flux of precipitating particles from a variety of sources, such as the continuous drizzle from the radiation belts. Phase-lock detection might possibly increase significantly the signal-to-noise ratio. Time-modulation of tether bias and current can be achieved through current control at the Hollow Cathode. The distributed capacitance in the tether-sheath would result in a pulse of bias, current, and emission of secondary electrons travelling along the tether, and the front of a luminosity wave moving horizontally in the E-layer. The dynamical effects of such pulses repeated at some frequency must be considered.

On the other hand, the large cross-section of the beam, with energy flux varying from tether top to bottom, could allow continuous observation from the spacecraft (for which luminosity is high) with high spectral and vertical resolution. Such observations are impracticable with the narrow standard e-beams. The use of tomographic techniques to provide the vertical structure of the neutral density need be considered. Luminosity will vary over the cross section of the footprint which would be 20-30 km wide in the

vertical plane containing the magnetic field (and 200 m thick horizontally accross, near the beam-range end) and subtends about six degrees from the tether, flying about 150 km above.

The energy flux in the beam, varying along the tether, should allow imaging line-of-sight integrated emissions, which mix effects from altitude-dependent neutral densities and from fluxes originating at different points in the tether. An iterative relaxation algorithm incorporating a priori information need be used to determine the density profile from line-of-sight luminosity measurements; convolution algorithms make for worse reconstruction when the set of lines is limited as here. Backscattering of emitted light from both lower atmosphere and Earth's surface should be weak because of the very short horizontal extent of our emitting region.

1 *Tether System Design* (WP-100)

1A *Tether design for minimum system mass*

1A.1 Introduction

Tether design is mainly concerned with geometrical considerations, searching for optimal values of tether length L_t, cross-section perimeter p, and conductive area A_c of the cross section, which depends on its shape. Tether material properties (density ρ_c, electrical conductivity σ, and yield of secondary electrons) offer little room for choice, the driver being a low value of the ρ_c/σ ratio, which leads to use of aluminum tethers. Considering how the distribution of a full system-mass among tether mass and top and bottom masses affects the Lorentz torque that drives the skip-rope instability is left to the second part of this chapter.

A variety of effects condition tether length and perimeter values. Both the auroral footprint at the E-layer and the maximum energy of secondary electrons, which determines beam penetration down the E-layer, scale like L_t. The initial beam width perpendicular to the vertical plane through the geomagnetic field is about twice the gyroradius of secondaries, which is proportional to square root of energy, and thus scales as $\sqrt{L_t}$. The particle flux in the beam and the column-integrated ionization rate are proportional to $p \times L_t$ and $p \times L_t^2$ respectively.

Values of p are limited by considerations of bare-tether electron collection at daytime. For a thin tape and the conditions of interest, OML collection requires $p/8$ not to exceed about 1 Debye length (*Sanmartin & Estes,* Phys. Plasmas, 1999), but current keeps close to its OML value for $p/8$ up to 2 Debye lengths (*Estes & Sanmartin,* Phys. Plasmas, 2000); for daytime electron temperature 0.15 eV and density $N_{ocd} = 10^6$ cm^{-3}, maximum p is about 46 mm. Tether length and perimeter affect the probability

of a cut by debris (much more probable, at the altitudes of interest, than micrometeroid cuts), which varies, in case of a wire, as $L_t/p^{1.4}$ roughly (*Flury & Klinkrad,* ESA WPP-081, 1994). Regarding the tether *strength/weight* ratio, the characteristic parameter is the length $L_c \equiv (\textit{ultimate strength} / 6 \times \textit{density})^{1/2} / \textit{orbit angular rate,}$ which is about 100 km for aluminum; one should have $\textit{tether mass} / \textit{full system mass} > (L_t/L_c)^2$, which is just a few per cent for $L_t = 20$ km (*Carroll,* Tethers in Space Handbook, 1997). The magnetic drag during night operation scales as $pL_t^{5/2}$ whereas air drag scales as just pL_t.

Whatever tether length and perimeter, the shape of the cross section, in particular the geometry of its conductive part of area A_c, affects the mass of the tether system critically. The three basic types of cross sections for bare tethers are round wire and tape (both fully conductive), and round wire conductive in a thin outer layer surrounding non-conductive material of cross-section area much larger than A_c. The ratio A_c/p, which will be found determinant in characterizing ohmic effects, can be much smaller for the last two types of cross sections.

For given p and L_t, the mass of a tape can be reduced by making it thinner. Too thin a tape, however, results in high ohmic resistance, and a massive power subsystem to push current through in producing tether-thrust at day operation; there might exist an optimal thickness that yields a minimum system mass. On the other hand, mass below that minimum might possibly be achieved by using the electric power to just feed Ion or Hall Thrusters, both because of greater efficiency and allowed use of thinner tapes. Again, however, too thin a tape might result in ohmic effects setting up at night, limiting the current of secondary electrons emitted and reducing auroral effects. Also, for sufficiently long missions the (relative) high consumption of propellant by electric thrusters might make their use prohibitive. All these issues are explored in the present

part 1A of this chapter. Where necessary in the analysis we shall take L_t = 20 km, and leave a discussion of L_t and p design values to section 1A.9.

1A.2 Tether drag at night operation

During operation at eclipse intervals in orbit, with both electric-contact device (Hollow Cathode) and power supply off, at the top A, the tether floats electrically, current vanishing at top and bottom (Fig.1). Electrons are collected above a zero-bias point B, and ions are collected below, following the OML law in either case. Each ion picks up an electron to leave as neutral; one may thus prefer to say that electrons leak out below B at the ion impacting rate. At the 1 kV bias range of interest, the leak rate is increased due to substantial secondary emission, with a yield γ_1 per unit bias of order 0.1 - 0.2 / kV per impacting ion.

The electron current I_e along the tether flows downwards everywhere, increasing from A to B and decreasing from B to bottom. The bias and current profiles are determined by equations

$$\frac{d\Delta V(h)}{dh} = -E_m + \frac{I_e(h)}{\sigma A_c}, \tag{1}$$

$$\frac{dI_e}{dh} = \frac{eN_{\infty n}p}{\pi}\sqrt{\frac{2e\Delta V}{m_e}}, \qquad (h < h_B) \tag{2a}$$

$$\frac{dI_e}{dh} = -\frac{eN_{\infty n}p}{\pi}\sqrt{\frac{2e|\Delta V|}{m_i}}\left[1 + \gamma_1|\Delta V|\right], \qquad (h > h_B) \tag{2b}$$

current and bias obeying conditions

$$I_e(0) = I_e(L_t) = 0, \qquad \Delta V(h_B) = 0.$$

Here $N_{\infty n}$ is night plasma density, and ΔV is local bias, which is the difference between tether potential Φ_t and undisturbed ionospheric-plasma potential Φ_p due to the induced electric field E_m, both in the tether frame (Fig.1).

Because the OML collection rate, being proportional to the inverse square root of particle mass, is low over most of the tether length, ohmic effects should be weak, a floating tether being near equipotential. Dropping the last term in Eq.(1) to set $\Delta V \approx E_m(h_B - h)$ allows direct integration of the equations, which yield

$$\frac{h_B}{L_t} \approx \left(\frac{m_e}{m_i}\right)^{1/3}\left[1+\frac{3}{5}\gamma_1 E_m L_t\right]^{2/3} \approx 0.039 \qquad (3)$$

for oxygen ions, $\gamma_1 = 0.15/\mathrm{KV}$, $E_m = 165$ V/km and $L_t = 20$ km. Point B lies near the top because of the large ion-to-electron mass ratio; in what follows the upper, positive bias segment in Fig.1 is ignored, setting $h_B \approx 0$. One readily finds

$$W_{drag}(night) \approx \left(\frac{1}{\gamma_1}+\frac{5}{7}E_m L_t\right) I_{emit}{}^{total}, \qquad (4)$$

with a secondary emission rate

$$\frac{dI_{emit}}{dh} \approx \frac{eN_{\infty n}p}{\pi}\sqrt{\frac{2eE_m h}{m_i}}\,\gamma_1 E_m h, \qquad I_{emit}(h = h_B \approx 0) = 0, \qquad (5)$$

yielding

$$I_{emit}{}^{total} \approx \frac{2}{5}\gamma_1 E_m L_t \,\frac{eN_{\infty n}pL_t}{\pi}\sqrt{\frac{2eE_m L_t}{m_i}}. \qquad (6)$$

1A.3 **Ohmic effects**

To solve for the current and voltage profiles if keeping the last term in Eq.(1), one introduces dimensionless variables standard in bare-tether analisys,

$$i \equiv \frac{I_e}{\sigma E_m A_c}, \qquad \phi \equiv \frac{\Delta V}{E_m L^*}, \qquad \xi \equiv \frac{h}{L^*}, \qquad (7a\text{-}c)$$

where σ is tether conductivity and L^* is a characteristic length gauging ohmic versus bare-tether collection impedances and defined by

$$\frac{eN_\infty pL^*}{\pi}\sqrt{\frac{2eE_mL^*}{m_e}} \equiv \frac{3}{4}\sigma E_m A_c, \qquad (8)$$

or

$$L^*(km) = 4.22\times\left(\frac{E_m}{100V/km}\right)^{1/3}\left(\frac{10^5\,cm^{-3}}{N_\infty}\frac{\sigma_c}{3.5\times10^7\,\Omega^{-1}m^{-1}}\frac{A_c/p}{0.1mm}\right)^{2/3} \qquad (8')$$

(*Sanmartin et al.*, J. Prop. Power -1993-). The ratio $L_t/L^* \equiv \tilde{L}_t$ is a fundamental dimensionless parameter for current and bias profiles along an electrodynamic bare tether. A large $\tilde{L}_t$ value means that ohmic effects are limiting the current in the tether (if due to electron collection). Equations (1) and (2a, b), where we set $\gamma_1 = 0$ for a simple estimate, become

$$d\phi/d\xi = i - 1, \qquad (1')$$

$$di/d\xi = \sqrt{\phi}\times 3/4, \qquad \xi < \xi_B, \qquad (2a')$$

$$di/d\xi = -\sqrt{m_e/m_i}\times\sqrt{|\phi|}\times 3/4, \qquad \xi > \xi_B. \qquad (2b')$$

Using again the conditions of zero current at both ends and zero bias at point B, one readily obtains from Eqs.(1') and (2a', b') relations

$$\phi^{3/2} + 2i - i^2 = 2i_B - i_B^2 = \phi_A^{3/2} \qquad \text{for} \quad \xi < \xi_B,$$

$$\sqrt{m_e/m_i}\times|\phi|^{3/2} + 2i - i^2 = \phi_A^{3/2} \qquad \text{for} \quad \xi > \xi_B$$

which, when used back in (1'), (2a', b'), determine $i(\xi)$. Finally one finds

$$\frac{L_t}{L_n^*} \equiv \tilde{L}_{tn} = \int_0^{\phi_A}\frac{d\phi}{\sqrt{1-\phi_A^{3/2}+\phi^{3/2}}} + \int_0^{\phi_A}\frac{(m_i/m_e)^{1/3}\,d\phi}{\sqrt{1-\phi_A^{3/2}+\phi^{3/2}}}, \qquad (9)$$

with L_n^* corresponding to night plasma density in (8'). The first and second integrals above are the ratios h_B/L_n^* and $(L_t - h_B)/L_n^*$ respectively; result (3) for the ratio h_B/L_t still holds approximately whatever the importance of ohmic effects.

Dropping the last term in (1) will be valid if that term is small at the point of maximum current, that is, for i_B small. This requires a small ϕ_A, Eq.(9) now yielding

$$\tilde{L}_{tn} \times (m_e / m_i)^{1/3} \approx \phi_A \times \left[1 + \phi_A{}^{3/2} \times 3/10\right].$$

The condition for ohmic effects to be negligible *at night* lies somewhere between requiring small values for $(m_e/m_i)^{1/3} \times \tilde{L}_{tn}$ and $0.3\sqrt{m_e/m_i} \times \tilde{L}_{tn}{}^{3/2}$. We will consider this issue in Sec.1A.6.

Equations (4), (6) are rewritten, for later use, as

$$\frac{W_{drag}(night)}{\sigma E_m{}^2 A_c L_t} = \frac{3}{10}\sqrt{\frac{m_e}{m_i}}\left(1 + \frac{5}{7}\gamma_1 E_m L_t\right)\tilde{L}_{tn}{}^{3/2}, \qquad (4')$$

$$\frac{I_{emit}{}^{total}}{\sigma E_m A_c} = \frac{3}{10}\sqrt{\frac{m_e}{m_i}}\,\gamma_1 E_m L_t\;\tilde{L}_{tn}{}^{3/2}. \qquad (6')$$

1A.4 **Tether drag and thrust at day**

At daytime, power supply and Hollow Cathode are on for partial current reversal. The zero-current and zero-bias points A and B move down. The electron current flows and increases upwards above A; it flows donwards below A, increasing from A to B and decreasing from B to the bottom (Fig.2). This is a new working set-up for electrodynamic tethers, raising some dynamical issues considered in part 1B of this chapter. A calculation of day drag is simple, however, if ohmic effects are still negligible.

Conditions below the zero-current point A in Fig.2 are then as in Fig.1, with just a scaling $L_t \rightarrow l$, and a consideration of changes in mass m_i of dominant ion species, induced electric field E_m, and plasma density N_∞. At F-layer altitudes ions are mostly oxygen at both night and day. Also, the (no center-offset) dipole-model of the

geomagnetic field shows moderate orbital variations of E_m for orbit inclinations reaching middle latitudes,

$$E_m = v_{orb}(a)\, B_{eq}(a) \cos i_m, \qquad |i_m - i_{orb}| < \textit{dipole tilt} \approx 11°,$$

where v_{orb} and B_{eq} are satellite speed and magnetic field at the magnetic equator, in a circular orbit of radius a; i_{orb} is the constant orbital inclination and i_m the magnetic inclination, which varies weakly on a daily basis.

On the other hand, plasma density variations are large, with typical night and day values $N_{\infty n} \sim 2 \times 10^5$ cm^{-3}, $N_{\infty d} \sim 10^6$ cm^{-3}. One then finds from Eq.(4)

$$\frac{W_{drag}(day)}{W_{drag}(night)} \approx \frac{N_{\infty d}}{N_{\infty n}} \left(\frac{l}{L_t}\right)^{5/2} \frac{1 + \frac{5}{7}\gamma_1 E_m\, l}{1 + \frac{5}{7}\gamma_1 E_m\, L_t} \equiv \alpha_w \left(\frac{l}{L_t}\right). \tag{10}$$

The condition of negligible ohmic effects *at day*, to be considered in section 1A.6, lies somewhere between requiring $(m_e/m_i)^{1/3} \times l/L_t \times \tilde{L}_{td}$ to be small and requiring $0.3\sqrt{m_e/m_i} \times (l/L_t)^{3/2} \times \tilde{L}_{td}^{\,3/2}$ to be small, with L_d^* corresponding to daytime density, making $\tilde{L}_{td} = \tilde{L}_{tn} \times (N_{\infty d}/N_{\infty n})^{2/3}$.

To determine the thrust above A, where conductive effects prove definitely important, variables (7a-c) are used in the bias and current laws. Using conditions $i_A = 0$, $\phi_A \approx 0$ (ignoring the segment AB), one readily finds a first relation for length ratio l/L_t and dimensionless bias at C,

$$\tilde{L}_{td}\left(1 - \frac{l}{L_t}\right) = \int_0^{\phi_C} \frac{d\phi}{\sqrt{1 + \phi^{3/2}}}, \qquad \phi_C \equiv \frac{\Delta V_C}{E_m\, L_d^*} \tag{11}$$

in terms of day value $\tilde{L}_{td}$. One also finds the supply power required at the top C,

$$W_e = I_C\, \Delta V_C = \sigma\, E_m^{\,2}\, A_C\, L^*{}_d \times i_C\, \phi_C \qquad (i_C = \sqrt{1 + \phi_C^{\,3/2}} - 1). \tag{12}$$

For the thrust power one readily finds

$$W_{thrust}(day) = \sigma {E_m}^2 A_c {L^*}_d \times \left[\phi_C - \int_0^{\phi_C} \frac{d\phi}{\sqrt{1+\phi^{3/2}}} \right], \tag{13}$$

resulting in a thrust efficiency

$$\eta_{teth} \equiv \frac{W_{thrust}(day)}{W_e} = \frac{\phi_C - \int_0^{\phi_C} d\phi / \sqrt{1+\phi^{3/2}}}{\phi_C \left(\sqrt{1+{\varphi_C}^{3/2}} - 1 \right)}. \tag{14}$$

The condition for day thrust to balance night and day drag is

$$r W_{thrust}(day) = \left[1 - r + r\alpha_w (l/L_t) \right] W_{drag}(night) \tag{15}$$

where r is the non-eclipse time fraction in orbit, providing a second equation for ϕ_C and l/L_t,

$$\frac{3}{10}\sqrt{\frac{m_e}{m_i}} \left[1 + \frac{5}{7}\gamma_1 E_m L_t \right] \times \left[\frac{1-r}{r} \frac{N_{\infty n}}{N_{\infty d}} + \left(\frac{l}{L_t} \right)^{5/2} \frac{7 + 5\gamma_1 E_m l}{7 + 5\gamma_1 E_m L_t} \right] \tilde{L}_{td}^{\,5/2} =$$

$$= \phi_C - \int_0^{\phi_C} \frac{d\phi}{\sqrt{1+\phi^{3/2}}}. \tag{16}$$

For given values of ion mass, night-to-day plasma density ratio $N_{\infty n}/N_{\infty d}$, yield of secondary electrons at full bias $\gamma_1 E_m L_t$, and non-eclipse time fraction, Eqs.(11) and (16) determine the thrusting length-fraction l/L_t and the dimensionless voltage at the power source, $\Delta V_C/E_m {L_d}^*$, as functions of the dimensionless tether length at day, $L_t/{L_d}^*$. Figure 3a shows $\Delta V_C/E_m {L_d}^*$ for oxygen ions, r = 0.6, $\gamma_1 E_m$ (= 0.15/kV × 0.165 kV/km) = 0.2475/km, L_t = 10 and 20 km, and $N_{\infty n}/N_{\infty d}$ = 0.1 and 0.3. Figure 3b shows corresponding values for l/L_t. We note that l/L_t (≈ 0.85) is nearly constant whereas ϕ_C is a rapidly increasing function of $L_t/{L_d}^* \equiv \tilde{L}_{td}$.

1A.5 System mass for short missions

Electrodynamic tethers use no propellant but consume expellant if using a Hollow Cathode as cathodic device; the consumption rate is very low, however. Values of mass-flow rates and electron currents in state-of-the-art Hollow Cathodes allow ascribing an equivalent "specific impulse" to ED-tethers in LEO that are over 10^2 (10^3) times greater than specific impulses of standard Ion Thrusters (chemical rockets). For limited operational times, a condition to be later discussed, one may ignore the expellant mass. The tether-system mass can then be written as made of mass related to the power subsystem and remaining hardware mass,

$$M \approx \alpha_t m_t + \beta W_e, \qquad (17)$$

tether-mass itself being

$$m_t = L_t \rho_c A_c (1 + \frac{\rho_{nc}}{\rho_c} \frac{A_{nc}}{A_c}),$$

with non-conductive cross section $A_{nc} = 0$ for the simple tape and wire cross sections, and $\rho_{nc}/\rho_c \approx 1/2.7$ for a cross section with thin outer layer if made of aluminum.

For later discussion on use of Ion Thrusters, M can be rewritten as

$$\frac{M}{\beta \sigma E_m^2 A_c L_t} = \frac{\alpha_t \rho_c}{\beta \sigma E_m^2} \left(1 + \frac{\rho_{nc}}{\rho_c} \frac{A_{nc}}{A_c}\right) + \frac{W_{thrust}(day)/\eta_{teth}}{\sigma E_m^2 A_c L_t}. \qquad (17')$$

It can further be rewritten by using Eq.(6') for I_{emit}^{total} and Eq.(12) for W_e,

$$\sqrt{\frac{m_e}{m_i}} \frac{\gamma_1}{\beta} \frac{3 N_{\infty n}}{10 N_{\infty d}} \times \frac{M}{I_{emit}^{total}} = \frac{\alpha_t \rho_c}{\beta \sigma E_m^2} \frac{1 + \rho_{nc} A_{nc} / \rho_c A_c}{\tilde{L}_{td}^{3/2}} + \phi_C \frac{\sqrt{1 + \phi_C^{3/2}} - 1}{\tilde{L}_{td}^{5/2}} \qquad (17'')$$

with $\phi_C(\tilde{L}_{td})$ taken from Eqs.(11) and (16). In the first term inside the bracket of (17") one has

$$\frac{\rho_c}{\sigma E_m^2} \approx 3.1 \frac{kg}{kw} \qquad \text{(for } Al \text{ and } E_m = 165 \text{ V/km)},$$

with β as low as (Fortescue and Stark, *Spacecraft Systems Engineering* -1995-, Martinez-Sanchez and Pollard, *J.Prop. Power* -1998-)

$$\beta \approx 5\frac{kg}{kw}\,(Hollow\ Cathode,\ Power\ \mathrm{Pr}ocessing\ Unit) + 15\,\frac{kg}{kw}\,(Solar\ array).$$

As regards the dimensionless coefficient α_t, which takes into account the masses of tether, end-mass/deployer and spacecraft itself, it is not possible to give definite values. Setting $\alpha_t \approx 4$ results in a value $\alpha_t\rho_c/\beta\sigma E_m^2 \approx 0.62$; in general, this dimensionless parameter would take values not far from unity.

1A.6 **Tether design for minimum system mass**

For given emitted current I_{emit}^{total} the mass of the system is determined by the right-hand-side of Eq.(17"), which is basically a function of $\tilde{L}_{td}$, shown in Figs.4a, b for $A_{nc} = 0$ (fully conductive round wires and tapes), two values of $\alpha_t\rho_c/\beta\sigma E_m^2$, and values of parameters $\gamma_1 E_m L_t$ and $(1 - r)N_{\infty n} / rN_{\infty d}$, determining $\phi_C(\tilde{L}_{td})$, as in Fig.3a. Table I gives additional results. Note that the mass of the system exhibits a minimum. At high enough $\tilde{L}_{td}$, the second term in the right-hand-side of (17"), which represents the mass of the power subsystem, is dominant; that term increases with $\tilde{L}_{td}$ because ϕ_C does increase very fast with $\tilde{L}_{td}$. At lower $\tilde{L}_{td}$, all other masses in the system, represented by the first term in the RHS of Eq.(17"), become dominant.

We now notice two important features of the minimum. First, it is very flat; this will allow some range of choices in design. Secondly, it occurs at high $\tilde{L}_{td}$, in the range 18-25 in the figures; it occurs at higher $\tilde{L}_{td}$ the higher $\alpha_t\rho_c/\beta\sigma E_m^2$ and the lower $\gamma_1 E_m L_t$ or $(1 - r)N_{\infty n} / rN_{\infty d}$. From Eq.(8') with $E_m = 165$ V/km, $N_{\infty d} = 10^6$ cm^{-3} and *Al* conductivity, one finds, for a tape,

$$\tilde{L}_{td} \approx 0.93 \times L_t(km) \times (0.2\,mm/\delta)^{2/3}.$$

This result also applies to a round wire of radius R if δ is replaced by R. A tape 20 km long, and a small fraction of millimiter thick, may reach values of $\tilde{L}_{td} \sim 20$, within the range for the mass minimum. Around the minimum, the mass of the power subsystem would be comparable to the set of all other masses; clearly, a tape very thin and thus having a large ohmic resistance requires a large solar array subsystem to carry current through, in producing enough thrust at day.

For the p values of tens of millimiters allowed by OML current collection, a $L_t \approx 20$ km, round wire would have $\tilde{L}_{td} << 20$, well to the left of the minimum; such tether would be much heavier than a tape of the same length and cross-section perimeter (and thus emitting the same secondary current); correspondingly, the tape system would be much lighter. We note, however, that a round wire of radius less than a millimeter and length scaled up appropriately could keep both the total emitted current and a value $\tilde{L}_{td} \sim 20$, and thus system mass. On the other hand, simple considerations show that neither the flux of secondary electrons emitted nor the energy of secondaries (and the size of the e-beam footprint at the E-layer) would be kept. The tape would produce greater flux but weaker energies (and smaller footprint).

As regards the third type of tether cross-section -a round wire only conductive in a thin outer layer- the basic difference with the tape case in Eq.(17") comes through the factor $(1 + \rho_{nc}A_{nc}/\rho_c A_c)$, which is equivalent to a large increase in the ratio $\alpha_t \rho_c / \beta \sigma E_m^2$. This results in the minimum mass occurring at a larger $\tilde{L}_{td}$, and that minimum mass being larger itself. From here on in this study we will only consider tape tethers.

For $\tilde{L}_{td} \approx 20$ and $L_t = 20$ km one has $L_d^* \approx 1$ km; with $E_m = 165$ V/km, $N_{\infty d} = 10^6$ cm^{-3} and *Al* conductivity, a length $L_d^* = 1$ km in Eq.(8') corresponds to a thickness $\delta = 0.18$ mm. In addition, values $r = 0.6$, $\gamma_1 = 0.15$/kV and $N_{\infty n} = 3 \times 10^5$ cm^{-3} lead to $\phi_C \approx 6.6$ at $\tilde{L}_{td} = 20$, and to an efficiency $\eta_{teth} \approx 0.17$ in Eq.(14). A value $\alpha_t \rho_c / \beta \sigma E_m^2 \approx 0.62$ then yields a ratio between the second and first terms in the RHS of (17"), $\beta W_e / \alpha_t m_t \approx 1.69$. A tape of width ($\approx p/2$), say, 12 mm would have a mass $m_t = 116.6$ kg, yielding for $\alpha_t = 4$, a hardware mass $\alpha_t m_t \approx$ 466.4 kg, a power-subsystem mass $\beta W_e \approx 789.9$ kg and a total mass M around 1256 kg ($\approx 10.8\ m_t$). The electric power required would be $W_e \approx 39.5$ kw at a voltage supply of 1.09 kV.

Regarding ohmic effects at day we note, for the preceding conditions, values

$$\left(\frac{m_e}{m_i}\right)^{1/3} \frac{l}{L_t} \tilde{L}_{td} \approx 0.552, \qquad 0.3 \sqrt{\frac{m_e}{m_i}} \left(\frac{l}{L_t}\right)^{3/2} \tilde{L}_{td}^{3/2} \approx 0.123.$$

Clearly, ohmic effects are not negligible as regards day drag, making Eq.(10) to overestimate $W_{drag}(day)$ and its use in Eq.(15) to overestimate $\phi_C(\tilde{L}_{td})$. Minimum mass would then correspond to somewhat thinner tapes. We also note, however, values

$$\left(\frac{m_e}{m_i}\right)^{1/3} \tilde{L}_{tn} \approx 0.291, \qquad 0.3 \sqrt{\frac{m_e}{m_i}} \tilde{L}_{tn}^{3/2} \approx 0.047.$$

This means that there are also (incipient) ohmic effects at night, with some reduction in the desired auroral effects; $\tilde{L}_{td}$ values around 20 thus correspond to *both* a minimum of system mass and some kind of threshold for ohmic effects on the beam of secondary electrons. Halving, say, tape thickness δ from 0.18 mm to 0.09 mm would strongly impair using a tether for auroral studies.

1A.7 **Day thrust by Ion thrusters**

We here consider whether the overall mass of the system could be reduced if the minimum-mass bare tape is used to just attain auroral effects by night, while an Ion thruster is used to provide thrust. An Ion thruster might require a lower power W_e if its (propulsive) efficiency η_{IT} is higher than the efficiency of that tape, $\eta_{teth} \approx 0.17$. A thinner tape would reduce M through the first term in Eq.(17) without impairing η_{IT} but it cannot be used because of the ohmic effects at night.

The electrical power required by an Ion Thruster is

$$W_e = \frac{Thrust \times v_{exh}}{2\eta_{IT}}, \tag{18}$$

where the exhaust velocity v_{exh} (*specific impulse* times *acceleration of gravity*) is about 30 km/s, and η_{IT} is typically 0.65 (Martinez-Sanchez and Pollard, *J.Prop. Power* - 1998). Since $Thrust \times v_{orb}$ must equal the required $W_{thrust}(day)$ there results an effective efficiency,

$$\eta_{IT}(eff) \equiv \frac{W_{thrust}(day)}{W_e} = 2\eta_{IT} \times v_{orb} / v_{exh} \approx 0.32, \tag{19}$$

which is definitely larger than $\eta_{teth} \approx 0.17$.

An Ion thruster could thus reduce M in (17), for the same $\delta = 0.18$ mm tape about optimal for bare-tether thrusting, through savings in the electrical power W_e due to an efficiency gain by the factor $0.32/0.17 \approx 1.88$. This gain would be somewhat reduced because the Ion thruster must produce greater $W_{thrust}(day)$ [day-drag would then act over the entire tether length: if using (10) in Eq.(15), $\alpha_w(1)$ should replace the value $\alpha_w(0.85)$ at the ratio $l/L_t \approx 0.85$ we found for the tape]. Also, the factor β (kg/kw) might need be taken greater if using the Ion Thruster (instead of just a Hollow Cathode for the tether if used for thrusting).

1A.8 System mass for long-missions

Balancing night and day drag with an Ion thruster becomes comparatively less convenient the longer the mission because of the extremely low expellant consumption in a Hollow Cathode. For long missions the mass of the system must be rewritten in the Ion Thruster case as

$$M = \alpha_t m_t + \beta W_e + (1+\alpha)\times \dot{m}_{prop} \times r\tau \tag{20}$$

where $\dot{m}_{prop}$ is the propellant mass flow rate, τ is the mission duration, and $\alpha \approx 0.2$ accounts for tankage and plumbing. Using Eq.(18), the last term in (20) amounts to an increase in the power term by a factor

$$1 + \frac{(1+\alpha) r \dot{m}_{prop} \tau}{\beta \times Thrust \times v_{exh}/2\eta_{IT}} \equiv 1 + \frac{\tau}{\tau_{IT}}. \tag{21}$$

Introducing the propulsive relation

$$Thrust = \dot{m}_{prop} \times v_{exh}$$

we find

$$\tau_{IT} = \frac{\beta v_{exh}^2}{2\eta_{IT}(1+\alpha) r} \approx 7.3 months. \tag{22}$$

For bare-tether thrusting with the 0.18 mm tape and W_e given by Eq.(12), the expression equivalent to (21) is

$$1 + \frac{(1+\alpha) r \dot{m}_{\exp} \tau}{\beta I_c E_m L_d^* \phi_c} \equiv 1 + \frac{\tau}{\tau_{teth}},$$

$$\tau_{teth} = \frac{\beta I_c B_n v_{orb} L_t \phi_c}{(1+\alpha) r \dot{m}_{\exp} \tilde{L}_{dt}},$$

where we wrote $E_m/v_{orb} = B_n$ (magnetic component perpendicular to the orbital plane $= B_{eq} \cos i_m$ for the dipole model). The ratio $I_c / \dot{m}_{\exp}$, which is the ratio of current to mass-flow-rate at the Hollow Cathode, is a charge-to-mass ratio; with state-of-the-art

technology, its value is the charge-to-mass ratio for singly ionized atoms of low atomic number. In LEO orbit we have

$$\frac{I_c}{\dot{m}_{\exp}} \times B_n \equiv \omega_{hc} \approx 350 s^{-1}.$$

For $\tilde{L}_{td} = 20$ ($\phi_c \approx 6.6$) we finally find

$$\tau_{teth} = \frac{\beta v_{orb} \times \omega_{hc} L_t}{(1+\alpha) r \times \tilde{L}_{td} / \phi_c} \approx 183 \; months . \qquad (23)$$

1A.9 **Conclusions**

Comparing Eqs.(22) and (23) for given intensity of auroral effects shows that, as soon as the auroral-probe mission reaches beyond, say, six months, use of the bare-tether itself for day-thrust will result in a system lighter than the system using electric propulsion for that purpose. A tape of thickness around 0.15 - 0.2 mm would then provide a minimum system-mass (for length 20 km). For shorter missions, Ion thrusters might result in somewhat lighter systems.

Regarding L_t design values, notice that $\tilde{L}_{td}$ scales as $L_t/\delta^{2/3}$ for tapes. Keeping the value $\tilde{L}_{td} \approx 20$ (corresponding to conditions about minimum M, and incipient ohmic effects at night) as L_t is varied, requires thickness δ to vary as $L_t^{3/2}$ and tether mass to scale as $L_t^{5/2}$. With W_{drag} scaling as $L_t^{5/2}$ too, total mass M will increase very fast with increasing tether length. This means that the range of design values for L_t is narrow (15 - 25 km) because, as already noticed, column-integrated ionization rates ($\sim L_t^2$) decrease rapidly with decreasing tether length.

As regards the perimeter p we note that all quantities of interest scale linearly with p as long as it is small enough to collect OML current ($p <$ 46 mm) but it is not so small as to dangerously increase the probability of cuts by debris (roughly varying as

$1/p^{1.4}$ as previously indicated). In particular, the mass of the $L_t = 20$ km, $\delta = 0.18$ mm tape considered in Sec.1A.6 could be cut in half from 116.6 kg to 58.3 kg by just halving the width ($\approx p/2$) from 12 mm to 6 mm, while keeping its optimal $\tilde{L}_{td} \approx 20$ value. Total system mass M and electrical power W_e would be halved to values 628 kg and 19.75 kw respectively, but column-integrated ionization rates would be halved too.

Finally, it would be worth carrying out a detailed analysis of the tradeoffs between use of an optimal tape, as considered in this study, and use of a very thin round-wire tether of length appropriately scaled up, as suggested in Sec.1A.6.

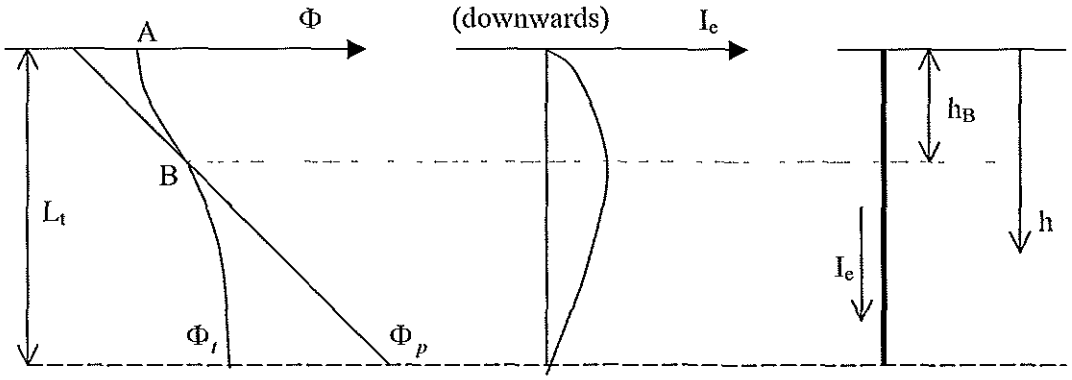

Fig. 1 Profiles of plasma potential and tether potential and current at night.

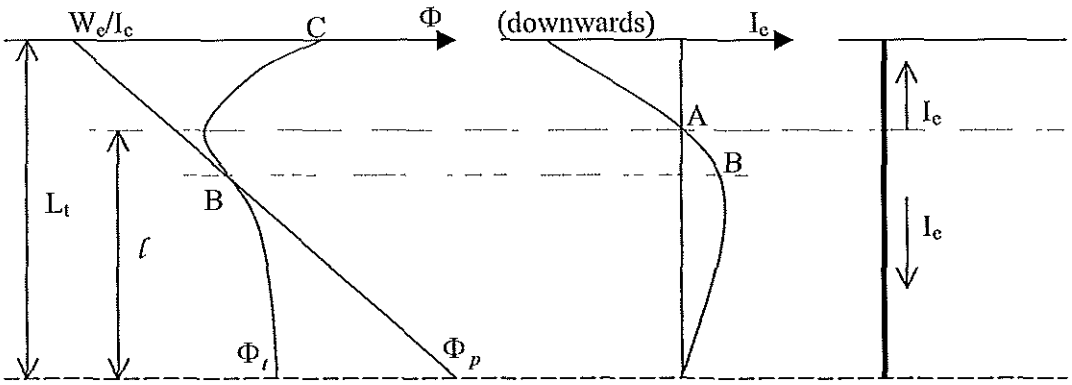

Fig. 2 Profiles of plasma potential and tether potential and current at daytime.

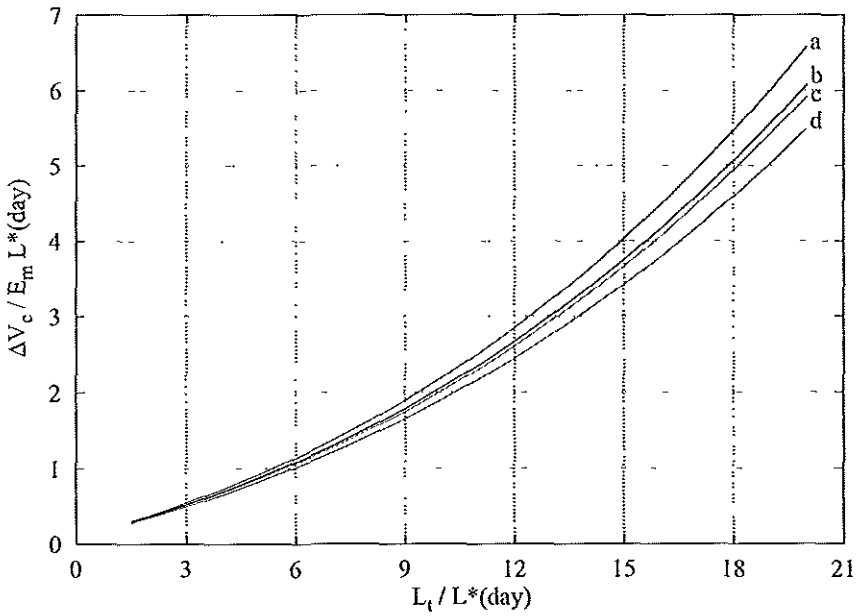

Fig. 3a E_m = 165 *V/km;* γ_1 : 0,15*/kV;* *eclipse time-fraction* = 0.4*; oxygen ions.*

a) $L_t = 20\ km$ - $N_{\infty n}/N_{\infty d} = 0.3$

b) $L_t = 10\ km$ - $N_{\infty n}/N_{\infty d} = 0.3$

c) $L_t = 20\ km$ - $N_{\infty n}/N_{\infty d} = 0.1$

d) $L_t = 10\ km$ - $N_{\infty n}/N_{\infty d} = 0.1$

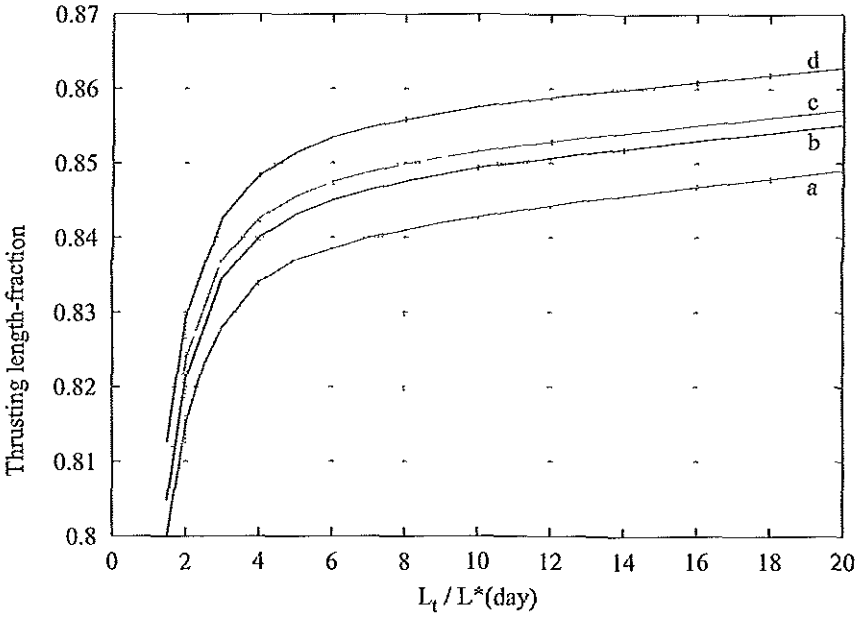

Fig 3b Parameter values as in Fig 3a

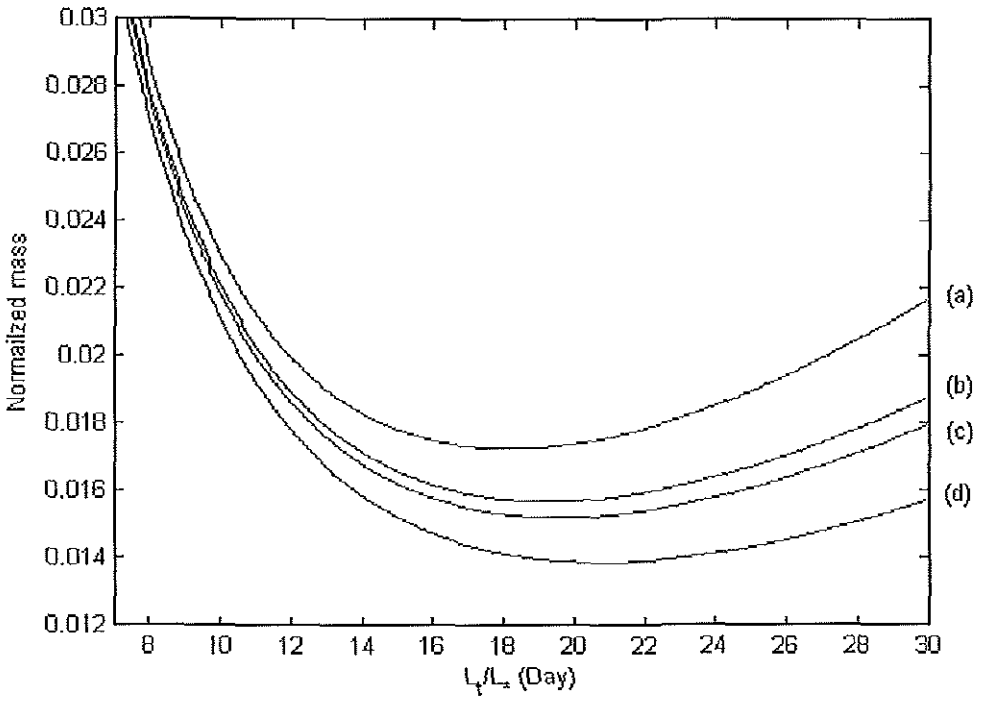

Fig. 4a Mass normalized as in equation (17''). Ratio $\alpha_t \rho_c / \beta\sigma E_m^{\,2} = 0.5$; other parameters as in Fig. 3a.

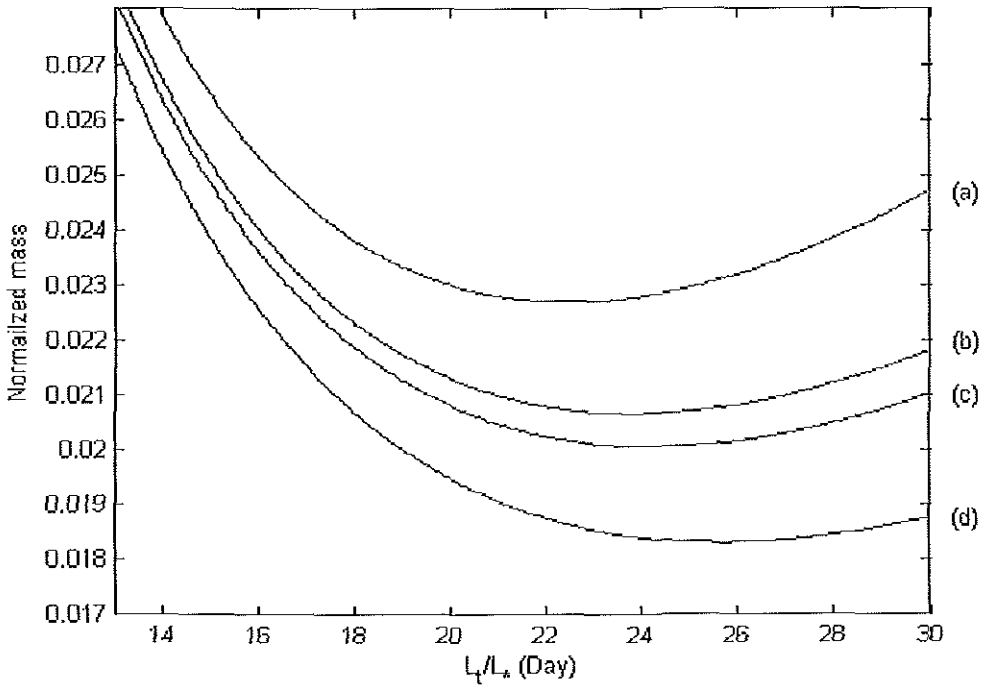

Fig.4b Ratio $\alpha_t \rho_c / \beta\sigma E_m^{\,2} = 1$; other parameters as in Fig. 3a.

$L_t / L_*(day)$	Thrusting length-fraction	$\frac{\Delta V_C}{E_m L_*(day)}$	Efficiency	Normalized mass
2	0.8476	0.3149	0.3834	0.2239
4	0.8480	0.6664	0.3610	0.0826
6	0.8486	1.0696	0.3340	0.0477
8	0.8493	1.5372	0.3063	0.0334
10	0.8501	2.0798	0.2793	0.0262
12	0.8509	2.7071	0.2540	0.0222
14	0.8518	3.4281	0.2307	0.0198
16	0.8526	4.2511	0.2096	0.0185
18	0.8535	5.1841	0.1906	0.0178
20	0.8544	6.2348	0.1736	0.0176
22	0.8553	7.4104	0.1584	0.0178
24	0.8562	8.7181	0.1448	0.0182
26	0.8571	10.1645	0.1327	0.0188
28	0.8580	11.7565	0.1219	0.0196
30	0.8589	13.5003	0.1123	0.0205

Ratio $\alpha_t \rho_c / \beta\sigma E_m^{\ 2} = 0.62$; $L_t = 20km$; $N_{\infty n} / N_{\infty d} = 0.2$.

Table I. Other parameters as in Fig. 3a.

1 *Tether System Design* (WP-100)

1B *Dynamical issues*

1B.1 Introduction

Dynamical issues for the eclipse and non-eclipse orbital phases are slightly different. The orbital motion of the system is not affected by dynamical instabilities. However, the electrodynamic torque would induce instability in the motion relative to the center of mass, as recently shown in the literature (see *Peláez et al.*, J. Astronaut. Sci., 2000). This instability will be more important during the daytime operation when the electrodynamic torque takes the highest values. An appropriate distribution of the masses of the system would largely help removing, or reducing substantially, the instability. In what follows, some general considerations of dynamic nature will be made, before undertaking a detailed analysis of the eclipse and non-eclipse orbital phases.

The weak electrodynamic forces acting on the tether in both phases permit to describe the tether dynamics using a dumbbell model. The upper mass, m_2, is assumed to be larger than the lower mass, m_1. The tether mass will be m_t. The center of mass G of the system follows a circular orbit. Its inclination is i_{orb}. Instead of values m_1, m_2, m_t, the mass geometry of the system is described in a better way with three different parameters M, ϕ_m, Λ_t. The total mass of the system is $M = m_1 + m_2 + m_t$, and $\Lambda_t = m_t/M$ is the fraction of the total mass due to the tether mass. Both end masses can be described using the parameter ϕ_m defined by relations

$$\cos^2\phi_m = \frac{1}{M}\{m_1 + \frac{1}{2}m_t\} \quad \Rightarrow \quad m_1 = M\left(\cos^2\phi_m - \frac{1}{2}\Lambda_t\right), \tag{24}$$

$$\sin^2\phi_m = \frac{1}{M}\{m_2 + \frac{1}{2}m_t\} \quad \Rightarrow \quad m_2 = M\left(\sin^2\phi_m - \frac{1}{2}\Lambda_t\right). \tag{25}$$

The maximum (minimum) possible values of ϕ_m corresponds to $m_1 = 0$ ($m_2 = 0$), respectively. Thus, $\phi_m \in [\phi_{min}, \phi_{max}]$, and the ends of this interval only depend on Λ_t

$$\phi_{min} = \arcsin(\sqrt{\frac{\Lambda_t}{2}}) \quad (m_2 = 0),$$
$$\phi_{max} = \arccos(\sqrt{\frac{\Lambda_t}{2}}) \quad (m_1 = 0).$$

If $\Lambda_t = 0$, $\phi_{min} = 0$ and $\phi_{max} = \pi/2$. For fixed values of Λ_t and M, when ϕ_m describes the interval $[\phi_{min}, \phi_{max}]$ from the lower to the upper end, mass is conceptually redistributed from the lower end to the upper one, with the total mass M constant in this process. For $\phi_m = \pi/4$, both end masses are equal.

The position of the center of mass G and the moment of inertia relative to an axis perpendicular to the tether through G are (see Fig. 5)

$$h_G = L_t \cos^2 \phi_m, \qquad I_s = \frac{1}{12} M L_t^2 (3 \sin^2 2\phi_m - 2\Lambda_t). \tag{26}$$

The main dynamic instability affecting electrodynamic tethers appears in the motion relative to the system center of mass G. The torque introduced by the electrodynamic forces on G is

$$M_e = u \times (u \times B) J_1, \qquad \text{where} \quad J_1 = \int_0^{L_t} (h_G - h) I_e(h) dh \tag{27}$$

B is the geomagnetic field and $I_e(h)$ is the tether current profile. Assuming a non-perturbed orbit for the system center of mass G, the equations governing the motion of the tether relative to the orbital frame $Gxyz$ are:

$$\ddot{\theta} - 2(1 + \dot{\theta})\dot{\varphi} \tan\varphi + \frac{3}{2} \sin 2\theta = -\varepsilon (\sin i_{orb} \tan\varphi \, h_1(\nu, \theta) + \cos i_{orb}) \tag{28}$$

$$\ddot{\varphi} + \frac{1}{2} \sin 2\varphi \left((1 + \dot{\theta})^2 + 3 \cos^2 \theta \right) = +\varepsilon \sin i_{orb} \, h_2(\nu, \theta) \tag{29}$$

Here, θ and φ (see Fig. 6) are the in-plane and out-of-plane angles, respectively, ν the true anomaly and h_1 and h_2 are auxiliary functions defined by:

$$h_1(\nu,\theta) = 2\,\sin\nu\cos\theta - \cos\nu\sin\theta$$

$$h_2(\nu,\theta) = 2\,\sin\nu\sin\theta + \cos\nu\cos\theta$$

The non-dimensional parameter

$$\varepsilon \equiv \frac{J_1}{I_s}\frac{\mu_m}{\mu_E} \tag{30}$$

gauges the electrodynamic torque versus the torque produced by the gravity gradient and the inertia forces. In (30), $\mu_E \approx 3.9860 \cdot 10^{14}$ m^3/s^2 is the Earth gravitational constant, $\mu_m \approx 8.097 \cdot 10^{15}$ Teslas m^3 represents the strength of the Earth magnetic dipole. I_s is the moment of inertia (26) and J_1 is defined in (27).

The instability we are considering here is characterized by the following facts (see *Peláez et al.*, J. Astronaut. Sci., 2000):

1. For each pair of values (ε, i_{orb}), an *unstable* basic periodic solution of equations (28-29) exists. Its period is the orbital one (2π in terms of the true anomaly ν)

2. For small values of ε, the largest unstable eigenvalue of the monodromy matrix of such a periodic solution has a modulus given by

$$\lambda_m = 1 + \frac{\pi}{9}\cos i_{orb}\,\sin^2 i_{orb}\,\varepsilon^3 + O(\varepsilon^4)$$

Thus, any initial deviation Δ from the basic 2π-periodic solution is roughly multiplied, in each orbit, by the growth factor

$$f_g = \frac{\pi}{9}\cos i_{orb}\,\sin^2 i_{orb}\,\varepsilon^3 + O(\varepsilon^4) \tag{31}$$

that is, after n orbits, the initial deviation becomes, approximately, $(1+f_g)^n\Delta \approx (1+nf_g)\Delta$. The growth factor (31) exhibits a cubic dependence on ε that must be emphasized. If, for example, ε decreases by a factor two, the instability declines by a factor eight. Thus, a design goal would be to reach values of ε as small as possible, within the limits imposed by the system.

Introducing L^* and the non-dimensional variables as defined in part 1A

$$\xi = \frac{h}{L^*}, \qquad i = \frac{I_e}{\sigma E_m A_c}, \qquad \tilde{L}_t = \frac{L_t}{L^*}$$

J_1 becomes

$$J_1 = \sigma E_m A_c (L^*)^2 \cdot \int_0^{\tilde{L}_t} (\tilde{L}_t \cos^2\phi_m - \xi)\, i(\xi)\, d\xi \tag{32}$$

The parameter ε can be written as

$$\varepsilon = \varepsilon_0 \cdot \hat{f} \tag{33}$$

where

$$\varepsilon_0 = \frac{E_m}{L_t} \frac{12\Lambda_t}{(3\sin^2 2\phi_m - 2\Lambda_t)} \cdot \frac{\mu_m}{\mu_E} \frac{\sigma}{\rho_c}, \tag{34}$$

$$\hat{f} = \int_0^{\tilde{L}_t} (\cos^2\phi_m - \frac{\xi}{\tilde{L}_t})\, i(\xi)\, \frac{d\xi}{\tilde{L}_t}. \tag{35}$$

The parameter ε has been split in two factors: ε_0 and $\hat{f}$. Apart from the ratio (μ_m/μ_E), the factor ε_0 depends on the tether material (σ/ρ_c), the mass distribution (through ϕ_m and Λ_t) and the ratio E_m/L_t. It takes values of order unity, except in the neighborhoods of the interval ends $[\phi_{min}, \phi_{max}]$.

Let us consider a tether made of a conductive tape with the following dimensions

$$\delta = 0.18 \text{ mm (thickness)}, \quad p_t \simeq 24 \text{ mm (perimeter)}, \quad L_t = 20 \text{ Km (length)} \tag{36}$$

Figure 7 shows the values of ε_0 as a function of ϕ_m for several values of Λ_t. To plot

this figure the following values have been used:

$$\sigma = 3.5 \cdot 10^7\ \Omega^{-1}\mathrm{m}^{-1}, \quad \rho_c = 2700\ \mathrm{Kg/m}^3, \quad E_m = 165\ \mathrm{V/Km}$$

which correspond to a tether made of aluminum. However, different configurations do not introduce substantial changes in the values of ε_0, which remains of order unity.

1B.2 Eclipse operation

Notice that $\hat{f}$ depends (see eq. (32)) on the mass angle ϕ_m and the non dimensional tether current $i(\xi)$, which must be obtained numerically following the analysis of Secs 1A.2 and 1A.3, and assuming that the tether keeps its straight form along the eclipse zone. This last point will be considered in detail later on in this document (see Sec 1B.7).

During the eclipse operation it is possible to get negligible values for $\hat{f}$, and therefore for ε, by selecting appropriately the mass distribution of the system. In fact, due to the small values of the current, the parameter $\hat{f}$ can be approximated by

$$\hat{f} = \sqrt{\frac{m_e}{m_i}}(\tilde{L}_{tn})^{\frac{3}{2}}\frac{3}{10}(1+\frac{5}{7}\gamma_1 E_m L_t)\left\{\cos^2\phi_m - \frac{5}{14}\frac{(1+\frac{7}{9}\gamma_1 E_m L_t)}{(1+\frac{5}{7}\gamma_1 E_m L_t)} + \mathcal{O}((\frac{m_e}{m_i})^{\frac{1}{3}})\right\} \quad (37)$$

where $\tilde{L}_{tn}$ is the nondimensional tether length calculated with the plasma density $N_{\infty n}$ at the eclipse zone of the orbit.

During the eclipse operation and due to the negligible influence of the ohmic effects, the parameter ε turns out to be proportional to the product

$$\sqrt{\frac{E_m L_t}{m_i}} \cdot \frac{N_{\infty n}}{\rho_c \delta} \quad (38)$$

for a given tape. To obtain this result, relation (37) has been considered. Notice that (38) involves m_i, but not m_e. This is due to ion collection taking place over almost

the entire tether length and playing an essential role in the process. In general, the destabilizing torque increases with $N_{\infty n}$ and with decreasing tape thickness.

However, the value of ϕ_m can be chosen, in a first approximation, to make $\hat{f} = 0$

$$\cos\phi_m^* \approx \sqrt{\frac{5}{14}\frac{(1+\frac{7}{9}\gamma_1 E_m L_t)}{(1+\frac{5}{7}\gamma_1 E_m L_t)}}. \tag{39}$$

This critical value leading to zero electrodynamic torque in G, only depends on the parameter $\gamma_1 E_m L_t$; it is independent of the plasma density, and almost independent of tether length. Figure 8 shows the variation of the critical value ϕ_m^* with $\gamma_1 E_m L_t$. It is almost constant, $\phi_m^* \simeq 53°$, when $\gamma_1 E_m L_t$ ranges in the interval $[0, 1]$.

Figure 9 shows the values of the factor $\hat{f}$, numerically calculated, for two tether lengths: 20 and 30 Km. For the first case, $\gamma_1 E_m L_t = 0.5$ and $\phi_m^* \approx 52.80°$. For the second one $\gamma_1 E_m L_t = 0.75$ and $\phi_m^* \approx 52.64°$. In both cases we used the values:

$$\gamma_1 = 0.15 \text{ KV}^{-1}, \quad E_m = 165 \text{ V/Km}$$

Notice that with these values and for the aluminum tape previously considered (see (36)), when the ionospheric plasma density at night, $N_{\infty n}$, ranges in the interval $[1,\ 3] \times 10^{11}$ m^{-3}, the characteristic length L^* ranges in the interval $[4.6, 2.2]$ Km. Therefore, in Fig. 9 the values of $\tilde{L}_{tn}$ are lower than, approximately, 10. Thus, in the region of interest, the values of $|\hat{f}|$ are smaller than, approximately, 0.009.

In fact, by selecting appropriately the lower mass, it is possible to reach values of $|\hat{f}|$ very small. For example, taking $\phi_m = 52°$, which is close to the critical values $\phi_m^* \approx 52.80° - 52.64°$, the values of $|\hat{f}|$ will be smaller than, approximately, 0.0004. In the case of the aluminum tape, this value, $\phi_m = 52°$, leads to a mass distribution as follows, for a total mass $M = 1000$ Kg:

$$m_2 = 563.5 \text{ Kg}, \quad m_1 = 321.6 \text{ Kg}, \quad m_t = 116.6 \text{ Kg}, \quad M = 1000 \text{ Kg} \tag{40}$$

For these particular values, and for a tether 20 Km long, we get

$$\varepsilon_0 \simeq 1.15$$

Thus, the parameter ε as a function of $\tilde{L}_{tn}$ takes values lower than, approximately, 0.0005. Taking into account the very small value of ε and the growth factor given by (31), the instability considered turns out to be extremely slow, that is, it needs a huge number of orbits to develop in this eclipse regime. The mass distribution selected, $\phi_m = 52°$, makes the electrodynamic forces acting on the tether equivalent to a drag force placed in G, the system center of mass.

For the mass distribution considered in Sec 1A.6 ($M = 1256$ Kg), this procedure provides slightly different values for the end masses: $m_2 = 721.6$ Kg, $m_1 = 417.8$ kg. However, these differences do not produce significant changes in the dynamical behaviour of the system. Thus, from the point of view of the night operation of the tether, the above used procedure removes this instability from the system.

1B.3 Non-eclipse operation

During the non-eclipse operation the tether is divided in two segments. In the upper one the electronic current flows upward and produces a thrust force on the system. In the lower segment the electronic current flows downward and produces a drag force (see Fig. 2 in Sec 1A). However, the electrodynamic torque is also given by equation (27). Notice that the value of ε_0 is not affected, but the factor J_1 and the non-dimensional parameter $\hat{f}$ takes very different values because of the tether current profile, which changes substantially. The structure of the non dimensional tether current profile, $i(\xi)$, is governed by the equations described in Sec 1A.4. Here, $i(\xi)$ will be *numerically* determined following the analysis of that section.

Equations (11) and (16) of Sec 1A.4 permit determine the parameters ϕ_C and ℓ/L_t. Through them, the entire structure of the electrodynamic forces depends on the parameters

$$\sqrt{\frac{m_e}{m_i}}, \quad \gamma_1 E_m L_t, \quad \tilde{L}_{td}, \quad \tilde{L}_{tn}, \quad r \tag{41}$$

In particular, the nondimensional electrodynamic torque $\varepsilon = \varepsilon_0 \hat{f}$. Figure 10 shows the numerical values reached by the factor $\hat{f}$ as function of the nondimensional tether length $\tilde{L}_{td}$, taking ϕ_m as a free parameter. Two cases have been considered: $N_{\infty n}/N_{\infty d} = 0.1$ in the upper picture, and $N_{\infty n}/N_{\infty d} = 0.3$ in the lower one.

During the diurnal operation, the current profile provides a torque that can not be balanced by any selection of ϕ_m. For the plasma density $N_{\infty d} \approx 10^{12}$ m^{-3}, the non dimensional tether length becomes $\tilde{L}_{td} \approx 20$. Therefore, the maximum value of $|\hat{f}|$ that can be expected in the range of nominal operation is about $|\hat{f}|_{max} = 0.065$. Taking the same mass distribution as in (40) the maximum value of the nondimensional electrodynamic torque ε is

$$\varepsilon_{max} = 1.15\hat{f} \approx 0.075$$

The associated growth factor given by (31) is $f_g \approx 1.5 \cdot 10^{-4} \cos i_{orb} \sin^2 i_{orb}$. Any initial deviation Δ from the basic 2π-periodic solution becoming approximately, $(1 + f_g)^n \Delta$, after n orbits, an increase in Δ by one order of magnitud, $\Delta \rightarrow 10\Delta$, takes approximately $n = \ln 10 / \ln(1 + f_g)$ orbits. For an orbital inclination $i_{orb} = 30°$ ($f_g \simeq 3.25 \cdot 10^{-5}$), n turns out to be $\simeq 71000$, that is, about 12 years in LEO.

However, electrodynamic tethers flying at inclined orbits have no equilibrium positions relative to the orbital frame. Therefore, the tether will oscillate continuously about the local vertical. Moreover, any small residual eccentricity of the circular orbit will help to self excite those oscillations. Thus, even though the dynamic in-

stability we had just considered will need a big number of orbits to develop, the oscillations of the tether could give place to out-of-plane angles φ not too small. Therefore, a realistic system dynamic simulation will be very convenient, in order to confirm these results.

1B.4 Tether deployment

To begin with the deployment of an electrodynamic tether, we will make some preliminary considerations related with the deployer system used. Thus, it is necessary to distinguish between a *motorized deployer*, as in the cases of TSS1 and TSS1-R, and a *passive deployer*, as in the case of SEDS. Both systems exhibit different characteristics that should be underlined.

Usually, the *motorized deployers* have an in-line thruster system on the end-mass side. Cold gas ejected in the direction of the tether could be a simple solution. The thruster system provides the steady force which is necessary to keep the tether straight while the motor turns the reel to unspool the tether. In these cases, the deployment takes place gradually and with low accelerations. The reason for that must be found in the spool where the tether is wound. Normally, it is big, and it turns out to be very difficult to accelerate it quickly. However, once the end satellite has reached enough distance, of the order of 2-3 Km, the gravity gradient becomes significant, and it can be used to replace the force produced by the in-line thruster system, which can be turned off. Probably, the combination *motorized reel + in-line thruster* is the most safe way of deploying *any kind* of tether. Notice that there are only two design parameters: 1) the force of the in-line thrusters (it depends on the friction of the deployer system and the bending stiffness of the wire), 2) the distance beyond which the in-line thrusters will be turned off. On the debit side of this kind

of deployment we find: 1) the cost of the global system increases due to the complex mechanism involved in the scheme, 2) usually, the system is much heavier and needs a more complex operation.

Passive deployers have much more complex running because there is no motor to help the tether out. In the more extreme case, the tether is unspooled with the help of a spring ejection system and the gravity gradient. This was the case of NASA SEDS missions, which flew successfully in the 90's, and the ProSEDS program, which finally has been terminated, following the Columbia accident. Such a combination, *passive deployer + spring ejection*, works well with very flexible tethers with extreme low friction. For example, in the cases of SEDS and ProSEDS, if during the first 5-10 minutes of the deployment the tension due to friction keeps greater than, approximately, 0.075 N, the tether would stop after roughly 750 m of deployed length.

An usual advice, in the tether-dynamics field, for deployment of an electrodynamic tethers, is to introduce a tether leader, about 3-4 Km long, very flexible and with very low friction. This way, when the metallic part begins to be deployed, the gravity gradient at the end mass would be high enough to overcome the larger friction created inside the deployer by the metallic (or conductive) wire. On the credit side, passive deployers exhibit a simpler operation and the global system is lighter.

Finally, there is an intermediate solution in which a passive deployer is used with an in-line thruster (like a gas canister) on the satellite side. Probably, this could become a good option for stiff metal tethers (aluminum or copper).

In that follows, our goal will be to analyze the deployment of the tether of this mission, using a passive deployer avoiding, if it is possible, the flexible leader.

1B.5 Deployment elementary analysis

In this section, we will consider a tether made of an aluminum tape 12 mm wide and 0.18 mm thick (its perimeter is about 24 mm). The masses of the system are given by the relation (40) and the tether will be 20 Km long, once deployed. We try to explore the conditions under which a passive deployer could be used to deploy the tether. The deployment takes place downwards.

The aim of the deployment phase must be to leave the tether aligned with the local vertical and at rest (relative to the orbital frame). Analysis of the deployment process of an electrodynamic tether can be found in the literature. For example, in (*J. Peláez*, Acta Astronautica, 1995), a procedure is carried out to deploy the tether when the satellite mass is negligible compared with the orbiter mass. It is based in an exponential law and it could be extended to be used in this case, when both end masses are of the same order of magnitude.

An important characteristic of the process should be underlined before facing the detailed analysis. The gravity gradient force has a component normal to the orbit which makes the orbital plane attractive during the deployment. Thus, assuming that the initial velocities of the end masses lie in the orbital plane, the whole process takes place in this plane.

Under this assumption, three phases can be distinguished, roughly, in the process. During the first phase, friction brakes the deployment and the gravity gradient grows. This phase ends when the radial velocity of the end mass reaches a minimum. In the second phase the gravity gradient becomes more importan than the friction, which is no longer able to stop the deployment. Finally, the deployment must be stopped

gradually at the end of the process, and this is the third and last phase.

Since the ratio $m_t/m_1 \approx 0.36$ is moderately small, the tether keeps straight during the deployment. This assumption has been *validated* in the deployment of SEDS-I and SEDS-II, for which the ratio was $m_t/m_1 \approx 0.26$. Moreover, the tension can be considered *uniform* along the tether and equal to the tension at the end attached to the orbiter.

Let v_{10} and v_{20} be the ejection velocities of the end masses m_1 and m_2, respectively, relative to the orbital frame. The spool with the wound tether is assumed to be part of the mass m_2. Thus, the momentum conservation provides the relation

$$m_1 v_{10} = (m_2 + m_t) v_{20}$$

The energy balance between the initial time and a generic instant for both end masses provides

$$\frac{1}{2} m_1 v_1^2 = \frac{1}{2} m_1 v_{10}^2 + \frac{3}{2} m_1 \omega^2 x_1^2 - \int_{t=0}^{t} T(t) dr_1 \tag{42}$$

$$\frac{1}{2} m_2 v_2^2 = \frac{1}{2} m_2 v_{20}^2 + \frac{3}{2} m_2 \omega^2 x_2^2 - \int_{t=0}^{t} T(t) dr_2 \tag{43}$$

where $T(t)$ is the tension, ω the orbital frequency and r_i the distances of both end masses from the system center of mass (see Fig. 6 for the coordinate x). In equation (43), the mass of the tether and deployer system has been neglected. This assumption introduces errors of the order of Λ_t ($\simeq 0.1$ in our case) which are conservative.

Assuming that the only source of tension is due to the deployer internal friction, the tension can be considered constant during the deployment process. In such a case, the tension T_{stop} that would result in stopping the deployment can be obtained by adding equations (42-43), giving

$$T_{stop} L_f = \frac{1}{2} \{ m_1 v_{10}^2 + m_2 v_{20}^2 \} + \frac{3}{2} \omega^2 L_f^2 \cos^2 \theta_f \{ m_1 \sin^4 \phi_m + m_2 \cos^4 \phi_m \} \tag{44}$$

where L_f is the deployed length and θ_f the in-plane angle at the end of deployment.

At the end of this partial deployment, equations (24-25) provide a value ϕ_f, different from the value ϕ_m for the full deployed tether; however, the difference is small if Λ_t is moderately small. For the tape of (36), $\Lambda_t \simeq 0.1$, and therefore we will take $\phi_f = \phi_m$ in this analysis. The approximation $\phi_f = \phi_m$ has been used in equation (44), that can be written as

$$T_{stop} L_f = \frac{1}{2} M v_{10}^2 \, F(\Lambda_t, \phi_m) + \frac{3}{2} M \omega^2 L_f^2 \cos^2 \theta_f \, G(\Lambda_t, \phi_m)$$

where F and G are positive definite functions which depend on the mass distribution of the system. They are given by

$$F(\Lambda_t, \phi_m) = \frac{m_1}{M}\left(1 + \frac{m_1 m_2}{(m_2 + m_t)^2}\right) \equiv (2\cos^2 \phi_m - \Lambda_t) \frac{\Lambda_t(\Lambda_t - 1) + 2(\Lambda_t + 1)\sin^2 \phi_m}{(\Lambda_t + 2\sin^2 \phi_m)^2}$$

$$G(\Lambda_t, \phi_m) = \frac{1}{M}(m_1 \sin^4 \phi_m + m_2 \cos^4 \phi_m) \equiv \frac{1}{8}\{1 - 3\Lambda_t(1 + \Lambda_t)\cos 4\phi_m\}$$

Introducing the non dimensional variables

$$\ell_f = \frac{\omega L_f}{v_{10}} \sqrt{\frac{G}{F}}, \qquad \lambda = \frac{T_{stop}}{\sqrt{3FG}\, M \omega v_{10}}$$

equation (44) takes the form

$$3\ell_f^2 \cos^2 \theta_f - 2\sqrt{3}\ell_f \lambda + 1 = 0 \tag{45}$$

For a given value of λ, equation (45) provides a curve in polar coordinates (ℓ_f, θ_f) inside the orbital plane. Such a curve is the locus of all possible positions where the deployment ends stopped by friction. Figure 11 shows this locus for different values of λ. Thus, when $\lambda > 1$ the locus is a closed curve encircling the origin, and the deployment will be stopped by friction *for all ejection conditions*. However, when $\lambda < 1$ the locus becomes an open curve, and it is possible to carry out the deployment of the tether (it must be close to the vertical if $1 - \lambda$ is small).

The limit $\lambda = 1$ provides

$$T^+_{stop} = \sqrt{3FG}M\omega v_{10}, \qquad L_f < L^+_f = \frac{v_{10}}{\omega}\sqrt{\frac{F}{3G}} \tag{46}$$

and can be used to obtain a fair estimation of the *maximum friction* which can be permitted in a passive deployer for a given ejection velocity (if $L^+_f < L_t$). The value L^+_f is the *maximum deployed length* which can be expected in this partial deployment. For a given initial ejection velocity v_{10}, if the tension produced by deployer friction is greater than T^+_{stop}, the tether can not be deployed with this system; to deploy the tether it would be necessary to change the passive deployer or to increase the ejection velocity.

Obviously, the deployment will be facilitated if T^+_{stop} takes the greatest possible value. For a given tether, by fixing v_{10} and M, the tension T^+_{stop} turns out to be a function of ϕ_m. Figure 12 shows the function $T^+_{stop} = T^+_{stop}(\phi_m)$, taking ϕ_m as a free parameter, in two cases: for the aluminum tape of (36) and for the SEDS deployer (data taken from table 1). The two first curves correspond to an ejection velocity of $v_{10} = 1$ m/s for both tethers; they show that: 1) it is easier to deploy light tethers, 2) there is an optimum value of ϕ_m which leads to a maximum of T^+_{stop}.

	M	m_t	ω
SEDS deployer	932.6 Kg	6.6 Kg	$1.17 \cdot 10^{-3}$ s^{-1}
Aluminum tape of (40)	1000.0 Kg	116.6 Kg	$1.158 \cdot 10^{-3}$ s^{-1}

Table 1: Data for SEDS deployer and the aluminum tape

The figure also shows the function $T^+_{stop} = T^+_{stop}(\phi_m)$ for the real ejection velocity used in SEDS, $v_{10} \approx 1.5$ m/s. The point A of the figure, which correspond to

$$\phi_m \approx 80°, \qquad T^+_{stop} \approx 80 \text{ mN}, \qquad L^+_f \approx 761 \text{ m}$$

is provided by relations (46) taking into account the masses actually used $m_1 \approx 26$ kg, $m_2 \approx 900$ kg, in SEDS missions.

For the aluminum tape considered in Eq. (40), $m_1 = 321.6$ Kg, $m_2 = 563.5$ Kg and assuming an ejection velocity $v_{10} \approx 0.25$ m/s (conservative), relations (46) provide

$$\phi_m \approx 52^\circ, \qquad T^+_{stop} \approx 0.15 \text{ N}, \qquad L^+_f \approx 184 \text{ m}$$

(point B of Fig. 12). From the dynamic point of view, the selected mass distribution, $\phi_m \approx 52^\circ$, helps to deploy the tether, making the critical value T^+_{stop} larger and more sensitive to the variations of the ejection velocity v_{10}.

Thus, taking a conservative position, if friction inside the deployer provides a tension which is roughly lower than 0.15 N (with the appropriate safety factor), it will not be necessary to introduce the leader segment in the tether. Otherwise, using a passive deployer will require a leader segment.

1B.6 Residual stresses

For a tether aligned with the local vertical and at rest, the maximum tension appears in the system center of mass G and takes the value

$$T_M = \frac{3}{4}\frac{M\mu_E}{a^3} L \sin^2 2\phi_m (1 - \frac{\Lambda_t}{2}) \tag{47}$$

At the tethers ends the values of the tension are

$$T_1 = \frac{3}{4}\frac{M\mu_E}{a^3} L \left\{\sin^2 2\phi_m - 2\Lambda_t \sin^2 \phi_m\right\}, \tag{48}$$

$$T_2 = \frac{3}{4}\frac{M\mu_E}{a^3} L \left\{\sin^2 2\phi_m - 2\Lambda_t \cos^2 \phi_m\right\}. \tag{49}$$

When Λ_t is small, T_M, T_1 and T_2 are very close. Thus, for the tape considered in (36) they take the values

$$T_1 \approx 16.09 \text{ N}, \quad T_2 \approx 17.21 \text{ N}, \quad T_M \approx 17.88 \text{ N}$$

When a tether is reeled out during deployment it retains *residual stresses*, specially if it has spent a long time wrapped on a reel. These residual stresses depend, usually, on the bending stiffness of the wire. Let T be the tension of a tether completely deployed. The tether bending stiffness[1] EI will affect the form of the wire if the deployed length is of the order of $l_B \approx \sqrt{EI/T}$ (see *A. H. von Flotow*, J. Guidance, 1988). For the aluminum tape we are considering

$$E = 70.3\times10^9 \text{ N/m}^2, \quad I = \frac{1}{12}(\frac{p}{2}-\delta)\delta^3 \approx 5.74\times10^{-15} \text{ m}^4 \quad \Rightarrow \quad EI \approx 4.1\cdot10^2 \text{ N mm}^2$$

Assuming $T \sim 1$ N, (very conservative), the length l_B turns out to be $l_B \sim 2$ cm. Thus, for the deployed tether with lengths of the order of Km the effects of the bending stiffness is insignificant.

However, the residual stresses could affect the initial phase of the deployment. Let R_r be the radius of the reel from which the tether will be deployed. Due to residual stresses, the tether will tend to take the form of a circumference of radius $R > R_r$, and the gravity gradient will tend to straighten it (to increase R). The bending torque due to residual stresses is

$$M_B = \frac{EI}{R}$$

Associated to M_B a shearing force appears which usually is modeled as

$$F_s = \frac{EI}{RL}$$

where L is the tether length. In the first stage of deployment L is small and F_s takes values greater than the tether tension (47) produced by the gravity gradient. The ratio F_s/T_M satisfies the relation

$$\frac{F_s}{T_M} \leq \frac{k}{L^2}, \qquad k = \frac{4EIa^3}{3R_r M\mu_E \sin^2 2\phi_m(1-\frac{\Lambda_t}{2})} \tag{50}$$

[1]In this paragraph I stands for the moment of inertia of the tether cross section; it is not the tether current

For the tape we are considering, and taking R_r as small as $R_r = 10$ cm the value of k is $k \approx 4.6$ m^2. As a consequence, the effects of the residual stresses are limited to a few seconds at the very beginning of the deployment, that is, when the deployed length is smaller than ≈ 5 m.

1B.7 Tether straightness

During the eclipse operation it would be convenient that the tether keeps as straight as possible. For an inert tether, i.e., when no current flows in the wire, the librational motion does not produce change of the rectilinear form of the tether (for the sake of simplicity we neglect the aerodynamic drag acting on the tether in LEO orbits). But when the tether current is different from zero, the transversal electrodynamic forces acting on the tether will excite its lateral deflection, and the tether will no longer keep its straight form. Here, we will try to roughly estimate the order of magnitude of such a deflection.

First of all, during the eclipse operation the electrodynamic forces acting on the tether are equivalent to a unique force $\boldsymbol{D}_e$ just applied in the center of mass G of the system. This result is a consequence of the selection made for the angle $\phi_m \approx 52°$, which leads to zero electrodynamic torque on the center of mass G. The value of the electrodynamic drag $\boldsymbol{D}_e$ is

$$\boldsymbol{D}_e = (\boldsymbol{u} \times \boldsymbol{B})\, \sigma E_m A_c L_t \, \frac{1}{\tilde{L}_{tn}} \int_0^{\tilde{L}_{tn}} i(\xi) d\xi \tag{51}$$

where $\boldsymbol{u}$ is a unit vector along the tether (in the upward direction), $\boldsymbol{B}$ is the Earth magnetic field, and $i(\xi)$ the non dimensional current profile. The integral on the right hand side of (51) is given by

$$\frac{1}{\tilde{L}_{tn}} \int_0^{\tilde{L}_{tn}} i(\xi) d\xi = \sqrt{\frac{m_e}{m_i}} (\tilde{L}_{tn})^{\frac{3}{2}} \frac{3}{10} (1 + \frac{5}{7} \gamma_1 E_m L_t) \left\{ 1 + \mathcal{O}((\frac{m_e}{m_i})^{\frac{2}{3}}) \right\} \tag{52}$$

and the cross product $\boldsymbol{u} \times \boldsymbol{B}$ turns out to be

$$\boldsymbol{u} \times \boldsymbol{B} = \frac{\mu_m}{a^3} \boldsymbol{z}$$

where the vector $\boldsymbol{z}$ depends in a complex way of the libration angles θ and φ, the true anomaly ν along the orbit and the orbital inclination. However, when the tether is aligned with the local vertical, it always fulfills the relation $\cos i_{orb} \leq |\boldsymbol{z}| \leq 1$.

To clarify the effects of this force, it is enlightening to compare it with the maximum tether tension, which appears in the system center of mass when the tether is aligned with the local vertical. Such a tension is given by (47), and the ratio turns out to be

$$\frac{|\boldsymbol{D}_e|}{T_{max}} = \tilde{k} \, \frac{1}{\tilde{L}_{tn}} \int_0^{\tilde{L}_{tn}} i(\xi) d\xi \tag{53}$$

where the parameter $\tilde{k}$ is

$$\tilde{k} = \varepsilon_0 \frac{|\boldsymbol{z}|}{3} \cdot \frac{\sin^2 2\phi_m - 2\Lambda_t/3}{\sin^2 2\phi_m \, (1 - \Lambda_t/2)}$$

Thus, we obtain the following expression

$$\frac{|\boldsymbol{D}_e|}{T_{max}} \approx \tilde{k} \, \sqrt{\frac{m_e}{m_i}} (\tilde{L}_{tn})^{\frac{3}{2}} \frac{3}{10} (1 + \frac{5}{7} \gamma_1 E_m L_t) \tag{54}$$

which shows how this ratio growths with $(\tilde{L}_{tn})^{\frac{3}{2}}$.

For the tape we are considering here, the maximum value of $\tilde{k}$ is $\tilde{k}_{max} \approx 0.37$. Taking into account the maximum value of $\tilde{L}_{tn}$ (about 10 during the eclipse operation), the ratio $|\boldsymbol{D}_e|/T_{max}$ reaches a maximum value about

$$\max \left(\frac{|\boldsymbol{D}_e|}{T_{max}} \right) \approx 0.027$$

Roughly, the angle α_0 measuring the deflection of the wire due to the electrodynamic drag is given, in the worse case, by:

$$\tan \alpha_0 \approx 0.027 \quad \Rightarrow \quad \alpha_0 \approx 1.6^\circ$$

Thus, the tether keeps its straight form with high accuracy.

1B.8 Conclusions

Passive deployment of our metallic tape, with no use of a flexible leader segment, would be possible if friction inside the deployer does not make the tension exceed about 0.15 N. The effects of residual stresses are negligible, except at the very beginning of the deployment (deployed length smaller than about 5 m).

During the eclipse phase, the electrodynamic torque in the system center of mass can be made negligible, if the mass distribution is carefully chosen. The tether keeps its straight form with high accuracy. The electrodynamic torque in the non eclipse phase cannot be made zero but takes small values, suggesting that the skip rope instability will take a long time to develop ($\sim$ 10 years in LEO). For electrodynamic tethers operating at inclined orbits, however, the greater sensitivity of the out-of-plane angle to lateral forces makes convenient a realistic dynamic simulation of the entire system.

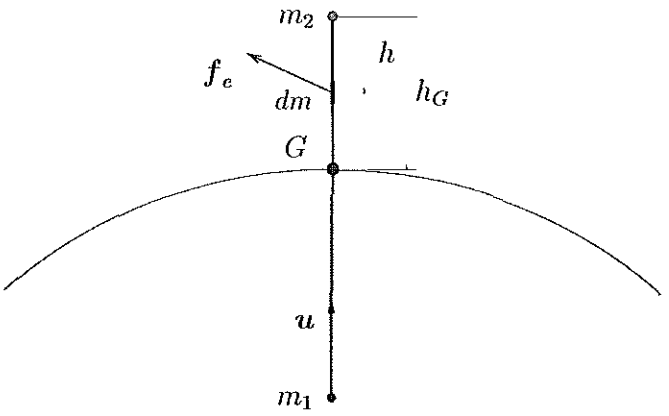

Figure 5: Mass distribution of the system

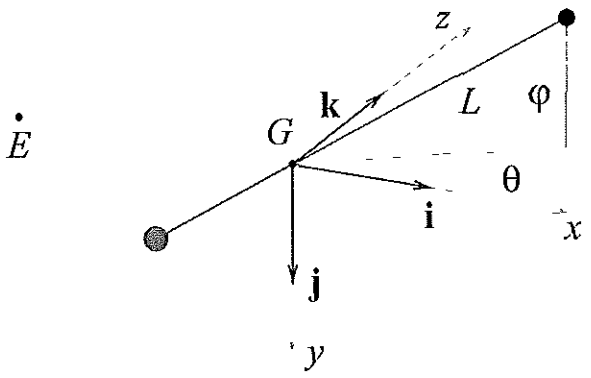

$E \rightarrow$ Earth center of mass $\quad Gz \rightarrow$ Direction of the velocity

$Gx \rightarrow$ Local vertical (to zenith) $\quad Gy \rightarrow$ Normal to the orbit

Figure 6: Libration angles

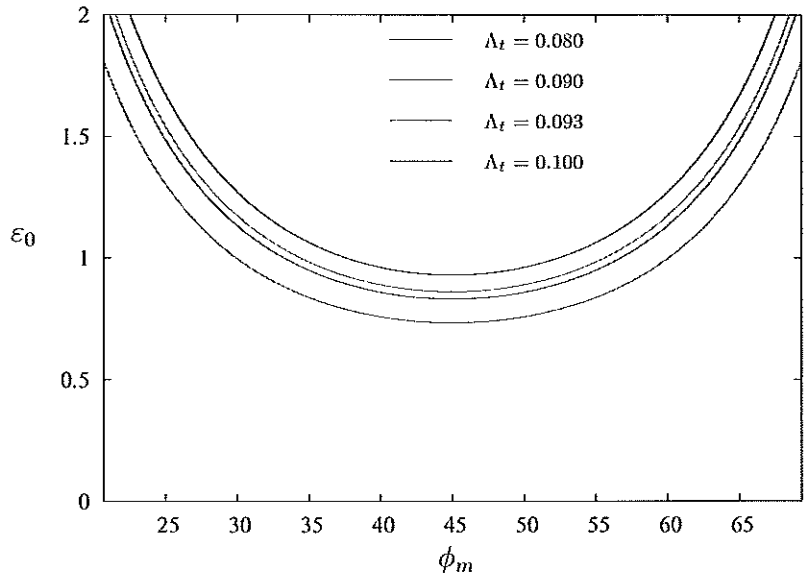

Figure 7: Parameter ε_0

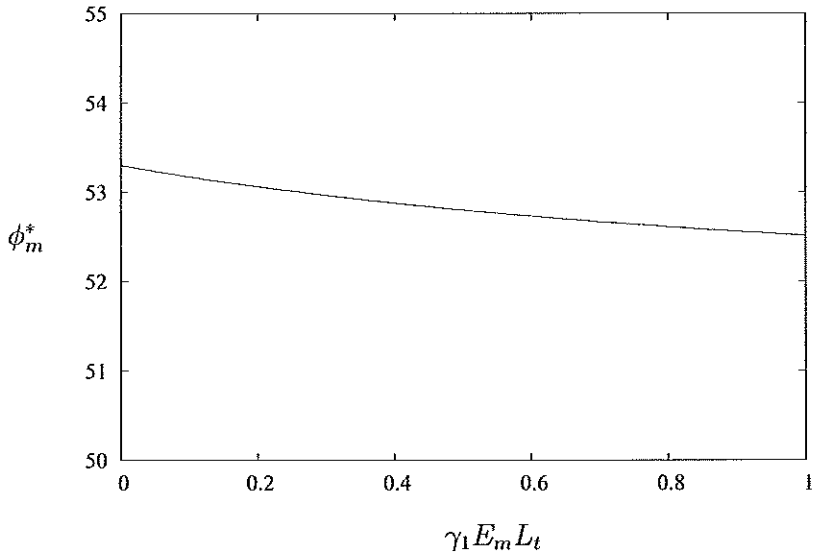

Figure 8: Critical value of ϕ_m

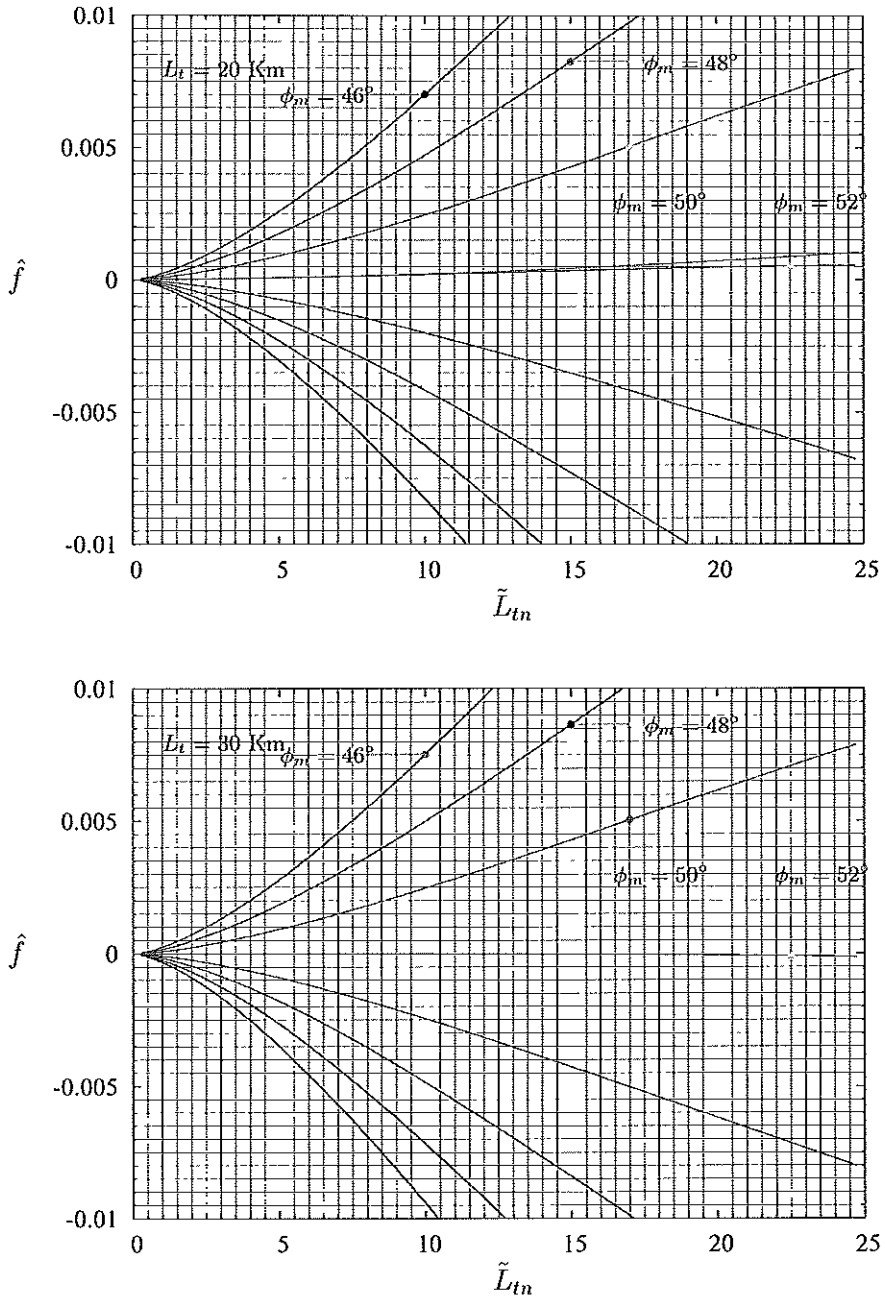

Figure 9: Factor $\hat{f}$ versus $\tilde{L}_{tn}$ for different values of $\phi_m = 46°, \ldots 60°$. In the upper figure $\gamma_1 E_m L_t = 0.5$. In the lower $\gamma_1 E_m L_t = 0.75$. In both cases $\sqrt{m_e/m_i} = 1/170$

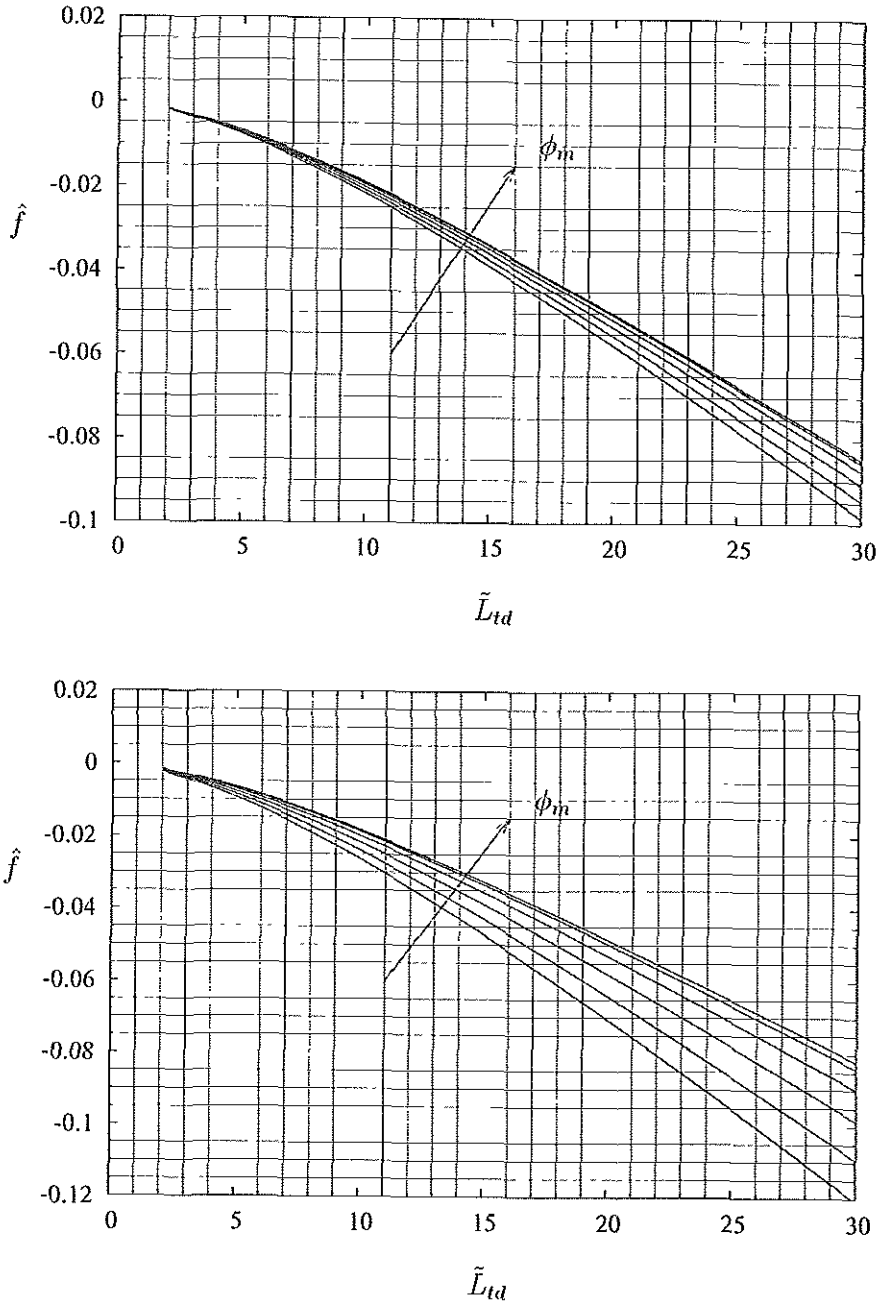

Figure 10: Factor $\hat{f}$ versus $\tilde{L}_{td}$ for different values of ϕ_m (from 40° to 90° by 10° incrment). In the upper picture $N_{\infty n}/N_{\infty d} = 0.1$. In the lower one $N_{\infty n}/N_{\infty d} = 0.3$. In both, $\gamma_1 E_m L_t = 0.5$, $r = 0.6$ and $\sqrt{m_e/m_i} = 1/170$

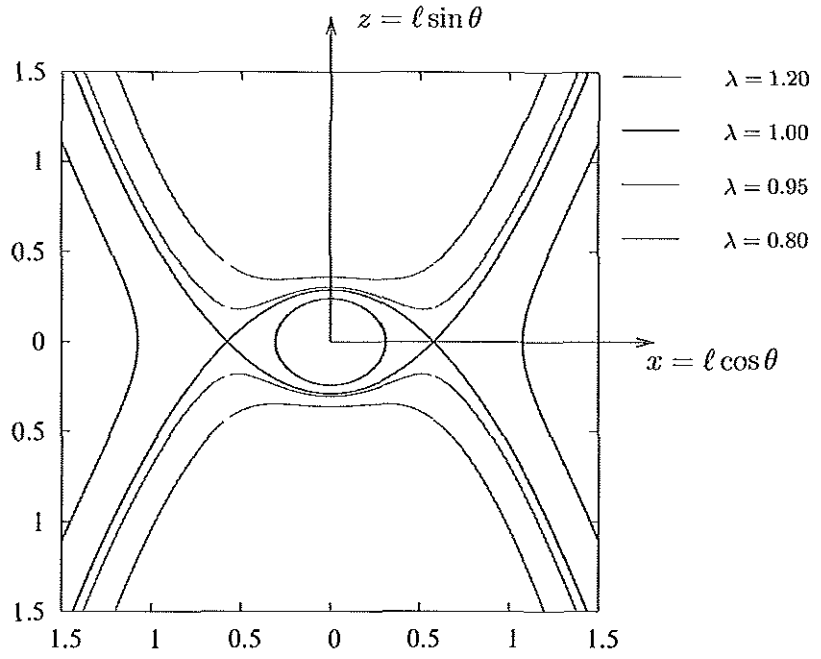

Figure 11: Boundary of the stopped deployment, in non dimensional lengths. Four different values of λ have been considered

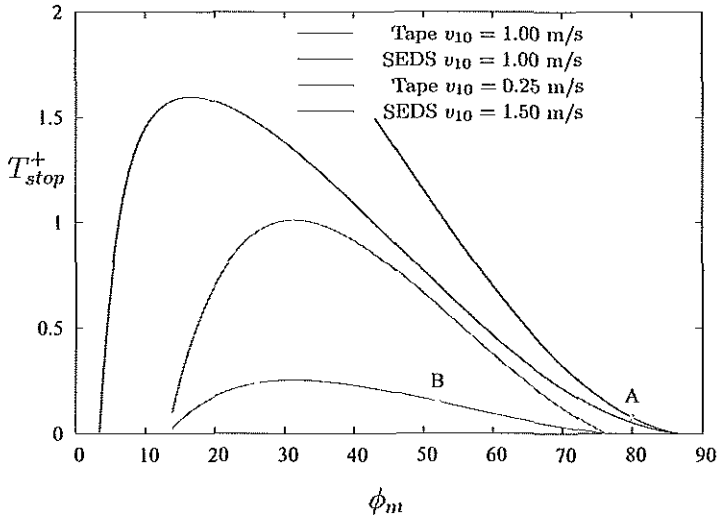

Figure 12: Function $T^+_{stop} = T^+_{stop}(\phi_m)$ for the SEDS and the free floating tethers.

2 *Auroral emissions and observations* (WP-200)

* *E-beam propagation and interaction* (WP-210)

2.1 Introduction

Secondary electrons are emitted with low energies (a few eV) and accelerate away from the tether under the large potential difference $\Phi_t - \Phi_p$ (a few kV). With tether bias large and 1/8 the tape-perimeter (3 mm) well below the Debye length at night, the potential would follow a 2-D Laplace solution for some distance, most of the outward acceleration of secondary electrons occurring away from the tape, where the potential is already near radial. As a first approximation we assume that at the start of their race along magnetic lines, secondary electrons are uniformly distributed in the azimuthal angle φ around the tether. From the relation $cos\theta = cosI \times cos\varphi$ one finds the normalized distribution in pitch angle θ (Fig.1), taking into account that both φ and $-\varphi$ contribute to the same value of θ,

$$f_\infty(\theta) = \frac{2}{\pi} \frac{sin\theta}{\sqrt{\cos^2 I - \cos^2 \theta}}. \qquad (1)$$

For the dipole model of the geomagnetic field considered in Sec.1A.4, the (dip) angle I between a magnetic line in the meridian magnetic plane and the horizontal plane varies along each orbit between zero and a maximum at the point nearest the magnetic pole, $I_{max} = \tan^{-1}(2 \tan i_m)$, i_m = magnetic inclination. At each value of I, the pitch angle θ ranges from I to $\pi - I$, but only electrons down the field line are considered ($I < \theta < \pi/2$). The half-width of the e-beam perpendicular to the tether is taken to be the electron gyroradius $l_{e\infty}$ at the emission energy $eE_m h \equiv \varepsilon_\infty(h)$, at each distance h from tether top,

$$l_{e\infty}(h) = \sqrt{\frac{2\varepsilon_\infty(h)}{m_e}} \times \frac{m_e}{eB}, \qquad \Omega_e \equiv \frac{eB}{m_e} = \Omega_{eq}(a)\sqrt{\frac{4+4tan^2 I}{4+tan^2 I}},$$

where $\Omega_{eq}(a)$ is the gyrofrequency at the magnetic equator, at the radius a of a circular orbit. This yields a (one-sided) electron flux,

$$\Phi_\infty(h) = \frac{1}{2}\frac{dI_{emit}/dh}{2l_{e\infty}\, e\cos I} = \sqrt{\frac{m_e}{m_i}}\frac{N_{\infty n}\, p\Omega_{eq} \times \gamma_1 E_m\, h}{2\pi\cos I\,\sqrt{1+3\cos^2 I}}, \qquad (2)$$

where we used Eq.(5) of section 1A.2.

Note that the beam flux increases (linearly) from top ($h = 0$) to bottom ($h = L_t$) although the half-width of the beam, $l_e \propto \sqrt{\varepsilon_\infty}$, increases itself as $\sqrt{h}$. This is because dI_{emit}/dh in Eq.(5) of Sec.1A.2 varies as $h^{3/2}$. Note also that the flux in (2) is much smaller than the random flux in the ambient plasma,

$$\Phi_{th} = N_\infty \times \sqrt{kT_e/2\pi m_e}\,.$$

With $\gamma_1 E_m L_t \sim 0.5$, $I \sim 45°$, and tape width less than the thermal gyroradius (~ 30 mm), the ratio Φ_∞/Φ_{th} is a small fraction of $\sqrt{m_e/m_i}$. Beam-plasma interactions will then have a negligible effect on the propagation of the beam.

As beam electrons move in helical paths down magnetic lines, they are slowed down by inelastic interactions with air molecules. For every ionization event there is a number of excitation collisions followed by prompt photon emission in the case of allowed transitions; one ionization is produced on the average for every 35 eV of energy (ε_i) lost by a beam electron. Cross sections have a similar energy dependence for all interactions and are characterized by a maximum, and an energy threshold, and can be written as

$$\sigma(\varepsilon) \approx \sigma_* \times g(\varepsilon/\varepsilon_*). \qquad (3a)$$

The cross-section shape function $g(u)$ must satisfy some conditions: *i*) g vanishes at high energy as $ln\varepsilon/\varepsilon$ (Born approximation); *ii*) g vanishes at a threshold energy ε_*; *iii*) g presents a maximum at $\varepsilon/\varepsilon_*$ between 4 and 5. There has been extensive modelling of g functions (*Green and Stolarski,* J. Atm. Terr. Phys, *1972*). The ionization cross-section σ_i is quite similar for both dominant species N_2 and O_2, with values σ_* ($\approx 9.7 \times 10^{-16}$ cm^2), ε_* (≈ 23.6 eV), $\sigma_{max} \approx 0.26\,\sigma_*$. For energy above ε_i, the cross-section is well modelled by the shape function

$$g(u) = \frac{u-1}{u^2} \ln u \qquad (3b)$$

(maximum $g \approx 0.26$ at $u \approx 4.24$).

As a secondary electron with energy ε, pitch angle θ and mean free path $1/n\sigma_i$ advances a distance dl in its path, the altitude loss is $dz = -\,sinI\cos\theta\, dl$ and the energy loss rate is (Fig.1)

$$sinI\cos\theta \frac{d\varepsilon}{dz} = \varepsilon_i\, n(z)\sigma_i(\varepsilon)\,. \qquad (4)$$

For the purpose of illustrating the analysis, the scale height for atmospheric (neutral particle) density n in the altitude range 120 - 200 km may be approximated as $n/|dn/dz| \approx z/3$, or $n = constant / z^3$, the constant being dimensionless (note that z is measured in meters if n is measured in m^{-3}) and z starting at 95 km above Earth (*Carroll,* Tethers in Space Handbook, 1997). For the mean CIRA reference atmosphere one has an approximate law

$$n(z) = 10^{31}/z^3, \qquad (5)$$

which we will use up to the tether altitude in the following discussion (Fig.2), where as noticed 10^{31} is a dimensionless constant. As we shall see results are not sensitive to the precise values of density above 200 km.

2.2 Pitch-averaged, frozen beam-flux model

For a first simple discussion we fully ignore beam broadening from scattering in elastic collisions, with the pitch distribution for the propagating beam also frozen in the initial form given by Eq.(1). We now simplify Eq.(4) by averaging $cos\theta$ over that distribution,

$$<cos\theta> = cos\, I \times 2/\pi. \tag{6}$$

Then Eq.(4) can be solved for the energy $\varepsilon\,(z; h)$ at height z of electrons leaving the tether at some given h, with the initial condition

$$\varepsilon\,[z_\infty(h)\,; h] \;=\; \varepsilon_\infty(h) \equiv eE_m h, \qquad z_\infty(h) \equiv z_M - h, \tag{7a, b}$$

where z_M is z at the top of the tether (Fig.2).

In Eq.(4) $d\varepsilon / dz$ should now be read as $\partial\varepsilon / \partial z$. One then finds

$$\int_{\tilde{\varepsilon}}^{\tilde{\varepsilon}_\infty(h)} \frac{du}{g(u)} = \frac{z_*^{\,2}}{sin\,2I}\left(\frac{1}{z^2} - \frac{1}{z_\infty^{\,2}(h)}\right), \tag{8}$$

$$\tilde{\varepsilon} \equiv \frac{\varepsilon}{\varepsilon_*}, \qquad z_* \equiv \sqrt{\frac{\pi}{2}\frac{\varepsilon_i}{\varepsilon_*}10^{31}\sigma_*} \;\approx\; 1514\,km. \tag{9a, b}$$

The solution (8) for $\tilde{\varepsilon}\,(z; h)$ is shown in Fig.3, for $h = L_t$, $L_t/2$ (tether bottom and midpoint). We took $L_t = 20$ km, $I = 45°$, $E_m = 165$ V/km, $z_M + 95$ km $= 305$ km. Curves are terminated at $\tilde{\varepsilon} = 1.5 \approx \varepsilon_i / \varepsilon_*$. We note that there is little energy decrease above 200 km. An approximate solution for possible use in chapter 4 on tomographic inversion,

$$\frac{\ln\tilde{\varepsilon}_\infty(h)}{2\ln\tilde{\varepsilon}_\infty(h) - 1}\left(\frac{\tilde{\varepsilon}_\infty^{\,2}(h)}{\ln\tilde{\varepsilon}_\infty(h)} - \frac{\tilde{\varepsilon}^2}{\ln\tilde{\varepsilon}}\right) \approx \frac{z_*^{\,2}}{sin\,2I}\left(\frac{1}{z^2} - \frac{1}{z_\infty^{\,2}(h)}\right), \tag{10}$$

is also shown for comparison. The approximation is very good down to energy ~ 500 eV, and is still good below (though errors in energy at given z are larger than suggested by the very flat profiles).

With pitch evolution and beam broadening from scattering ignored, the volumetric ionization rate is just

$$\dot{n}_i = \Phi_\infty(h)\, n(z)\, \sigma_i\left[\varepsilon(z;h)\right]. \tag{11}$$

Figure 4 shows ionization rate profiles for the cases in Fig.3. We further took $p = 24$ mm, $N_{\infty n} = 3 \times 10^5$ cm^{-3}, $\Omega_{eq} = 5.3 \times 10^6$ /s, $\gamma_1 = 0.15$/kV in Eq.(2).

Location and value of peak ionization for each given h can be analytically determined. From Eqs.(4) and (5) the maximum of $n(z) \times g[\tilde{\varepsilon}(z;\, h)]$ can be readily shown to satisfy the condition

$$\frac{dg(\tilde{\varepsilon})}{d\tilde{\varepsilon}} = \frac{3}{2}\frac{z^2}{z_*^2}\sin 2I, \tag{12}$$

with $\tilde{\varepsilon}$ and z also related by Eq.(8). With the right-hand-side of (12) positive and clearly very small, $\tilde{\varepsilon}$ will be very close to the value 4.24 for maximum g. Equation (8) then gives the altitude $z_{max}(h)$ for peak ionization as

$$\int_{4.24}^{\tilde{\varepsilon}_\infty(h)} \frac{du}{g(u)} \approx \frac{z_*^2}{\sin 2I}\left(\frac{1}{z_{max}^2} - \frac{1}{z_\infty^2(h)}\right). \tag{13}$$

Figure 5 shows the maximum of the ionization rate versus h or $\varepsilon_\infty(h)$, as given by (13). The peaks in Fig.4 are in very good agreement with Fig.5.

2.3 **Frozen beam-flux model**

Keeping the frozen pitch-distribution we solve Eq.(4) for each particular θ,

$$\int_{\tilde{\varepsilon}}^{\tilde{\varepsilon}_\infty(h)} \frac{du}{g(u)} = \frac{2}{\pi\,\tilde{\mu}}\frac{z_*^2}{\sin 2I} \times \left(\frac{1}{z^2 - z_\infty^2(h)}\right), \tag{8'}$$

where we wrote

$$\mu \equiv \cos\theta, \qquad \tilde{\mu} \equiv \mu / \mu_I.$$

Equation (8') determines either $\tilde{\varepsilon}(z;h,\tilde{\mu})$ or $\tilde{\mu}(z;h,\tilde{\varepsilon})$. The pitch distribution (1) takes here the form

$$f_\infty(\tilde{\mu}) = \frac{2/\pi}{\sqrt{1-\tilde{\mu}^2}}, \qquad 0<\tilde{\mu}<1. \tag{1'}$$

The volumetric ionization rate is now

$$\dot{n}_i(z;h) = \Phi_\infty(h)n(z)\times \int_{\tilde{\mu}_{min}(z;h)}^{1} \frac{2}{\pi}\frac{\sigma * d\tilde{\mu}}{\sqrt{1-\tilde{\mu}^2}}\, g[\tilde{\varepsilon}(z;h,\tilde{\mu})]. \tag{11'}$$

The lower end of the integration range is determined by setting $\tilde{\varepsilon} = \tilde{\varepsilon}_i = 1.5$ in Eq.(8'), that is, $\tilde{\varepsilon}[z;h,\tilde{\mu}_{min}] = 1.5$. Note that electrons with low pitch angle in Eq.(4) penetrate further down; electrons with pitch angle $\theta > \cos^{-1}(\tilde{\mu}_{min}\times\cos I)$ had reached down to energy ε_i at some altitude above z. Figure 6 shows ionization-rate profiles for $h = L_t$, $L_t/2$. One basic result is that retaining the spectrum of pitch angles makes profile maxima broader than those in Fig.4 corresponding to a single, average pitch angle (a similar broadening would occur if electrons exhibited a spectrum of energies, instead of being monoenergetic -for each h value-, as in our tether beam). Also shown for comparison are profiles resulting from using the left-hand-side of (10) as an approximation for the LHS of (8').

2.4 **Scattering effects: Isotropic-pitch model**

For a rough estimate of scattering effects we now consider a new limit model: we assume that the electrons reach an uniform pitch-angle distribution over the range 0 - $\pi/2$ immediately after leaving the tether, and keep this distribution afterwards. The solution to Eq.(4) takes now the form

$$\int_{\tilde{\varepsilon}}^{\tilde{\varepsilon}_\infty(h)} \frac{du}{g(u)} = \frac{{z_*}^2}{\pi\,\mu\,\sin I}\left(\frac{1}{z^2} - \frac{1}{{z_\infty}^2(h)}\right), \qquad (8")$$

with a pitch distribution

$$f_\infty(\mu) = \frac{2/\pi}{\sqrt{1-\mu^2}}, \qquad 0 < \mu \equiv \cos\theta < 1. \qquad (1")$$

The volumetric ionization rate is now

$$\dot{n}_i(z;h) = \Phi_\infty(h)\,n(z) \times \int_{\mu_{min}(z;h)}^{1} \frac{2}{\pi}\frac{\sigma_* d\mu}{\sqrt{1-\mu^2}}\; g\left[\tilde{\varepsilon}(z;h,\mu)\right], \qquad (11")$$

with $\tilde{\varepsilon}(z;h,\mu)$ determined by (8"). The lower end of the integration range is again determined by setting $\tilde{\varepsilon} = 1.5$ in Eq.(8"), that is, $\tilde{\varepsilon}\left[z;h,\mu_{min}\right] = 1.5$. Figure 7 shows ionization rate profiles for L_t, $L_t/2$. Also shown for comparison are profiles resulting from using the LHS of (10) as an approximation for the LHS of (8").

2.5 **Scattering effects: Beam broadening**

As electrons move down the magnetic field, elastic collisions, in addition to affecting the pitch distribution, will result in the broadening of beam-width due to diffusion perpendicular to the magnetic lines. For (onedimensional) diffusion along the horizontal direction perpendicular to the beam one has

$$v_{par}\frac{d<R^2>}{dl_{par}} = 2 \times D_\perp \qquad (14)$$

where v_{par} is the electron velocity parallel to the magnetic field and dl_{par} is the distance advanced parallel to the field corresponding to a height decrease dz (Fig.1),

$$v_{par} = \sqrt{2\varepsilon/m_e} \times \cos\theta\,, \qquad dl_{par} = -dz/\sin I\,;$$

$\sqrt{< R^2 >}$ is the diffusion length; and $D_\perp$ is the diffusion coefficient perpendicular to the magnetic lines,

$$D_\perp = \frac{1}{3}\sqrt{\frac{2\varepsilon}{m_e}}\,\lambda_c \times \frac{l_e^{\,2}}{\lambda_c^{\,2}}, \qquad l_e << \lambda_c,$$

the mean-free-path $\lambda_c = 1/n(z)\sigma_c$ being much greater than the electron gyroradius l_e at energy $\varepsilon < \varepsilon_\infty(L_t)$.

One then finds

$$sinI\cos\theta\,\frac{d\langle R^2\rangle}{dz} = -\frac{2}{3}\,l_e^{\,2}(\varepsilon)\sigma_c\,n(z). \tag{15}$$

Note that as electrons move down the field, the broadening rate decreases because their energy is progressively lower but increases because of the increasing density. With magnetic field nearly constant throughout the electron path, we have $l_e \propto \sqrt{\varepsilon}$. Using Eq.(4) and writing $l_e^{\,2} = l_{e\infty}^{\,2}(h) \times \varepsilon/\varepsilon_\infty(h)$ we then find

$$\frac{d < R^2 >}{d\tilde{\varepsilon}} = -\frac{2}{3}\,\frac{l_{e\infty}^{\,2}(h)\times\tilde{\varepsilon}}{\tilde{\varepsilon}_\infty(h)\tilde{\varepsilon}_i\; g(\tilde{\varepsilon})}, \tag{16}$$

where we took $\sigma_c \approx 10^{-15}$ cm^2 $\approx \sigma_*$. Using $\sqrt{<R^2>} = l_{e\infty}$ at $\varepsilon = \varepsilon_\infty$ one finds

$$\frac{< R^2 >}{l_{e\infty}^{\,2}(h)} = 1 + \frac{2/3}{\tilde{\varepsilon}_i\,\tilde{\varepsilon}_\infty(h)} \times \int_{\tilde{\varepsilon}}^{\tilde{\varepsilon}_\infty(h)} \frac{u\,du}{g(u)}. \tag{17}$$

The broadening factor

$$\frac{\sqrt{< R^2 >}}{l_{e\infty}(h)} \equiv f_{br}\left[\tilde{\varepsilon},\tilde{\varepsilon}_\infty(h)\right] \equiv \sqrt{1 + \frac{2/3}{\tilde{\varepsilon}_i\,\tilde{\varepsilon}_\infty(h)} \times \int_{\tilde{\varepsilon}}^{\tilde{\varepsilon}_\infty(h)} \frac{u\,du}{g(u)}} \tag{18}$$

is shown in Fig.8 for h = 20 km, 10 km.

As a result of beam broadening, the flux of electrons that left the tether at a given h is reduced (along with energy) as it propagates,

$$\Phi(h,\tilde{\varepsilon}) = \frac{\Phi_\infty(h)}{f_{br}\left[\tilde{\varepsilon},\tilde{\varepsilon}_\infty(h)\right]}. \qquad (19)$$

When this correction is introduced into the ionization rate for the isotropic-pitch model of Sec.2.4, as given by Eq.(11"), we find

$$\dot{n}_i(z;\,h) = \Phi_\infty(h)\times n(z)\times \int_{\mu_{min}(z;h)}^{1} \frac{2}{\pi}\frac{\sigma * d\mu}{\sqrt{1-\mu^2}}\frac{g\left[\tilde{\varepsilon}(z;\,h,\mu)\right]}{f_{br}\left[\tilde{\varepsilon}(z;\,h,\mu),\,\tilde{\varepsilon}_\infty(h)\right]}. \qquad (20)$$

Figure 9 compares ionization profiles from Eqs.(11), (11'), (11") and (20). We first note that electrons in the (no-broadening) isotropic pitch-angle model penetrate further and produce higher ionization than electrons in the frozen pitch-angle model, but they keep close to each other up to very near the maximum in this last model. Next we note that broadening results in a reduction of the ionization rate by more than one order of magnitude. Also, since the factor f_{br} soon approaches near constant values with decreasing energy in Fig.8, a simple approximation to Eq.(20) would be multiplying (8") by an average factor that varies from about 12 for $L_t/2$ to about 24 for L_t.

2.6 **Column-integrated ionization rate**

For later observational considerations it is convenient to introduce the 'column'-integrated ionization rate along any straight line, $\int \dot{n}_i ds$, with ds the length element along the line and the integral extending over the ionization region. For a line coinciding with the magnetic line through some point in the tether we have $ds = -\,dz\,/\,sinI$ with s starting at the tether (Fig.2). The range of integration vanishes for a line with $h < \varepsilon_i / eE_m$. For the pitch-averaged frozen model of Sec.2.2 and $h > \varepsilon_i / eE_m$ one can readily use Eqs.(4), (6) and (11) to find

$$\int \dot{n}_i \frac{-dz}{sinI} = \Phi_\infty(h)\times\frac{\mu_I}{2\pi}\times\frac{\varepsilon_\infty(h)-\varepsilon_i}{\varepsilon_i}.$$

For the isotropic-pitch model of Sec.2.4 we find

$$\int \dot{n}_i \frac{-dz}{sinI} = \Phi_\infty(h) \times \int_{z_{min}(h)}^{z_\infty(h)} \frac{dz}{sinI} n(z) \times \int_{\mu_{min}(z;h)}^{1} \frac{2}{\pi} \frac{\sigma * d\mu}{\sqrt{1-\mu^2}} g\left[\tilde{\varepsilon}(z;h,\mu)\right],$$

with $\tilde{\varepsilon}(z;h,\mu)$ as given in Eq.(8"), and

$$\tilde{\varepsilon}\left[z;h,\mu_{min}\right] = \tilde{\varepsilon}_i = 1.5,$$

$$\tilde{\varepsilon}\left[z_{min};h,1\right] = 1.5.$$

A similar result is found for the frozen-pitch model of Sec.2.3.

The lines of interest for observational considerations in chapter 3 correspond to lines of sight from the top of the tether at a (small) angle ψ with the magnetic field (Fig.2). Relations immediately following from that figure are

$$sin\,(I + \psi)\, ds = - dz, \tag{21}$$

$$\frac{tan(I+\psi)}{tan\,I} = \frac{z_M - z}{z_\infty(h) - z}. \tag{22a}$$

For ψ small against I one would have $ds \approx - dz / sin\,I$ and

$$\frac{2\psi}{sin\,2I} \approx \frac{z_M - z}{z_\infty(h) - z} - 1 \approx \frac{h}{z_M - z}. \tag{22b}$$

We would then find, for the isotropic-pitch model including beam broadening,

$$\int \dot{n}_i ds = \int_{z_{min}(\psi)}^{z_{max}(\psi)} \frac{dz}{sin\,I} \Phi_\infty(h)\; n(z) \times \int_{\mu_{min}[z;h]}^{1} \frac{2}{\pi} \frac{\sigma * d\mu}{\sqrt{1-\mu^2}} \frac{g\left[\tilde{\varepsilon}(z;h,\mu)\right]}{f_{br}\left[\tilde{\varepsilon}(z;h,\mu),\tilde{\varepsilon}_\infty(h)\right]} \tag{23}$$

with $h = h(z;\, \psi)$ given by Eq.(22a) or (22b).

We note that ionization does not occur above certain altitude z_{max} and below another altitude z_{min} where $\varepsilon = \varepsilon_i$ on the line-of-sight. These altitudes are determined by using (22b) for $h(z;\, \psi)$ in Eq.(8") and setting $\tilde{\varepsilon} = 1.5$ and $\mu = 1$ on its left and right hand sides, respectively, yielding

$$\int_{1.5}^{1.5 \times 2\psi\, eE_m (z_M - z)/\varepsilon_i\, sin\,2I} \frac{du}{g(u)} = \frac{z_*^2}{\pi\, sin\,I} \left(\frac{1}{z^2} - \frac{1}{z_M^2} \right).$$

There are 2 roots (z_{max} and z_{min}) to this equation, except at small enough ψ; both are shown in Fig.10. Similar results are found for the isotropic-pitch model without beam broadening and for the frozen-pitch model. Figure 11 shows the column-integrated ionization rate versus the angle ψ for all three pitch-distribution models. The factor 10^{-6} in the rates introduced in the graph will make estimates of emission luminosity in Ch. 3 easier.

2.7 Conclusions

In the tomographic analysis of chapter 4 we will use the isotropic-pitch model with broadening. We note that the density law enters the column-integrated ionization rate in (23) in quite a complex way: both explicitly and through the function $\tilde{\varepsilon}(z,h,\mu)$, itself appearing in two ways [in the functions g and f_{br} and in the integration limits $\mu_{min}(z, h)$ and $z_{min}(\psi)$ and $z_{max}(\psi)$]. In the tomographic analysis, the density law $n(z)$ will be left undetermined in the algorithm for the column-integrated ionization rate. The complex nonlinearity dependence of column integrated rates could make tomographic inversion to determine the neutral density vertical profile difficult. Also, note in Fig.11 that broadening at the top of the peak is much more effective than in the wings, resulting in a flattening of the peak. This effect might also make tomography harder. A completely flat profile for luminosity versus line-of-sight, which would be equivalent to an initial energy ε_∞ independent of h, would make tomography impossible, as immediately verified.

As regards effects of the ionospheric environment at the emitting heights, the geomagnetic field enters results in a complex way too, through the values of the dip angle I, the motional field E_m, and the electron gyrofrequency (at the magnetic equator at orbital radius a) $\Omega_{eq}(a)$, again both explicitly [see Eq.(2) for $\Phi_\infty(h)$] and

through the function $\tilde{\varepsilon}(z,h,\mu)$. Three-axis measurements of the magnetic field in orbit will be required. The dependence of column-integrated ionization rate on plasma density N_∞ (and on secondary-yield coefficient γ_1) is of simple proportionality, though N_∞ measurements in orbit, and careful precalibration of tether yield, will be also required.

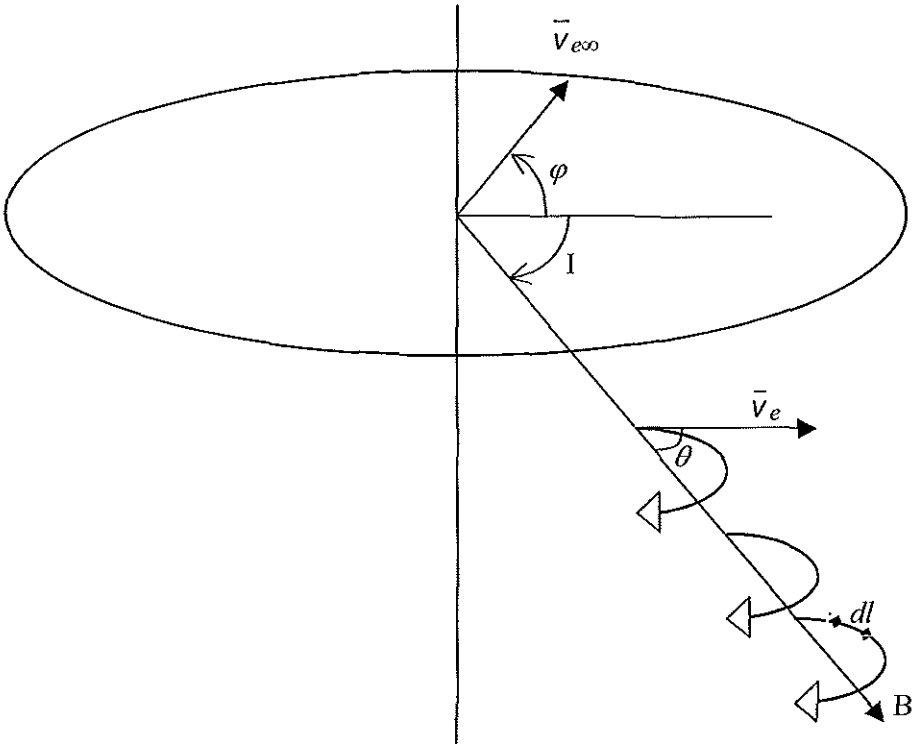

Figure 1: Geometry of tether electron emission and pitch determination.

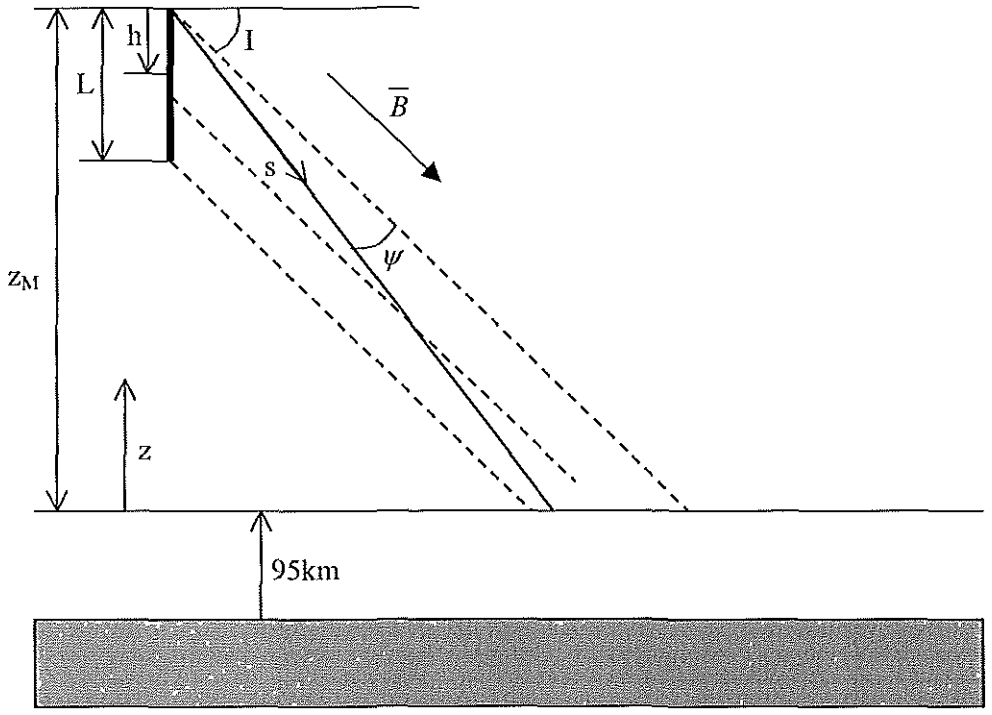

Figure 2: Geometrical disposition of tether and geomagnetic field.

Figure 3

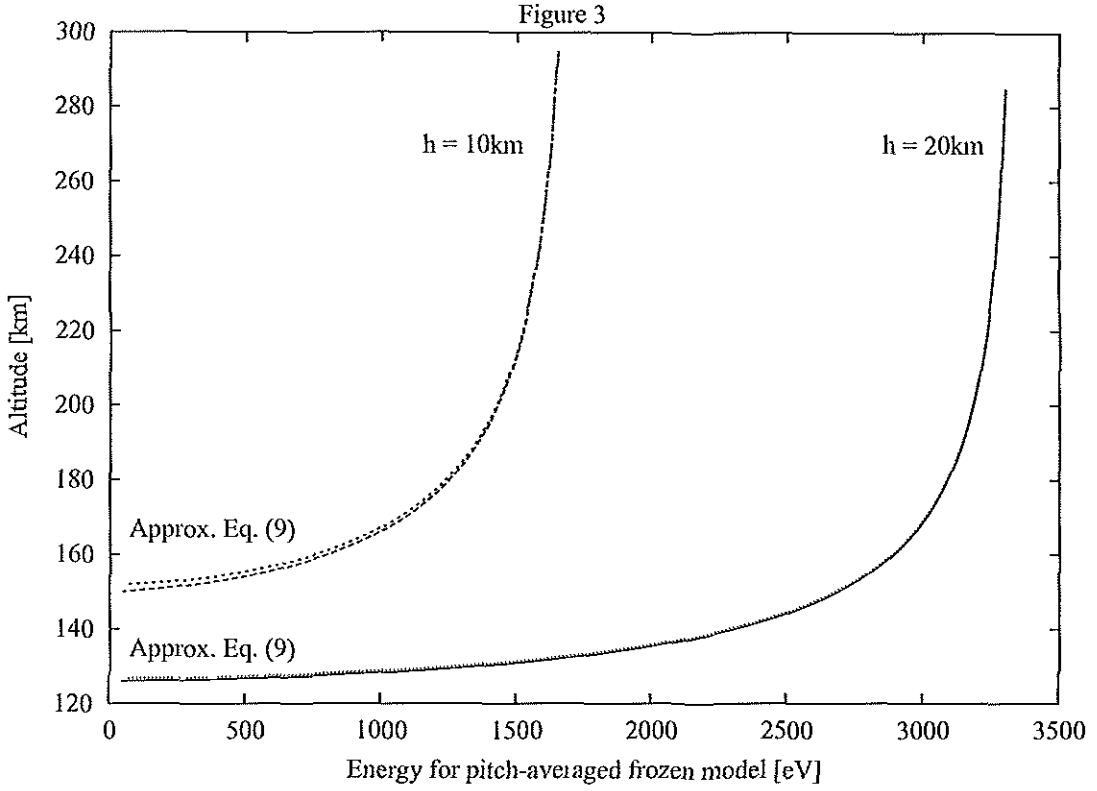

Figure 4

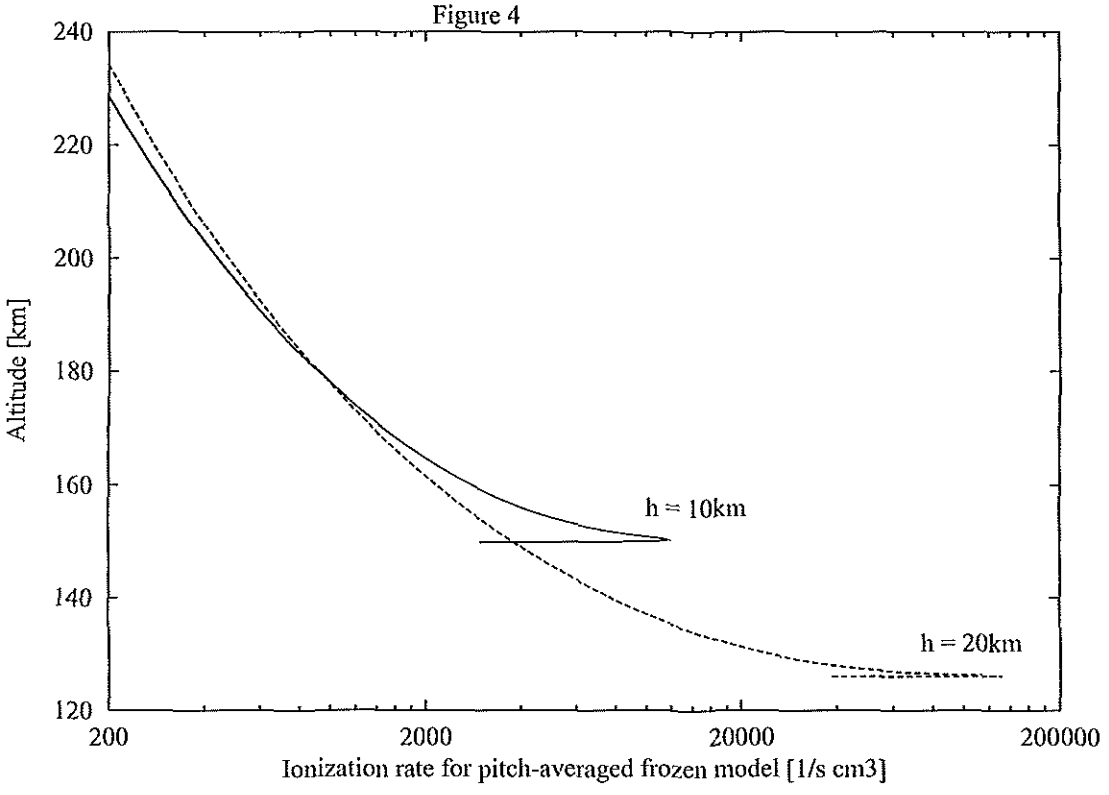

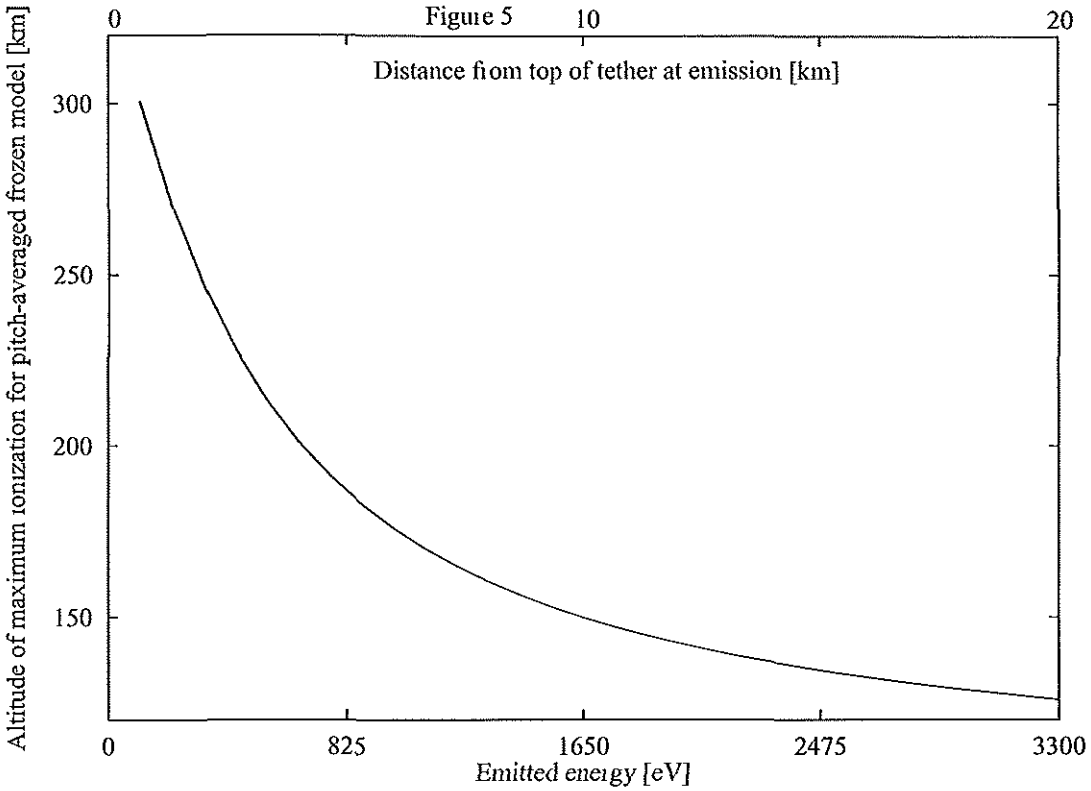

Figure 5

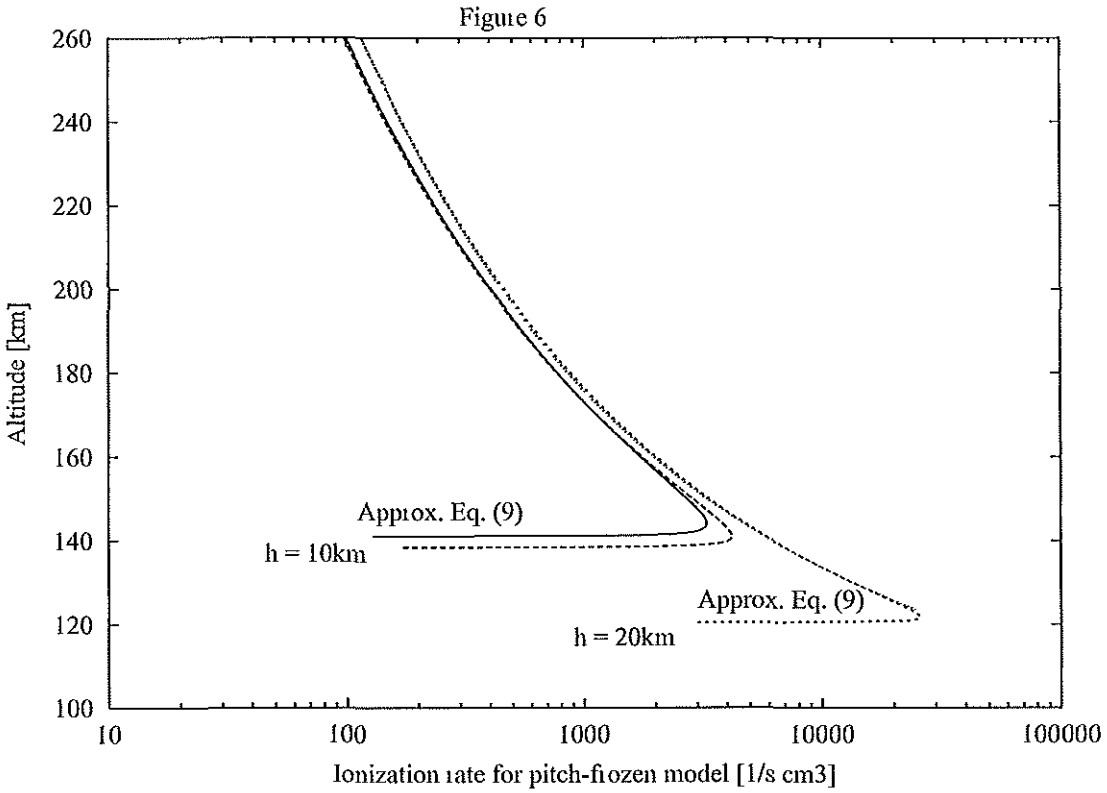

Figure 6

Figure 7

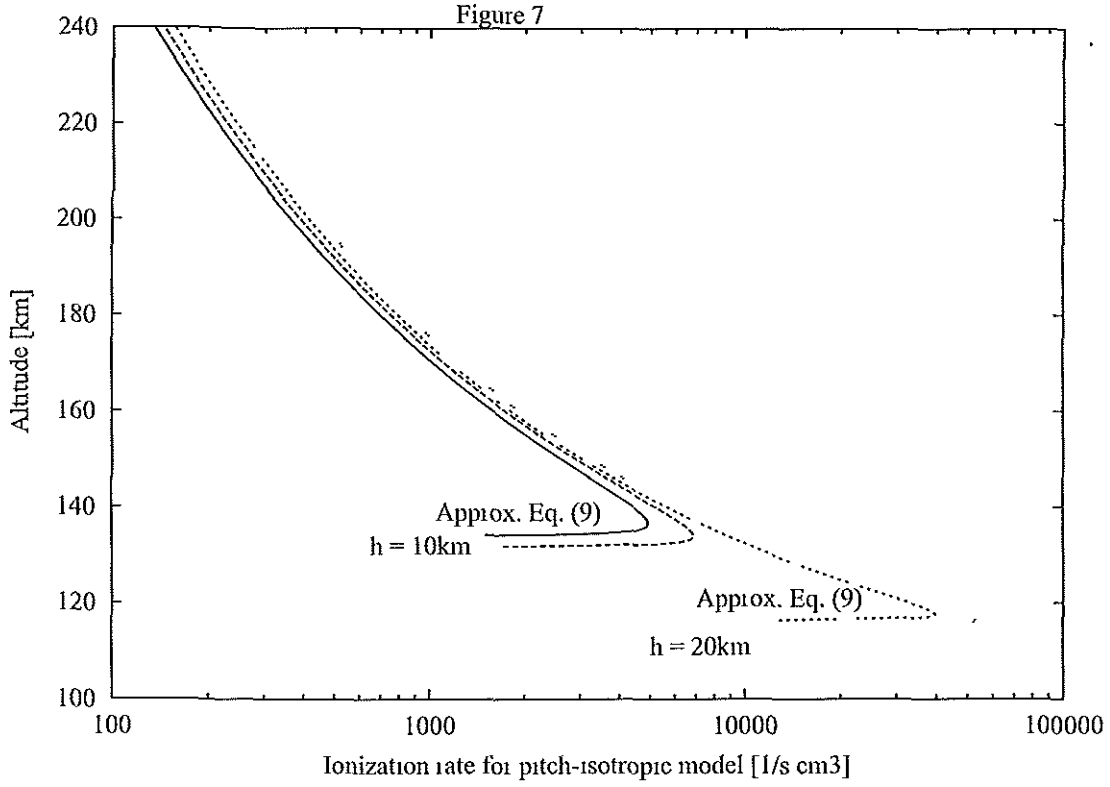

Figure 8

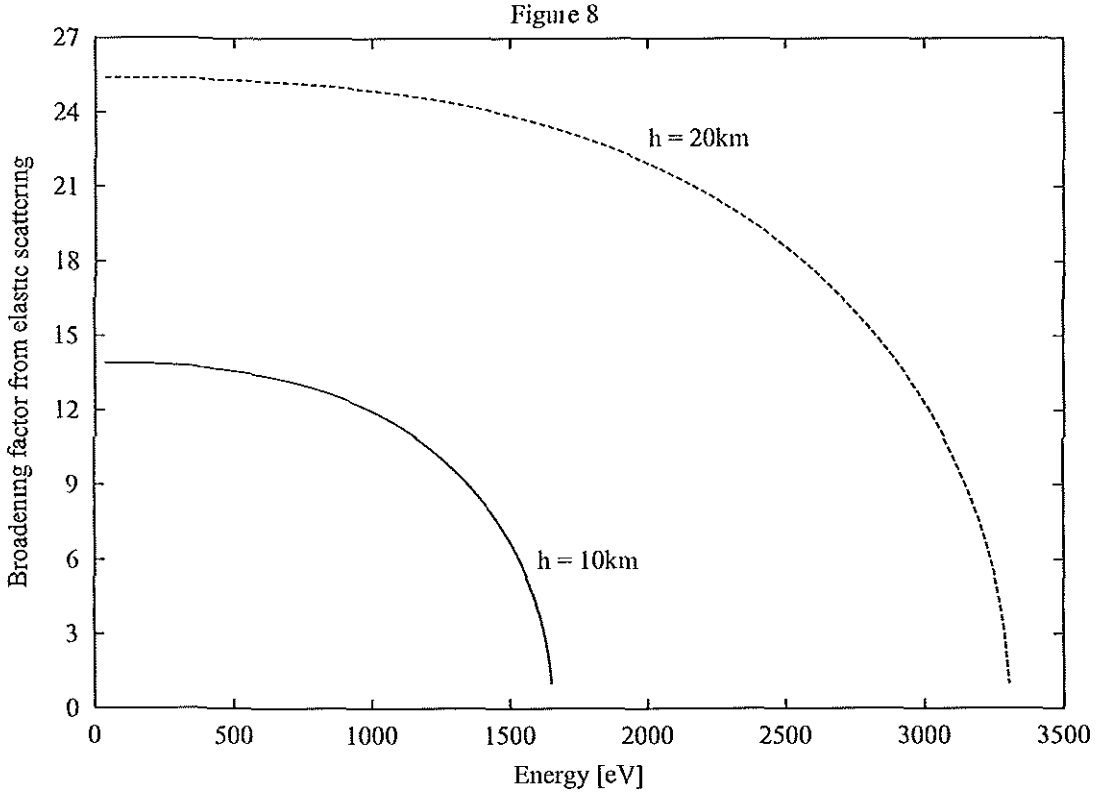

Figure 9

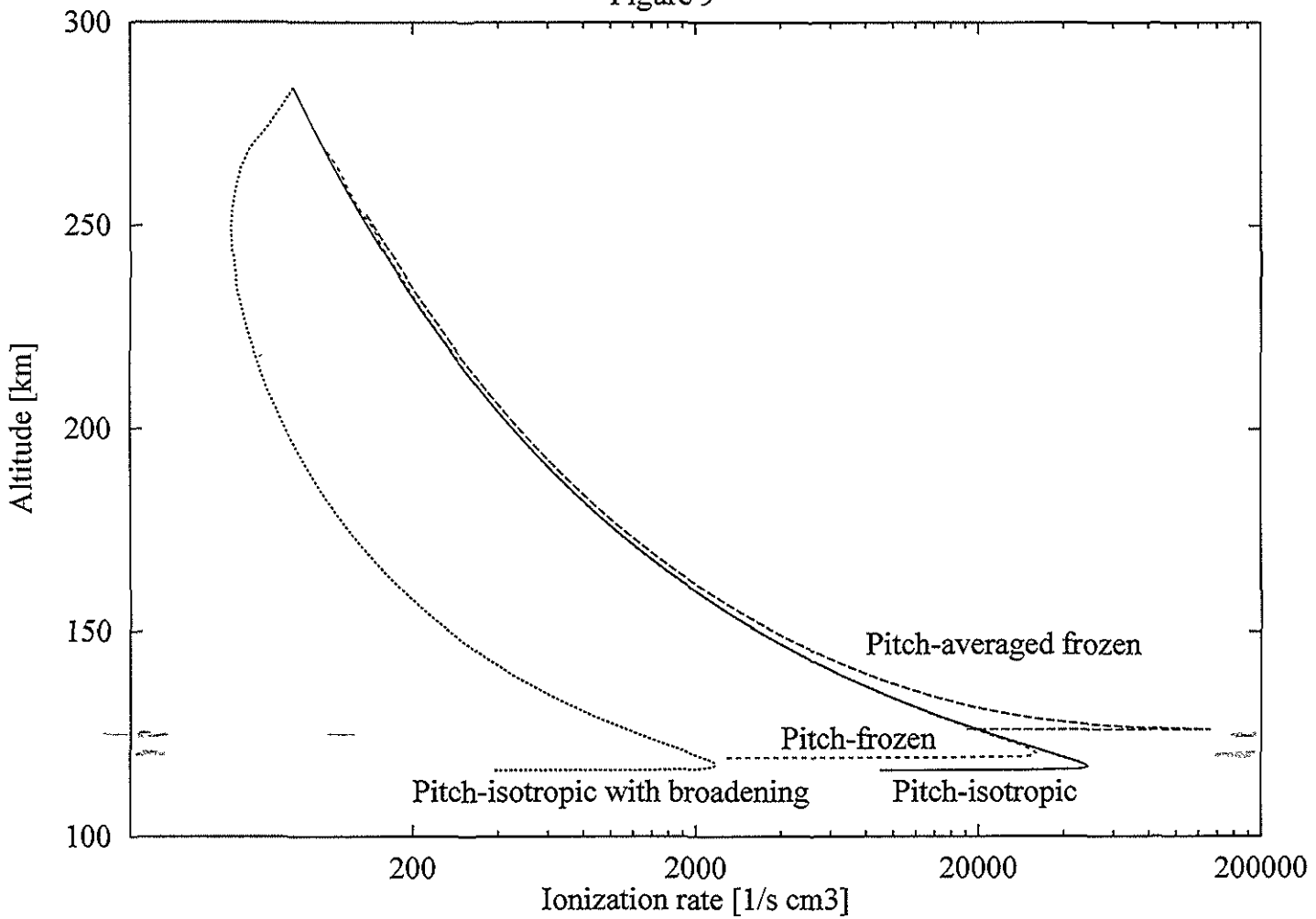
300
250
200
150
100
Altitude [km]
200
2000
20000
200000
Ionization rate [1/s cm3]
Pitch-averaged frozen
Pitch-frozen
Pitch-isotropic with broadening
Pitch-isotropic

Figure 10

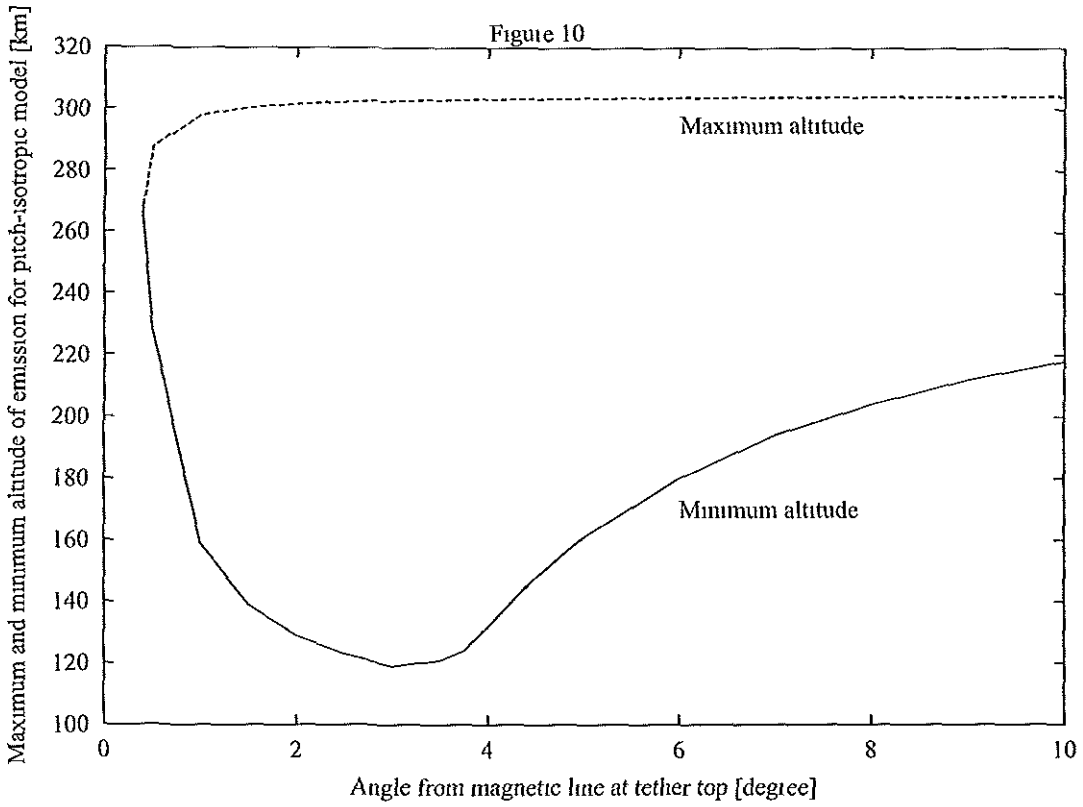

Figure 11

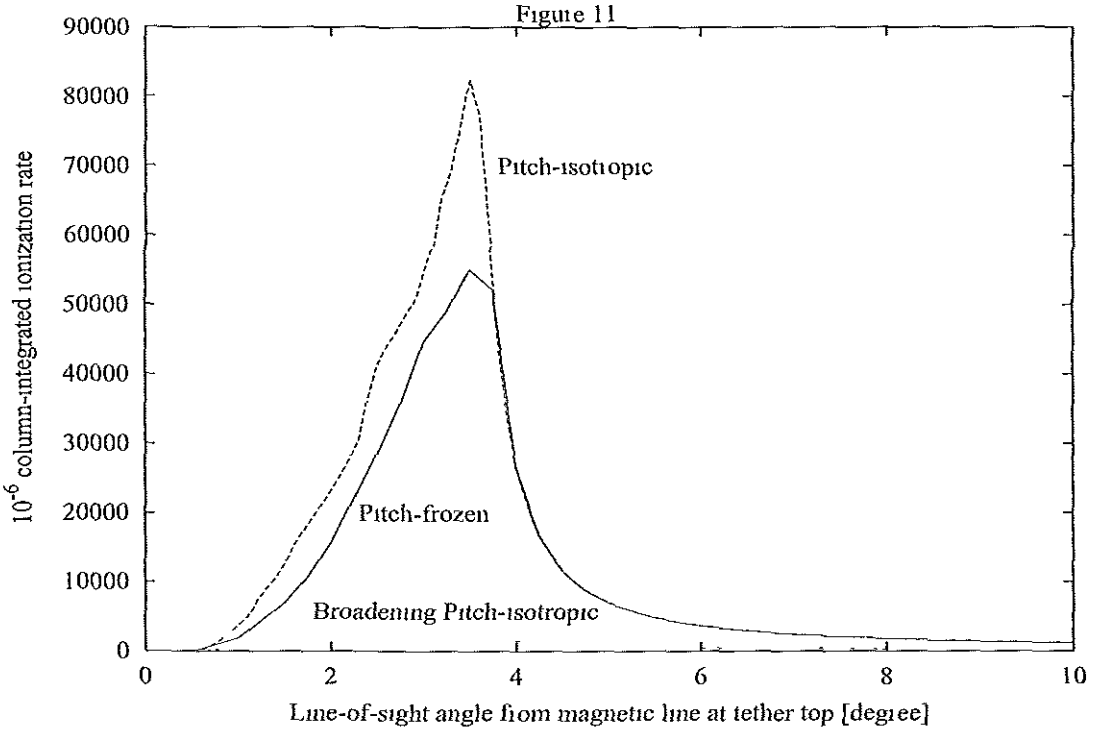

3 *Auroral emissions and observations* (WP-200)

* *Feasibility of observational options* (WP-220)

3.1 Introduction

The electron beam produced by a bare tether is characterized by a number of singular features: Each point in the tether ejects monoenergetic electrons. The energy of the ejected electrons increases linearly from top to bottom of the tether. These two features appear convenient for the main purpose of using a bare tether for auroral studies, which in principle would be to provide real-time mapping of the vertical structure of the neutral density in a critical thermospheric layer, 110 - 160 km say. The *e*-beam of the tether is also characterized, however, by two other less convenient features: Its auroral emissions are highly localized in both space and time.

Regarding time dependence, consider Fig.1 and use the dipole model of the geomagnetic field. The plane of the figure would be a magnetic meridian plane and the closest magnetic pole would lie on the right in the figure. The dip angle would be $I = tan^{-1}(2/tan\theta_m)$ where θ_m is the magnetic colatitude, horizontal and vertical components of the dipole-field being proportional to $sin\theta_m$ and $2\ cos\theta_m$ respectively. The dip would vanish at the magnetic equator (a region thus useless for the purpose of the present study) and reach a maximum $I_{max} = tan^{-1}(2\ tan\ i_m)$ at the point nearest the magnetic pole, where $\pi/2 - \theta_m = i_m$ (inclination of orbit to the magnetic equator). Ignoring the dipole-tilt for simplicity, magnetic and geographic equator, poles and orbital inclination would be the same, with $i_m = i_{orb} = const$ (Fig.2); in the northern hemisphere, the tether would move to the right in the plane of Fig.1 from ascending node to point nearest the pole, and to the left afterwards. Perpendicular to that plane the velocity will vary from $v_{orb}\ cos\ i_{orb}$ at the equator to v_{orb} at the point nearest the pole.

With the beam thick 250 m at most, v_{orb} about 7.5 km/s, and orbital inclination moderate, the dwell-time of the beam at some particular point will be no more than a few tens of msecs (this is about the time beam electrons at KeV energies take to travel down from the tether, too).

That dwell time is much too short for the population density of electrons resulting from beam-induced ionization (now called *secondary* electrons), n_{ss}^{sec}, to approach a steady state. This state would be basically determined by the balance between ionization and the dissociative recombination of O_2^+ and NO^+ (since N_2^+ converts rapidly via $N_2^+ + O \rightarrow NO^+ + N$). We would have $(n_{ss}^{sec})^2 \sim \dot{n}_i / c_{\sec}\sigma_{rec}$, where c_{sec} is the thermal velocity (at fraction-of-eV energy) of the *secondaries*. With $\dot{n}_i \sim 1 - 2 \times 10^3$ cm^{-3} s^{-1} as found in Ch.2, $n_{ss}^{\sec}$ might exceed 10^5 cm^{-3}, well above the night-time plasma density. The buildup time ($\sim n_{ss}^{\sec} / \dot{n}_i$), however, would be 10 - 100 seconds, or about 10^3 times the dwell time; the localized modifications in plasma density and associate plasma effects would thus be barely detectable.

On the other hand, the population of excited states with typical lifetimes (about 10^{-7} - 10^{-8} s) much shorter than the dwell-time, and their prompt emission through *allowed* transitions, will be able to reach a steady-state. Such transitions include the prominent N_2^+ first negative spectral bands at 427.8 nm and 391.4 nm, and the 777.4 and 844.6 nm lines and bands from atomic and molecular oxygen. The case for *forbidden* transitions from states with lifetimes of order of second and longer is different; relevant examples are the green line (557.7 nm) and the red doublet (630.0 and 636.4 nm) of atomic oxygen. Our tether for auroral studies must discard any such emissions. The ratio of auroral intensity at 630.0 nm to the intensity at 391.4 nm has been used in the past to determine the characteristic energy of the incident beam electrons. In our case, however, that energy is known a priori.

3.2 **Observations from the spacecraft**

For allowed transitions at steady state, emission rates are determined by, and proportional to the excitation rates. With cross sections for ionization and excitations quite similar in shape, and just differing in cross-section maximum and in energy at maximum (and at threshold), simple, approximate relations between emission and ionization rates have been established for prominent spectral bands and lines under some standard conditions. In particular, about 70 - 75 ion-electron pairs are produced for every N_2^+-band, $\lambda = 427.8$ nm photon emitted, and 25 pairs in the case of the $\lambda = 391.4$ nm band (*Carlson and Egeland*, Introduction to Space Physics, 1995), with emission at the 557.7 nm line still higher. Writing $\dot{n}_{em}(j) \approx c_j \times \dot{n}_i$ with a different constant c_j for each line or band j, one may use results from chapter **2** on ionization rate $\dot{n}_i(z;h)$ and column-integrated rate $\int \dot{n}_i\, dz$ to determine 'surface brightness'. Surface brightness, as measured in Rayleigh units, is proportional to the column-integrated rate of (optically thin) emission,

$$b_j(R) \equiv 10^{-6} \times \int \dot{n}_{em}(j)\, ds = 10^{-6}\, c_j \times \int \dot{n}_i\, ds\,, \qquad (1)$$

with rate and depth of (optically thin) emission in cgs units. Brightness of 1 Rayleigh corresponds to $4\pi \times 10^{-6}$ photons per cm^2, per second, per stereoradian, reaching the detection system.

Ground observation accross the propagating beam would yield brightness for each point in the beam, which could provide, in principle, direct vertical resolution of the density structure. Observation from a second satellite, lagging or leading the tether in the same orbit, would be a more demanding alternative but could provide continuous measurements. Signal accross the beam, however, appears too weak because the beam is thin, beam broadening being negatively balanced by the inverse reduction in beam

flux and ionization rate. Taking a typical value $c \sim 1/50$ and ignoring broadening we have an optical depth $\Delta s \approx 10$ m = 1000cm, and $\dot{n}_i(max) \approx 50{,}000$ /cm^3 s (see Fig.9 of chapter **2**), Eq.(1) then yielding $b \approx 1\ R$. Taking broadening into account increases Δs by a factor 20 - 25 but decreases $\dot{n}_i(max)$ in that Fig.9 by a similar factor.

There are sources of light in the night sky from other particle precipitation into the atmosphere, even at low and middle latitudes, making for background noise that could mask any $b \approx 1\ R$ effect; there is a continual drizzle from the radiation belts, with precipitating electrons at 1- 10 keV characteristic energy coming from the plasma sheet. The best chance would correspond to magnetically quite conditions around 40° latitude (*Kelley*, The Earth's Ionosphere, 1989). One way out for observation across the beam might be increasing the signal-to-noise ratio by periodically pulsing the Hollow Cathode. This would result in the intensity of auroral emissions showing a high frequency component superposed on slow variations due to any modulation in background light sources and atmospheric processes, and will be later discussed.

An auroral layer thin but otherwise extensive would clearly appear most intensive from the ground when viewed at a high elevation angle. Note now that observation from the spacecraft would provide line-of-sights along beam length (and width) equivalent to maximum "elevation angle". One may then directly use results from chapter **2** to determine 'surface brightness' at each angle ψ from the magnetic field,

$$b(R) \equiv 10^{-6} c \times \int \dot{n}_i \frac{dz}{sin(I + \psi)}. \qquad (2)$$

When beam broadening is taken into account in column-integrated ionization rates (Fig.11 of chapter **2**) and $c \sim 1/50$ is used, Eq.(2) yields $b \sim 30$ - $100\ R$.

3.3 **Orbit selection**

For ease of optical observations, if from the ground, one would like to assure repeated overflights of selected ground stations. This could be accomplished by placing the tether-carrying satellite at an altitude that yields an integer number of orbits per day, the only two reasonable choices being 279 km for 16 orbits /day, and 572 km for 15 orbits / day. There are no such definite choices, however, for observations from the satellite. Its altitude is then restricted by safety considerations regarding the International Space Station, in orbit at present, and by the need to locate the tether somewhere in the $F1$ ionospheric layer, to attain a maximum e-beam intensity and thus maximum auroral response. Considerations of *ISS* safety made NASA decrease the orbit of its then intended *ProSEDS* tether experiment, following the *Columbia* accident, down to around 300 km. Accordingly, in the previous sections we selected a spacecraft altitude of 305 km, (z_M = 210 km), the proposed 20 km tether extending down to a 285 km altitude.

As regards orbital inclination, a good coverage of mid-latitudes, where natural auroras do not occur, could be of interest. These latitudes are confirmed by other considerations. For an easier tomographic inversion, the line-of-sight angle ψ subtending the footprint at some characteristic emission height 95 km + z_{em}, which is given by (Fig.1)

$$\psi(footprint) \approx \frac{tanI}{1 + tan^2 I} \times \frac{L_t}{z_M - z_{em}}, \qquad (3)$$

should be as large as possible. Equation (3) gives a footprint-angle maximum at $tanI$ = 1, and dropping by just a factor 0.8 at $tanI$ = 0.5 and 2. Ignoring the magnetic dipole tilt, an inclination $i_m \approx i_{orb} = 45°$ yields $tanI_{max} = 2$ and $tanI > 0.5$ over most of the orbit; in Fig.2 one has

$$tan I = \frac{2 sin i_{orb} \times sin\alpha}{\sqrt{1 - sin^2 i_{orb} \times sin^2 \alpha}},$$

with $tanI = 0.5$ at $\alpha = 9.9°$ and $\alpha = 170.1°$.

On the other hand, column brightness in Eq.(2) has basically (as it might be expected) a dependence on I that is the inverse of ψ(*footprint*). With ψ small against I, and $\dot{n}_i \propto \Phi_\infty$ and

$$\Phi_\infty \propto 1/\cos I \times \sqrt{1 + 3\cos^2 I}$$

in chapter **2**, Eq.(2) shows brightness roughly proportional to $(1 + tan^2 I) / tanI$. Hence, if brightness resulted too weak, I values away from 45° might be desired. Note, however, that a higher dip-angle I allows electrons to reach farther down in the atmosphere [see Eq.(4) of chapter **2**], favoring data resolution, and leads indirectly to higher brightness through a decrease in the lower bound in the integral for ionization rate of Eq.(11') in chapter **2**.

Additional considerations relate to the fact that the electron flux is proportional to the induced electric field, E_m, itself proportional to $cosi_m \approx cosi_{orb}$ in the dipole field model, favoring low i_{orb} values. Figure 3 compares values for colum-integrated ionization rates (in Rayleigh-equivalent units) at fixed E_m and values $tanI = 0.5$, 1, and 2, showing a moderate dependence. The peak is indeed broader at $tanI = 1$, the peak itself increasing from $tanI = 0.5$ to 2. A more definite discussion of optimal orbital inclination will require a complete and detailed parametric study.

3.4 **Optical system**

A digital narrow-band CCD-based camera will be used, a refractive system being lighter, simpler and allowing a wider field of view than a reflective one. The major drawback of a CCD device is its serial readout; noise limitation requires a slow

readout. CMOS sensors, which can be read randomly, are faster, and outstand CCD sensors for applications emphasizing aggressive integration but allowing limited image quality. An originally poor CCD response in the UV domain has been lately solved through phosphor (Methachrome II) coating. The camera would operate on three wavelengths in order to determine, in a first simple scheme, both N_2 density ($\lambda = 391.4$ nm or 427.8 nm bands), and O and O_2 densities ($\lambda = 777.4$ nm and 844.6 nm), with definite branching ratios.

A number of lengths will be involved in the optics: focal length f, aperture diameter D, detector side length (image size) l_{det}, pixel size l_{pix}, wavelength λ, distance from emission s (Fig.1) and depth-of-field Δs. The ratio l_{det}/f is determined by the angular field-of-view, $\theta_{fv} \approx l_{det} / f$. Equation (3) above gives a value for the angle $\psi(footprint)$ about 1/18 radians ($\approx$ 3 degrees) for $I = 45°$ and $z_{em} = 30$ km (125 km altitude). As suggested in Fig.1, still larger angles will show substantial emission, a value of 6 degrees covering most emission in Fig.11 of Sec.2. For easying alignment requirements we take about twice as large a field of view (~ 12 degrees),

$$\theta_{fv} = l_{det} / f \approx 1/5. \tag{4}$$

The ratio l_{pix}/f determines the angular resolution

$$\theta_{pix} \approx l_{pix}/f = \theta_{fv} \times l_{pix}/l_{det} \sim \theta_{fv} /N_{\text{pix}}, \tag{5}$$

where

$$N_{\text{pix}} \sim l_{det}/l_{pix}$$

is the number of pixels in each side of the CCD-array. Note that a typical pixel size, l_{pix} ≈ 10 μm, would make θ_{pix} to easily satisfy the Rayleigh criterion,

$$\theta_{pix} > \theta\ (Rayleigh) \sim \lambda / D,$$

$$\rightarrow\ f/D < l_{pix} / \lambda \sim 20, \tag{6}$$

for any reasonable value of the ratio f/D. A standard CCD chip of 10 mm × 10 mm would have $N_{pix} \approx 10^3$, yielding $\theta_{pix} \approx 1/5000$ in Eq.(5); distances about 200 km/5000 ≈ 40 m could thus be resolved horizontally along the beam footprint-track, which is actually an unnecessarily high horizontal resolution because the atmosphere will be homogegeous over quite larger horizontal distances.

Large pixels will prove convenient in section 3.5. We will here consider $l_{pix} \approx 30$ μm (with Rayleigh's criterion even more easily satisfied); using the standard chip size, 10 mm x 10 mm, N_{pix} would then be smaller by a factor 1/3 and θ_{pix} greater by a factor of 3. A small θ_{pix} will also prove convenient. One can keep $N_{pix} \approx 10^3$ and thus θ_{pix} in Eq.(5), by tiling various CCD chips; the signal is read in parallel, and recombined by the software. This way, tiling 9 chips, we would get a detector size of about 30 mm x 30 mm. With $l_{det} \approx 30$ mm, Eq.(4) yields a focal length $f = 15$ cm. Tiling CCD chips is a convenient way to get more use of the focal plane; the Canada-France-Hawaii Telescope will use about 40 2000 × 4500-pixel chips.

The value of the ratio f/D (or f-ratio) is a critical factor in determining the number of photons incident on a detector pixel in a second,

$$\dot{N}_{ph}(pixel) = \frac{10^6}{4\pi} \times b(R) \times A_{pix}(cm^2) \times \Omega(sr) \qquad (7)$$

where A_{pix} is the pixel area, and Ω is the solid angle subtended at the detector by the entrance aperture. We approximately have

$$\Omega \approx \frac{\pi}{(2f/D)^2},$$

so that the total number of photons arriving at a pixel during an exposure time τ_{exp} is

$$N_{ph}(pixel) = \frac{10^6}{16} b(R) \times A_{pix}(cm^2) \frac{\tau_{\exp}(\sec)}{(f/D)^2} T_{optics}, \qquad (8)$$

where T_{optics} is the transmission of the system optics (affected by losses due to reflections and filter attenuation). Clearly, in order to have $N_{ph}(pixel)$ high, a low f-ratio may be needed.

A low f-ratio may produce depth-of-field off-focusing, however. The condition for the off-focusing spot being smaller than a pixel is

$$\frac{\Delta s}{s} \times \frac{f D}{s} < l_{pix}. \qquad (9)$$

In our case, with $\Delta s \sim s$ and $D \sim f \sim 15$ cm, this condition reads

$$s > fD / l_{pix} \sim 1 \text{ km}$$

which is clearly satisfied.

3.5 **CCD measurements**

A number of noise effects could in principle affect measurements. We first note that the brightness values $b \sim 30$ - $100\ R$ indicated in Sec.3.1 are well above the background noise. Also, we note that noise coming from present low values of dark current (pixel electrons escaping spontaneously under their own thermal energy) is completely negligible for the exposure times of interest here. At a temperature of –20°, the CCD dark current might be about 0.1 electrons/pix/s, or about 10^{-2} electrons per pixel for a 0.1 s exposure time. The critical noise thus arises from the CCD readout itself.

To get $N_{ph}(pixel)$ in Eq.(8) as large as possible, for given brightness, one needs large pixel areas and long exposure times, as well as a low ratio f/D. The exposure time cannot be too long, however, because of the satellite motion. We will here tentatively

consider an exposure time of 1/10 s, corresponding to a satellite displacement of 750 m; as previously noticed, atmospheric emission is reasonable homogeneous over large horizontal distances, allowing for relatively long expoure times. Standard "fast" cameras reach as low a *f*-ratio as 1.4. We will simply write $f/D \sim 1$; further reduction might result in unacceptable image distortion. With a pixel area 30 μm x 30 μm and an optics transmission value of 0.5, Eq.(8) yields

$$N_{ph}(pixel) \sim 0.03\, b(R). \qquad (10)$$

For $b \sim 30$ - 100 R, one gets $N_{ph}(pixel)$ 1 -3 photons per pixel. With the quantum efficiency of a CCD being at present close to 100 per cent ($\eta \sim 1$ *electrons/photon*), the pixel charge packet would contain about two electrons.

We now note that the image of the beam foot-track will be very narrow. Whereas the foot-track may extend 20 - 40 km horizontally in the vertical (magnetic-meridian) plane of Fig.1, it will be just about 200 m wide horizontally across, such resolution being unnecessary for the purposes of the measurements. The view angle across, 200 m / 200 km = 1/1000, is 5 times as large as θ_{pix} in Eq.(5). One might then use a "binning" mode (as implemented in almost all commercial chips), which combines several pixels into a "super pixel", summing the photons gathered by nearby pixels with no increase in the reading noise. Summing accross the length of the image one would obtain $\eta\, N_{ph}(super\ pixel) \sim 10$ for the number of electrons in the charge packet of a characteristic super pixel.

The generated photoelectrons are collected at the output register, and converted in an electral signal with a readout error R, given in number of electrons (rms). The charge transferred to the output register is converted to a voltage, which is then amplified and processed by the electronics; the output of the CCD is further digitized and recorded as a number of counts (data numbers). The signal-to-noise ratio is then

$$S/N = \frac{\eta N_{ph}(spix)}{\sqrt{\eta N_{ph}(spix) + R^2}}. \qquad (11)$$

Readout noise varies considerably depending on the model, but its value has been typically under or about 10 *e-* (rms). In our case, one obtains $S/N \approx 1$, which is of course too low.

A recent technique, 'on chip (electron) multiplication' could yield subelectron readout; with $\eta \approx 1$, $N_{ph}(super\ pixel) \sim 10$, Eq.(11) would then give $S/N \sim 3$, which is still low. Image intensifiers, although complex and costly, are usually introduced to increase the low (readout) S/N value of a weak image. The intensifier performs essentially a preamplification of the signal. Third generation intensifiers can achieve a net gain of about 1000. Electrons emitted by a photocathode (on which incoming photons have been imaged) are attracted to a honeycomb of glass channels with resistive coating; cascading down the channels under 1 kV voltage accross, results in a cloud of secondary electrons with a gain of up to 10^4, which then impact the inside of an output window with phosphor coating under a voltage of several keV. Noise introduced by the intensifier tube finally reduces the gain (input image / output image) to a typical value $G_{iccd} \sim 1000$. Considering an intensified CCD, we would thus get a signal-to-noise ratio,

$$S/N = \frac{G_{iccd}\,\eta N_{ph}(spix)}{\sqrt{G_{iccd}\,\eta N_{ph}(spix) + R^2}} \equiv 70, \qquad (12)$$

which is acceptable.

3.6 **Filtering optics**

Optical filters need be used to select specific line or band emissions. For wavelengths in the visible (and near IR and UV) ranges, the spectral width of molecular

bands are about a few nm, whereas line widths are 10 times smaller. Interference filters, as opposed to transmission (absorption) filters, need then be used. Interference filters act as low order Fabry-Perot spectrometers: Resonant cavities formed by two semireflective materials, separated by a submultiple of the wavelength, with a spacer of high refractive index. The filter works as a narrow bandpass with a certain transmitance.

Three filters would be needed: One filter for either the 427.8 nm spectral band or the 391.4 nm band, and two others for the 777.4 nm and the 844.6 nm lines. Three cameras might be used, each one with a single filter. A second solution would be to use adaptative filters which, controlled by hardware, can switch rapidly from one wavelength to the other. A third possibility would be to perform a spectral separation of the incoming radiation using a grating, so that different wavelengths are mapped into different areas of the detector (*Paxton* and *Meng*, Johns Hopkins APL Tech. Digest, 1999). Given the fact that the image is narrow in one direction, the different images at different wavelengths can be made not to overlap; in this way, one dimension of the array provides spectral information while the other dimension would provide spatial information, in the so called multidimensional imaging.

Pioneer in using a multiplicity of cameras for ground survey was the first (Indian) **IRS-1** spacecraft, launched in 1988 and flying at 905 km mean altitude, which carried three Linear-Imaging instruments working in four spectral bands, each band carrying its own optics. The *LISS*-1 instrument was based at the time on a CCD camera with a linear chip of 2048 pixels (l_{det} = 27 mm), a *f*/ratio = 4.5, and f = 16.2 cm. The field-of-view was θ_{fv} = 2.7/16.2 ~ 0.167 (9.5°); the camera thus swept a ground swath of 905 km × 0.167 ~ 150 km. The resolution was 150 km/2048 pixels ~ 72 m/pixel. In order to to double the swath width, two chips were placed alongside. The *LISS*-1 used

one camera for each chip, and one for each of the two bands it worked on, for a total of 4 cameras.

A second instrument, *LISS*-2A, worked on two other bands and was based in a similar arrangement, except that used CCD cameras that differed in the focal length, here $f = 32.4$ cm. This resulted in a greater resolution, 32 m/pixel, but reduced the angular field-of-view and the swath wept, now $4.7°$ and 75 km, respectively. To keep the swath to 150 km, a second identical instrument, *LISS*-2B, was placed aligned with *LISS*-2A, yielding a total of 8 additional cameras for the *LISS*-2 instruments.

2.7 **Sideview observation**

As noted in section 3.2, the signal-to-noise ratio for brightness in sideview observation (from either ground or a second, accompanying satellite) could be increased if tether current (and bias) were time-modulated, with detection conveniently phase-locked. This would require pulsing a Hollow Cathode to be located at the bottom of the tether, so as to reduce bias at bottom to a very low value. When the Hollow Cathode is off, conditions correspond to the analysis in chapter **1**, part 1A. With the Hollow Cathode on, however, electron collection would take place over a substantial tether segment, and overall ion collection woud be negligible (*Ahedo* and *Sanmartin*, J. Space. and Rockets, 2002). This scheme, however, presents two difficulties. First, a second Hollow Cathode and its subsystems would need be located at the bottom, away from the power source at the top. Secondly, night drag would be greatly increased during the Hollow-Cathode *on* periods, when electrons are collected over a large segment of the tether, placing a heavier burden on the power supply system, and increasing the overall system mass.

Independently, and aside from transients related to the Hollow Cathode on/off operation, transients in the pulses of bias and current travelling along the tether could play a complex role in the response of ambient ions, which determine the workings of the tether as a secondary-electron beam source. In order to study such pulses, the tether can be modelled as a transmission line, here much more complex than in previous modelling of pulses in electrodynamic tethers (*Bilen*, Univ. Michigan Ph.D.Thesis, 1998). The equations describing the (now) time dependent bias and current profiles are

$$\frac{\partial \Delta V}{\partial h} = - E_m + R_l I_e + L_l \frac{\partial I_e}{\partial t}, \qquad (13a)$$

$$\frac{\partial I_e}{\partial h} = G_l \Delta V + C_l \frac{\partial \Delta V}{\partial t}, \qquad (13b)$$

to be compared with Eqs.(1) and (2a, b) of section 1A.2 in chapter **2**. Here G_l, representing the conductance per unit tether-length of the transmission line, would be given by the RHS of those equations (2a) or (2b), depending on whether bias is positive or negative, and only if steady conditions have been reached; note that such conductance, being bias dependent, varies along the line. In addition, G_l will be time-dependent during transients.

The resistance per unit length of line is just $R_l = 1 / \sigma A_c$. The conductance per unit length would be $C_l = 2\pi\varepsilon_0 / ln(r_{sh}/R_{eq})$, which is weakly dependent on the argument of the logarithm; here r_{sh} is some characteristic 'sheath' radius, and R_{eq} is some equivalent radius. In steady conditions, under orbital-motion-limited conditions, one has $R_{eq} = p/8$ in our case of a tape; the argument of the logarithm is of the order of $\sqrt{e\Delta V/kT} >> 1$. Similarly, the inductance per unit length is $L_l = ln(r_m/R_{eq}) / 2\pi\varepsilon_0 c^2$, with the logarithm somewhat larger but less well defined (the distance r_m depending in current-circuit closure in the ambient plasma).

If one ignores the conductance term in Eq.(13b) and the weak logarithmic changes in both C_l and L_l the classical tranmissionn-line equation is recovered,

$$\frac{\partial^2 I_e}{\partial h^2} = C_l L_l \frac{\partial^2 I_e}{\partial t^2} + C_l R_l \frac{\partial I_e}{\partial t}. \qquad (14)$$

The (no-loss) phase velocity of the line is

$$v_{ph} = \frac{1}{\sqrt{C_l L_l}} = c \times \sqrt{\frac{\ln(r_{sh}/R_{eq})}{\ln(r_m/R_{eq})}} \approx c,$$

and the time for a wave to travel down the line is $t_w = L_t / c \approx 6 \times 10^{-5}$ s, for $L_t = 20$ km. For such times the ratio between the third and second terms in (14) is the ratio between the resistance $R_l L_t \approx 265\ \Omega$ and the ('no loss') impedance of the transmission line,

$$\sqrt{\frac{L_l}{C_l}} = \frac{\sqrt{\ln(r_{sh}/R_{eq}) \times \ln(r_m/R_{eq})}}{2\pi \varepsilon_0 c} \approx 60\,\Omega \times a\ \log arithmic\ \ factor,$$

which is comparable to the resistance. Pulses should therefore be strongly attenuated. We note that the time t_w is comparable to the time response of ambient oxygen ions to changes in bias, which is a few times $r_{sh}/\sqrt{2e\Delta V/m_i}$, with $r_{sh}/\sqrt{2e\Delta V/m_i} \approx \lambda_D/\sqrt{kT_e/m_e} \sim 10^{-5}$ s for $N_{\infty n} \sim 10^5$ cm^{-3}.

2.8 **Conclusions**

Emission brightness for observation from the spacecraft, should allow a well designed CCD camera with image-intensifier, to form a clear image of emissions produced by the e-beam of the tether; that image could, in principle, allow reconstruction of the vertical structure of the density of neutrals, through tomographic

techniques to be discussed in the next chapter. Sideview observation, either from the ground or from a second satellite presents, however, important disadvantages (need for Hollow Cathode and power suply at tether bottom, substantial increase in tether drag at night operation).

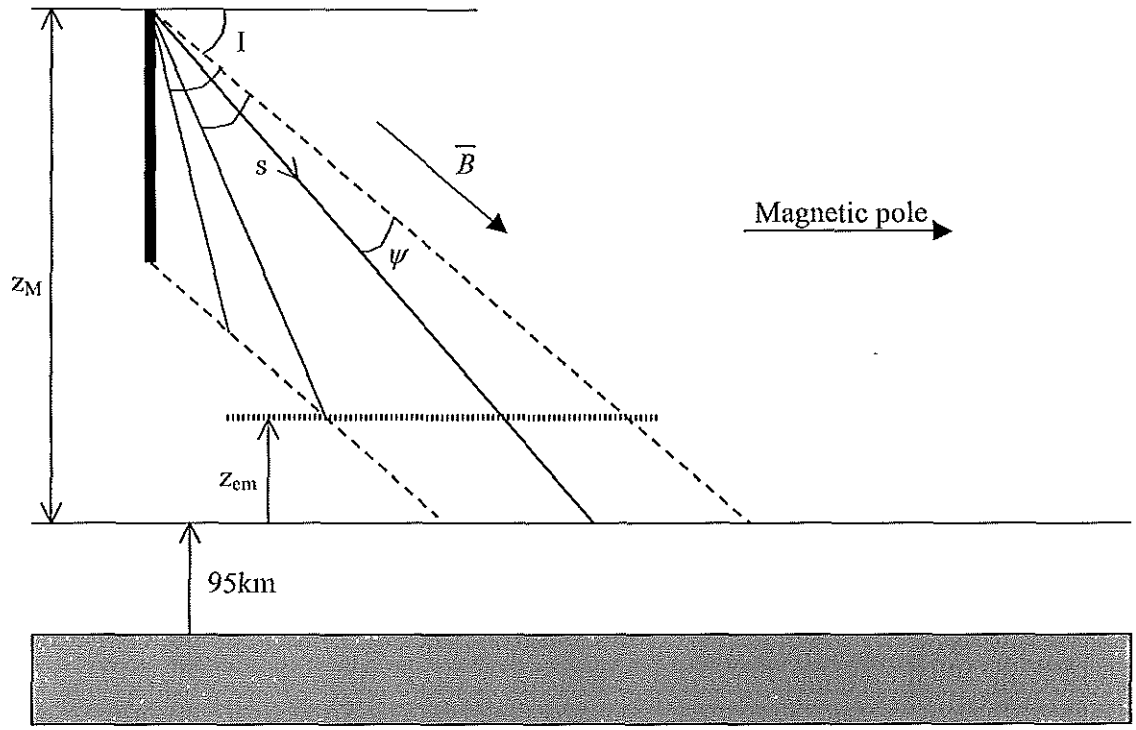

Figure 1

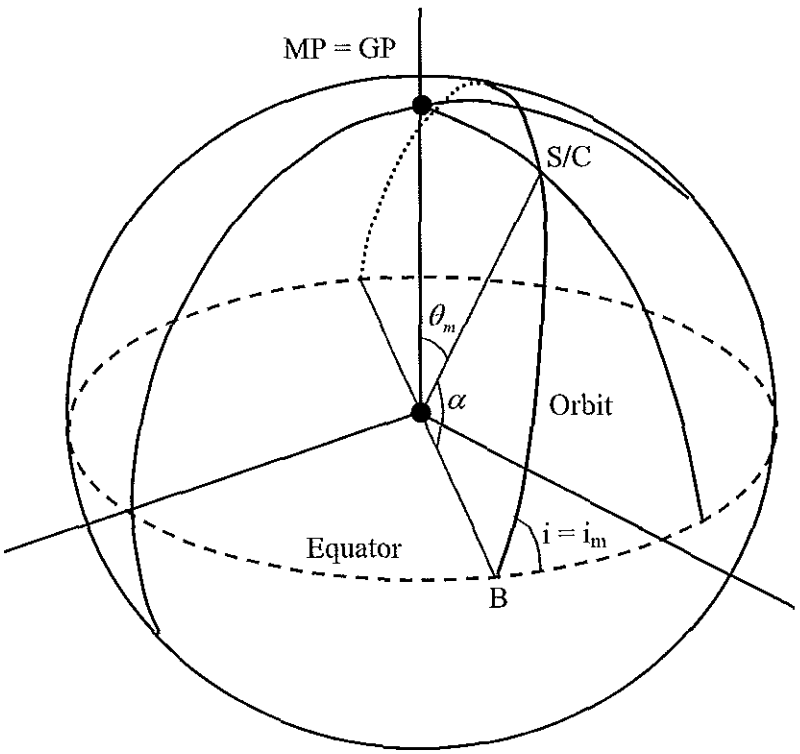

Figure 2

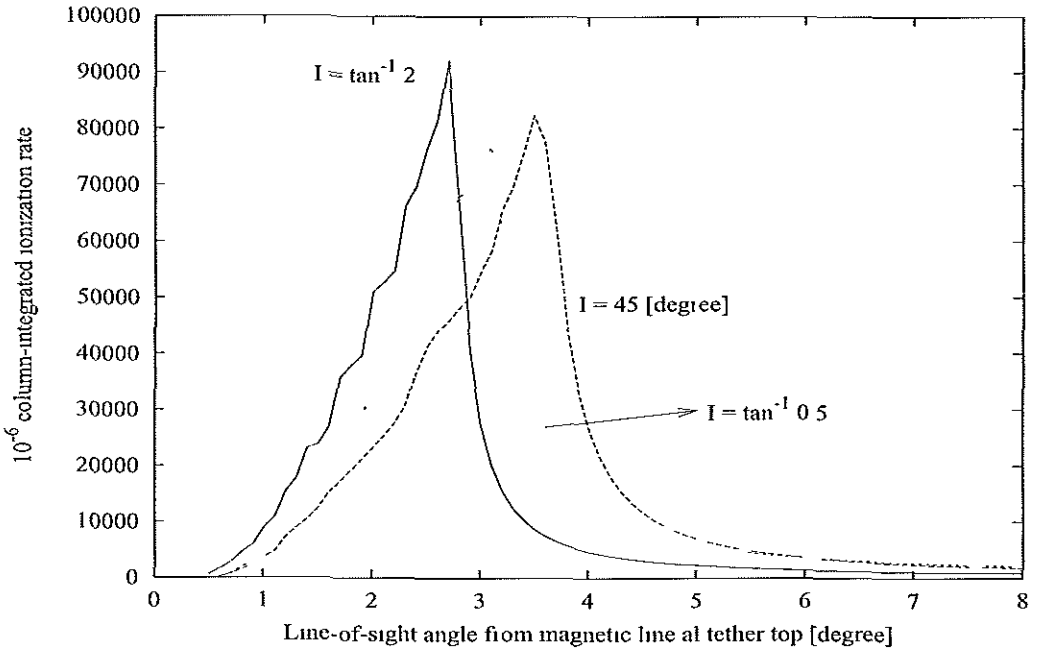
100000
90000
80000
70000
60000
50000
40000
30000
20000
10000
0
0
1
2
3
4
5
6
7
8
10^{-6} column-integrated ionization rate
Line-of-sight angle from magnetic line at tether top [degree]
I = tan^{-1} 2
I = 45 [degree]
I = tan^{-1} 0 5

Figure 3

4 Tomography algorithm (WP-300)

4.1 Introduction

Use of tethers was proposed in the past for high-resolution, global density mapping of some ionospheric species; a dual platform configuration would have a shuttle-based laser excite a column of the atmosphere adjacent to a tethered satellite, with triangulating photometric detectors on the satellite employed to measure the fluorescence from sections of the column (*McComas, Spence, Karl, Horak* and *Wilkerson*, Rev. Scientific Instr., 1985). In an electron-beam experiment on sounding parallel electric field structures within the auroral acceleration region, a tether would be used to keep the beam source payload and the diagnostics away from each other, overcoming one of the defficiencies of standard e-beams sources (*Habash, Neubert, Gilchrist* and *Raitt*, Proc. Fourth Int. Conf. on Tethers in Space, 1995); previous arrangements had beam source and diagnostics placed close, resulting in possible contamination of sensitive optical measurements due to the luminous glow produced by the electron bombardment of the return current.

Independently of tether applications, a range of tomographic inversion algorithms dealing with atmospheric emissions have been worked out. They depend heavily on the observation system used and may involve consideration of how backscatter from both the Earth's surface and clouds contaminate measurements. The *UVISI* instruments on board the *Midcourse Space Experiment* has provided data to test operational concepts and algorithms for use with later experiments (*Paxton* and *Meng*, Johns Hopkins APL Tech. Digest, 1999). A basic problem in optical tomography is a defficiency in information, resulting from limitations in the number of line-of-sights, the angular range, and the level of noise in projections; this makes necessary, in general, to

include a priori information in the reconstruction algorithms (*Alpatov* and *Romanovsky*, Adv. Space Res., 1998).

The Swedish ALIS system (Auroral Large Imaging System) consists of a ground-based network of automated stations (*Aso, Steen, Brandstrom, Gustavsson, Urashima* and *Ejiri*, Adv. Space Res., 2000). There are six unmanned, remote-controlled stations that enable locating auroral phenomena by triangulation, as well as extracting altitude information by a tomographic inversion technique. The inversion algorithm yields volumetric emission rates using an iterative reconstruction analysis that considers measurements from the entire ground system. The algorithm is a modified version of an inversion technique, SIRT (Simultaneous Iterative Reconstruction Technique), developed by Gilbert (1972). ALIS differs fundamentally from our intended system, which must deal with a set of line-of-sight brightness measurements from one (satellite) observation location, instead of combining information from several ground stations.

For photometry carried out from a satellite in orbit, a method has been developed, based on Cormack inversion (*Solomon, Hays* and *Abreu*, Applied Optics, 1984), which has been used with *Explorer* satellites. In this technique, knowledge of several sets of line integrals from different satellite observation locations allows to determine the volumetric rate of photon emission. Calling this emission rate $g(r, \theta)$, line integrals $f(p,\phi) = \int g(r, \theta)ds$, will be proportional to values of brightness obtained from measurements. The parameter p is the perpendicular distance from Earth's center to the particular line considered, as shown in Fig. 1, representing the orbital plane; r is radial distance for a generic emission point; and angles θ and ϕ are measured from some reference direction. Calling the n^{th} coefficient of the Fourier series expansion of

$f(p, \phi)$ with respect to ϕ, $F_n(p)$, and the n^{th} coefficient of the Fourier series expansion of $g(r, \theta)$ with respect to θ, $G_n(r)$, one can readily derive the relation

$$G_n(r) = -\frac{1}{\pi}\frac{d}{dr}\int_r^\infty \frac{r F_n(p) T_n(p/r)\,dp}{p(p^2 - r^2)^{1/2}}, \tag{1}$$

where $T_n(p/r)$ is the n^{th} Chebyshev polynomial.

The last equation can be rewritten by differentiation under the integral and integration by parts,

$$G_n(r) = -\frac{1}{\pi}\int_r^\infty \frac{\frac{d}{dp} F_n(p) T_n(p/r)\,dp}{(p^2 - r^2)^{1/2}}. \tag{2}$$

Knowledge of (brightness) line-integrals allows determining the volumetric emission rate. For instance, in the particular case of g not depending on θ, one would immediately find, using $T_0(p/r) = 1$,

$$g(r) = -\frac{1}{\pi}\int_r^\infty \frac{\frac{d}{dp} f(p)\,dp}{(p^2 - r^2)^{1/2}}, \tag{3}$$

which is the well known Abel inversion. Difficulties that arise from the singularity at $p = r$ are solved by fitting parabolic splines to the function $F_n(p)$. In general, use of properties of Chebyshev polynomials leads in a straightforward manner to a set of algebraic equations that can be solved iteratively.

A basic point to notice here, however, is that the function $g(r, \theta)$ at any particular $r = r_0$ (Fig.1), only depends on those line integrals with $p > r_0$, as seen in Eq. (2). This makes the present technique suitable for limb measurements only. An advantage of limb scans is that they are less contaminated by backscatter from clouds, and from the Earth surface, than nadir scans (for emission layers that have a non negligible horizontal extent). Since magnetic-dip angles are not small for the cases of interest, our

measurements are taken (from a single observation point) along lines that intersect the Earth surface, and are, unfortunately, suitable to nadir-scan models only.

In nadir satellite photometry, the problem of how to remove backscatter effects of diffuse light coming from snow on the Earth surface, or from clouds, to determine emission brightness from values of measured brightness, has been addressed in the past (*Hays and Anger,* Applied Optics, 1978). A planar, infinite, non uniform and optically thin surface emission layer is considered, located at constant height z above the ground surface (or above top clouds), which is regarded as Lambertian with constant albedo α. These conditions yield

$$B_m(\bar{r}) = B_a(\bar{r}) + \frac{\alpha z}{\pi} \int\int_{-\infty}^{+\infty} B_a(\bar{r}_a) \frac{1}{\left[(\bar{r}-\bar{r}_a)^2 + z^2\right]^{\frac{3}{2}}} d\bar{r}_a \,, \tag{4}$$

where $\bar{r}$ is the point where measurements are performed and $\bar{r}_a$ is any point on the emission layer. Note that these vectors are both bidimensional; volumetric effects, and thus usual tomography, are not involved here. B_a is brightness or luminosity of the emission layer and B_m is the brightness measured.

The second term on the right-hand-side of the last equation is the effect of backscattering. It is easy to check that this effect is not negligible, and must be taken into account when lines-of-sight intersect the ground, provided the albedo is not small and the horizontal extent of the emission layer is large enough. Equation (4) can be inverted using Fourier-transform and convolution properties of this kind of transformation,

$$B_a(\bar{r}) = B_m(\bar{r}) - \int\int_{-\infty}^{+\infty} B_m(\bar{r}_a) W_2^{-1}(|\bar{r}_a - \bar{r}|)\, d\bar{r}_a \,, \tag{5}$$

where

$$W_2^{-1}(\rho) = \frac{\alpha}{\pi} \int_0^\infty \frac{k J_0(k\rho) \exp(-kz)\, dk}{1 + 2\alpha \exp(-kz)}; \tag{6}$$

here, J_0 is the Bessel function of the first kind and zero order. With an onedimensional emission layer, that is, when brightness of the layer varies in just one dimension, the kernel function takes the simpler form

$$W_1^{-1}(\rho) = \frac{2\alpha}{\pi} \int_0^\infty \frac{\exp(-kz)\cos(k\rho)dk}{1 + 2\alpha \exp(-kz)}. \tag{7}$$

The previous algorithm has been generalized to take into account volumetric scatter in the atmosphere, using not quite-nadir observations (a range of line-of-sights near the vertical), resulting in an apparent displacement of the emission layer (a parallax effect), different for each direction (*Abreu and Hays*, Applied Optics, 1981). It is also possible to determine the Earth albedo, combining limb and nadir observations (*Solomon, Hays* and *Abreu*, Applied Optics, 1985). Limb brightness measurements allow to obtain a first approximation of volume emission rate using the Cormack inversion, that rate being then used to fit nadir brightness measurements. In any case the small horizontal extent of the emission layer in our problem (a thin ribbon about 30 km wide and 200 m thick) means that backscatter may be fully ignored here.

4.2 **The bare-tether inversion problem**

As it follows from the analysis in previous chapters, we want to determine the neutral density vertical profile $n(z)$, from the knowledge of a set of scan lines (column-integrals), from one observation location, for particular bands or lines, with each emission rate proportional to the ionization rate, $\dot{n}_{em} = c\,\dot{n}_i$. In principle, we would need a number of bands or lines equal to the number of dominant neutral species at the heights of interest, probably sufficing to consider N_2, O_2 and O. Here we focus on the mathematical problem of inversion for the particular conditions of our problem. We

thus assume that there is only one species and that we know the dimensionless factor c relating the emission and ionization rates. Using results from Ch.2, we may then write the column brightness, at an angle $I+\psi$ from the horizontal, as

$$b_\psi(R) \equiv 10^{-6} c \times \int \dot{n}_i \frac{dz}{\sin(I+\psi)}. \tag{8}$$

The basic difference with the analysis of Ch.2 is that we took there a nominal density law $n(z) \equiv 10^{31}/z^3$ whereas we here assume $n(z)$ unknown (as in Ch.2, z is measured from 95 km above Earth's surface). In order to explicitly write down the ionization rate inside the integral in Eq.(8), we first recall all functions introduced in Ch.2. The electron energy was written as $\varepsilon = \varepsilon_* \times \tilde{\varepsilon}(z;h,\mu)$, with the dimensionless function $\tilde{\varepsilon}$ given now by the equation

$$\int_{\tilde{\varepsilon}(z;h,\mu)}^{\tilde{\varepsilon}_\infty(h)} \frac{du}{g(u)} = \frac{\tilde{\varepsilon}_i \sigma^*}{\mu \sin I} \times \int_z^{z_\infty(h)} n(z')dz', \tag{9}$$

where $\tilde{\varepsilon}_\infty(h)$ is $eE_m h/\varepsilon_*$, $z_\infty(h)$ is $z_M - h$, μ is the cosine of the electron pitch-angle, and the function $g(u)$ describing the cross-section energy dependence is

$$g(u) = \frac{u-1}{u^2} \ln u.$$

Equation (9) results from integrating the rate of energy loss of secondary electrons in non-elastic collisions,

$$\frac{d\tilde{\varepsilon}}{dz} = \frac{\tilde{\varepsilon}_i \sigma^*}{\mu \sin I} \times n(z)\, g(\tilde{\varepsilon}). \tag{10}$$

Scattering effects that are responsible for beam-broadening are described by a factor involving $\tilde{\varepsilon}$,

$$f_{br}[\tilde{\varepsilon}(z;h,\mu),\tilde{\varepsilon}_\infty(h)] = \sqrt{1 + \frac{2/3}{\tilde{\varepsilon}_i \tilde{\varepsilon}_\infty(h)} \times \int_{\tilde{\varepsilon}(z;h,\mu)}^{\tilde{\varepsilon}_\infty(h)} \frac{u du}{g(u)}}. \tag{11}$$

In addition we need the electron flux leaving the tether $\Phi_\infty(h)$, which is explicitly given as

$$\Phi_\infty(h) = \sqrt{\frac{m_e}{m_i}} \frac{N_{\infty n}\, p\, \Omega_{eq} \times \gamma_1\, E_m\, h}{2\pi \cos I \sqrt{1 + 3\cos^2 I}}, \tag{12}$$

and the geometric relation $h(z; \psi)$ valid along each integration line corresponding to any given ψ,

$$h(z;\psi) = (z_M - z)\left[1 - \frac{tan\, I}{tan(I + \psi)}\right]. \tag{13}$$

Equations (9)-(13) are used in writing down the volumetric ionization rate, which, in the isotropic-pitch model, accounting for scattering effects too, takes the form

$$\dot{n}_i(z;\, h) = \Phi_\infty(h) \times n(z) \times \int_{\mu_{min}(z;h)}^{1} \frac{2}{\pi} \frac{\sigma * d\mu}{\sqrt{1 - \mu^2}} \frac{g[\tilde{\varepsilon}(z;\, h, \mu)]}{f_{br}[\tilde{\varepsilon}(z; h, \mu), \tilde{\varepsilon}_\infty(h)]}, \tag{14}$$

where $\mu_{min}(z;\, h)$ is given by

$$\tilde{\varepsilon}[z; h, \mu_{min}] = \tilde{\varepsilon}_i \approx 1.5. \tag{15}$$

Everywhere in Eq.(14) h is given in terms of z (and ψ) by Eq.(13). Introducing (14) in Eq.(8) one gets the brightness as a definite integral

$$b_\psi(R) \propto \int_{z_{min}(\psi)}^{z_{max}(\psi)} \dot{n}_i \frac{dz}{sin(I + \psi)}, \tag{16}$$

with the integration limits $z_{max}(\psi)$ and $z_{min}(\psi)$ given by the roots of the following equation,

$$\tilde{\varepsilon}[z; h(z;\psi), 1] = \tilde{\varepsilon}_i. \tag{17}$$

4.3 **The direct inversion algorithm**

The full inversion problem is complex, even if one were to introduce simplifications such as taking some average value for f_{br} out of the integral in (14), or

using the approximation in the LHS of Eq.(10) of chapter **2** for the LHS of (9). As noticed there, the unknown function $n(z)$ enters the integral giving the brightness both explicitly, and implicitly through the function $\tilde{\varepsilon}(z,h,\mu)$ defined by (9). This function itself enters Eq.(16) in two ways: through the factor-functions g and f_{br} in Eq.(14), and through limits of integration, $\mu_{min}(z;h)$ in (14), and $z_{max}(\psi)$ and $z_{min}(\psi)$ in (16).

Consider now how to solve Eq.(16) for $n(z)$. Since we have just a finite set of brightness measurements, inversion of equation (16) is an ill-posed problem and the determination of $n(z)$ can only be carried out with some a priori knowledge about the function, say, its stability or its smoothness. We take as unknowns a set of density values $\hat{n}_r$ at points z_r, with $r = 1,...,\ N_{pix}$, where N_{pix} is the number of pixels along one side of the CCD detector (measurements of brightness at N_{pix} values of ψ). The set of points z_r is selected in some such way that there are more points where density variations are stronger. All other values of $\hat{n}(z)$ are interpolated and extrapolated. Extrapolation is necessary because during iteration the limits of integration for each line of sight, in determining the brightness, could go outside the density range in the previous iteration step. In both interpolation and extrapolation one uses rational z functions, which result in lower errors for the expected density profiles.

We use an iterative solution scheme. Consider the following equation derived from (16)

$$b_\psi = \int_{z^m{}_{min}(\psi)}^{z^m{}_{max}(\psi)} \hat{n}^{m+1}(z)\, K^m\left[z,\psi;\hat{n}^m(z)\right]dz\,. \qquad (18)$$

Here, b_ψ is the measured brightness (except for some proportionality constant) and the superscript m is the iteration step. K^m is a *kernel* function evaluated using the estimated density $\hat{n}^m$ at step m. The construction of the kernel function at each step

is considered below. We note that $z^m{}_{max}(\psi)$ and $z^m{}_{min}(\psi)$ must be also evaluated at each step.

Once the kernel and the integration limits are known, and using some approximate numerical-quadrature rule,

$$\int_{a_S}^{b_S} y(s)ds = \sum_{r=1}^{N_{pix}} w_{r,s}\ y(s_r), \qquad s = 1,..., N_{pix}, \tag{19}$$

Eq.(18) can be written as

$$\sum_{r=1}^{N_{pix}} \tilde{K}_{r,s}{}^m\ \hat{n}_r{}^{m+1} = b_s, \qquad s = 1,....., N_{pix}, \tag{20}$$

where

$$\tilde{K}_{r,s}{}^m = K_{r,s}{}^m\ w_{r,s}{}^m, \tag{21}$$

and $b_s = b(\psi_s)$.

The linear system (20) can be solved using a suitable linear solver, yielding the next approximation of density. Finally, a convergence check can be performed, requiring that the inequality $\left\|\hat{n}^{m+1} - \hat{n}^m\right\| < \varepsilon_{conv}$ be satisfied for some specified small quantity ε_{conv}. If the convergence criterion is not reached, a new iteration must be performed.

The kernel function is

$$K_{r,s}(z_r;\ h_{r,s}) = \frac{\Phi_\infty(h_{r,s})}{sin(I+\psi)} \times \int_{\mu_{min}(z_r;h_{r,s})}^{1} \frac{2}{\pi} \frac{\sigma * d\mu}{\sqrt{1-\mu^2}} \frac{g\left[\tilde{\varepsilon}^m(z_r;\ h_{r,s},\mu,)\right]}{f_{br}[\tilde{\varepsilon}^m(z_r;h_{r,s},\mu),\tilde{\varepsilon}_\infty(h_{r,s})]} \tag{22}$$

where

$$h_{r,s} = (z_M - z_r)\left[1 - \frac{tan\, I}{tan(I+\psi_s)}\right]. \tag{23}$$

Energy itself is obtained iteratively from Eq.(9) using Newton's method

$$\tilde{\varepsilon}_{r,s}^{\,m,l+1} = \tilde{\varepsilon}_{r,s}^{\,m,l} + g\left(\tilde{\varepsilon}_{r,s}^{\,m,l}\right)\left[\int_{\tilde{\varepsilon}_{r,s}^{m,l}}^{\tilde{\varepsilon}_\infty(h_{r,s})} \frac{du}{g(u)} - \frac{\tilde{\varepsilon}_i \sigma^*}{\mu\ sinI}\int_{z_r}^{z_\infty(h_{r,s})} \hat{n}^m(z')dz'\right]. \qquad (24)$$

In the above equation, superscript l represents each step in Newton's iteration, and we wrote $\tilde{\varepsilon}_{r,s}^{\,m} = \tilde{\varepsilon}(z_r; h_{r,s}, \mu,)$ with superscript m standing for use of the m^{th}-iteration for the density in Eq.(9). To evaluate (22) we also need μ_{min}, as obtained from Eq. (15),

$$\mu_{min}(z_r; h_{r,s}) = \frac{\tilde{\varepsilon}_i \sigma^*}{sinI} \frac{\int_{z_r}^{z_\infty(h_{r,s})} \hat{n}^m(z')dz'}{\int_{\tilde{\varepsilon}_i}^{\tilde{\varepsilon}_\infty(h_{r,s})} \frac{du}{g(u)}}. \qquad (25)$$

The integration limits, $z^m{}_{max}(\psi_s)$ and $z^m{}_{min}(\psi_s)$ can be determined, again iteratively using Newton's method. From Eqs.(9) and (17), we get Eq.(26),

$$\tilde{z}_s^{\,m,l+1} = \tilde{z}_s^{\,m,l} + \frac{\int_{\tilde{\varepsilon}_i}^{\tilde{\varepsilon}_\infty(h_s^{m,l})} \frac{du}{g(u)} - \frac{\tilde{\varepsilon}_i \sigma^*}{sinI}\int_{\tilde{z}_s^{m,l}}^{z_\infty(h_s^{m,l})} \hat{n}^m(z')dz'}{\left(1 - \frac{tanI}{tan(I+\psi)}\right)\frac{1}{g(\tilde{\varepsilon}_\infty)} + \frac{\tilde{\varepsilon}_i \sigma^*}{sinI}\left[\left(1 - \frac{tanI}{tan(I+\psi)}\right)\hat{n}^m(z_\infty) - \hat{n}^m(\tilde{z}_s^{\,m,l})\right]}.$$

Estimates of initial values for $z^m{}_{max}(\psi_s)$ and $z^m{}_{min}(\psi_s)$ would be obtained using a bracketing algorithm. It may be advantageous to readjust mesh points to fit the new range established by $z^m{}_{max}$ and $z^m{}_{min}$ at each step m. Finally, one might in principle try using the inverse-cubic density law, as a convenient initial guess in constructing the kernel and determining the integral limits in (18).

The entire scheme is showed in Fig. 2. Some topics about numerical methods can be found in *Press, Teukolsky, Vetterling* and *Flannery*, Numerical Recipes, 1988.

4.4 **A two-step scheme**

We find that the direct inversion algorithm faces two hurdles. First, we find that for any reasonable density profile, the kernel K, which is density dependent, is numerically singular: There are linear combinations of rows or columns with values of the order of round-off errors in the machine carrying out the calculation. This relates to the fact that, as a result of broadening, the peak of brightness versus line-of-sight angle has been flattened considerably, as seen in Fig.11 of Ch.2. The problem then appears as an ill-posed one; any attempt to solution through direct methods (Gauss-Jordan, LU decomposition) is bound to fail.

To overcome this first hurdle, one may use a **SVD** (Singular Value Decomposition) regularization technique. A well established theorem from algebra allows one to write any square matrix A like ours as a product,

$$A = U W V^T, \tag{26}$$

where W is a diagonal matrix, all its elements, w_i, being positive or null; V^T is the transpose of V; and U and V are unitary matrices ($U U^T = V V^T$ = unit matrix, for our real **A** case). The matrix A is singular when one w_i element at least vanishes. Actually, it suffices that the condition number for A (that is, the ratio between the greater and the smaller of the W elements) has an inverse of the order of the round-off error in the machine (or, in practice, of the order of the typical error in the measurements).

The SVD technique to convert an ill posed problem into a well posed one provides a so called quasi-solution to the equation

$$A x = b, \tag{27}$$

with A singular and x unknown (*Herman, Tuy, Langenberg* and *Sabatier*, Basic Methods of Tomography and Inversion Problemas, 1987). After writing A as in (26), the quasisolution to (27) is

$$x = V W' U^T b, \tag{28}$$

where W' is a diagonal matrix with

$$w_i' = 1 / w_i \qquad \text{for} \quad w_i \geq \varepsilon\, w_{i,max},$$

$$w_i' = 0 \qquad \text{for} \quad w_i < \varepsilon\, w_{i,max},$$

where $w_{i,max}$ is $max\{w_i\}$ and ε is a conveniently chosen, small constant of the order of the round-off error. For A singular and (27) a system of equations incompatible, as, in general, in our case, the above solution makes $|A\,x - b|$ minimum.

A second hurdle facing the direct inversion algorithm lies in the fact that the iteration process is found not converge if the initial guess for the density profile introduced in the kernel K lies 'too far' from the actual profile; this appears to be a result of the highly nonlinear dependence of K on the density profile. To overcome this second hurdle, we now suggest to carry out the tomographic inversion in two steps. First, a rough estimate of the actual density profile is obtained by fitting parameters in a model of the density profile in such a way that the brightness resulting from that model be as close as possible to the actual brightness. This estimate is then used as initial guess for the kernel K to start the iteration of the regularized inversion process.

It is essential to the estimate of the actual density $n(z)$ that it makes no recourse to matrix inversion, the numerical process requiring direct evaluation of brightness only. One fits parameters in some parametric model of the density, $\hat{n}(z,\ \alpha_1\ \alpha_2\ \alpha_3,...)$, so as to make minimum some measure of the difference between the brightness it yields and the actual brightness. One looks for values of α_1, α_2, α_3,... such that $\hat{n}(z,\ \alpha_1\ \alpha_2\ \alpha_3,...)$ makes minimum the multidimensional function

$$f(\alpha_1, \alpha_2, \alpha_3,...) \equiv \sum_{i=1}^{i=N} \left(\hat{b}_i - b_i\right)^2, \tag{30}$$

where N_{pix} is the number of lines-of sight, $b_i \equiv b(\psi_i)$ the actual brightness values, and $\hat{b}_i$ the corresponding brightness for the model density.

In order to determine the α_1, α_2, α_3,...values at the f minimum, one uses a *Direction Set* (*Powell*) technique. This technique is based on two algorithms. First, one makes f minimum along some line in the parametric space using the *Brent* algorithm, which does not require introducing the partial derivatives $\partial f / \partial \alpha_j$, and then uses a method to choose the next line in the parametric space along which make f minimum. The *Brent* algorithm itself combines two methods: 1) a parabolic approximation to the function f from values at three points (resulting in a quadratic convergence), taking the minimum of the parabola for the next estimate of the overall minimum, and 2) a *golden section search* for those parameter intervals where the parabolic approximation gives no satisfactory results; this second method looks for subintervals where the value of f in the central point is inferior to its values at the end points (*Press, Teukolsky, Vetterling* and *Flannery*, Numerical Recipes, 1988).

4.5 Simulated numerical examples

To reduce the calculational time we simplify the heavy calculations by taking only 15 lines-of-sights (equally spaced between angles $\psi = 1°$ and $\psi = 10°$) instead of a typical number $\sim 10^3$. We first present a simple numerical example of the *Brent* method for a two-parameter density model, $\hat{n} = C/z^{\alpha}$, which can actually be reduced to a one-parameter model. For a given density profile, Eq.(9) determines the dimensionless energy,

$$\tilde{\varepsilon} = \tilde{\varepsilon}(z; h, \mu),$$

with no ionization (hence, no emission) for $\tilde{\varepsilon}$ less than 1.5, and, therefore, no emission below z_{Min} given by the equation $\tilde{\varepsilon}(z_{Min}; L_t, 1) = 1.5$. For our model density

one then finds z_{Min} as a function of both C and α. By setting $h = L_t$ and $z = z_{Min}$ in Eq. (13) relating ψ, z, and h, one next determines the angle $\psi(z_{Min}) = \psi(C, \alpha)$. We finally take this angle for the angle corresponding to the line-of-sight with the actual maximum brightness, $\psi(b_{max})$. Writing $\psi(z_{Min}) = \psi(b_{max})$ one obtains

$$C = C[\alpha, \psi(b_{max})].$$

The 'actual' profile density used in the calculations is

$$n(km^{-3}) = \frac{10^{31}}{[z(km)]^3} \times \frac{2}{1 + z(km)/210},$$

with $\hat{n}(km^{-3}) = C(\alpha)/[z(km)]^{\alpha}$. Figure 3 presents numerical results for f versus α, showing a minimum for α very close to 4. The best estimate of the density profile resulting from parameter fitting is

$$n(km^{-3}) = \frac{0.75\times10^{31}}{[z(km)]^3} \times \left(\frac{210}{z(km)}\right)^{0.97}.$$

To illustrate the regularization technique we computed brightness for an 'actual' density profile,

$$n = 10^{31}/z^3, \qquad \text{or} \qquad n(\mathrm{m}^{-3}) = 10^{22}/[z(\mathrm{km})]^3. \tag{29}$$

The round-off error in the calculations was of the order of 10^{-7}, corresponding to single precission. The inverse of the condition number of the kernel matrix was found to be 8.392×10^{-7} which is comparable, and therefore the matrix is numerically singular. Although regularization was achieved, convergence required using a density profile extremely close (with relative differences of about 10^{-3}) to the 'actual' profile, as initial one in computing the kernel K to start iterations. Table I shows results of two iteration steps.

4.6 **Conclusions**

It appears that a two step algorithm, with 1) a direct estimate of the actual density profile yielding a measured brigthness peak, previous to the iteration process involved in the inversion algorithm, and 2) a regularization of the near singular matrix used in that algorithm, can determine the profile. However, when using a limited number of line-of-sights, and correspondingly describing the profile by density values at just 15 altitudes (as against an actual typical value of about 10^3), in order to reduce the calculational time, convergence in the iteration required estimated (initial) density values extremely close to the actual ones. This appears to be a result of crudely describing a profile that covers over two orders of magnitude by giving values at just 15 altitudes.

Use of 10^3 line-of-sights and densities while keeping the calculation as a reasonable task would require adopting a new calculational scheme. At every iteration, each element (one among $10^3 \times 10^3$ elements) in the kernel-matrix K in (22) corresponds to an altitude and a line-of-sight, and through Eq.(23), to an altitude and an h value. In the scheme of Sec.4.3, and setting aside the additional complication of the μ-quadrature, determining any K-element in (22) requires solving Eq.(24) (which involves a quadrature) by iterating in Newton's method, in order to find the energy at the given z - h values, for use in both the g and f_{br} functions. A similar difficulty is involved in solving Eq.(26). A much simpler, though less precise scheme, would first readily determine energy in a h-z grid by choosing a set of h values and carrying out direct, upwind integration of Eq.(10) up to a similar set of z values. Further numerical work would be necessary to confirm convergence in the new scheme.

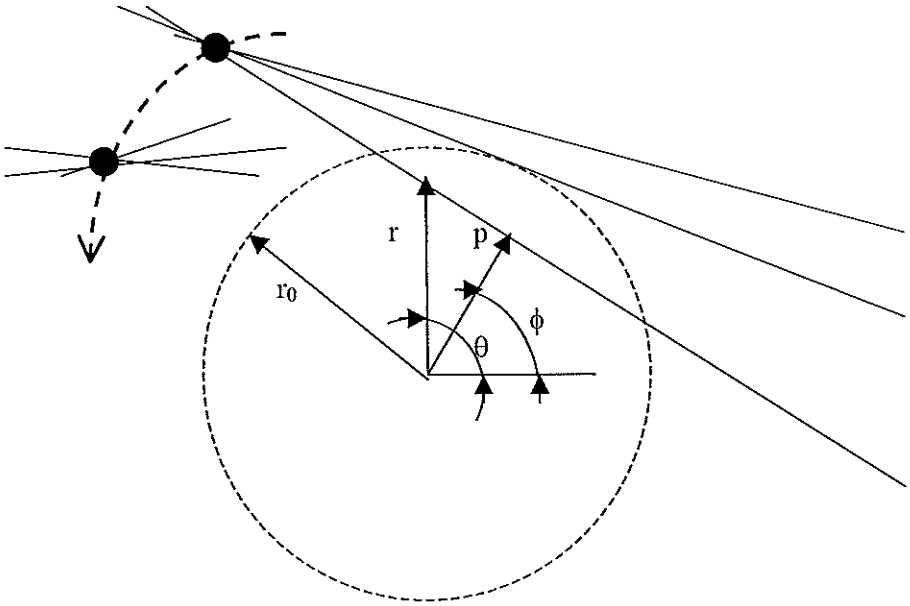

Figure 1

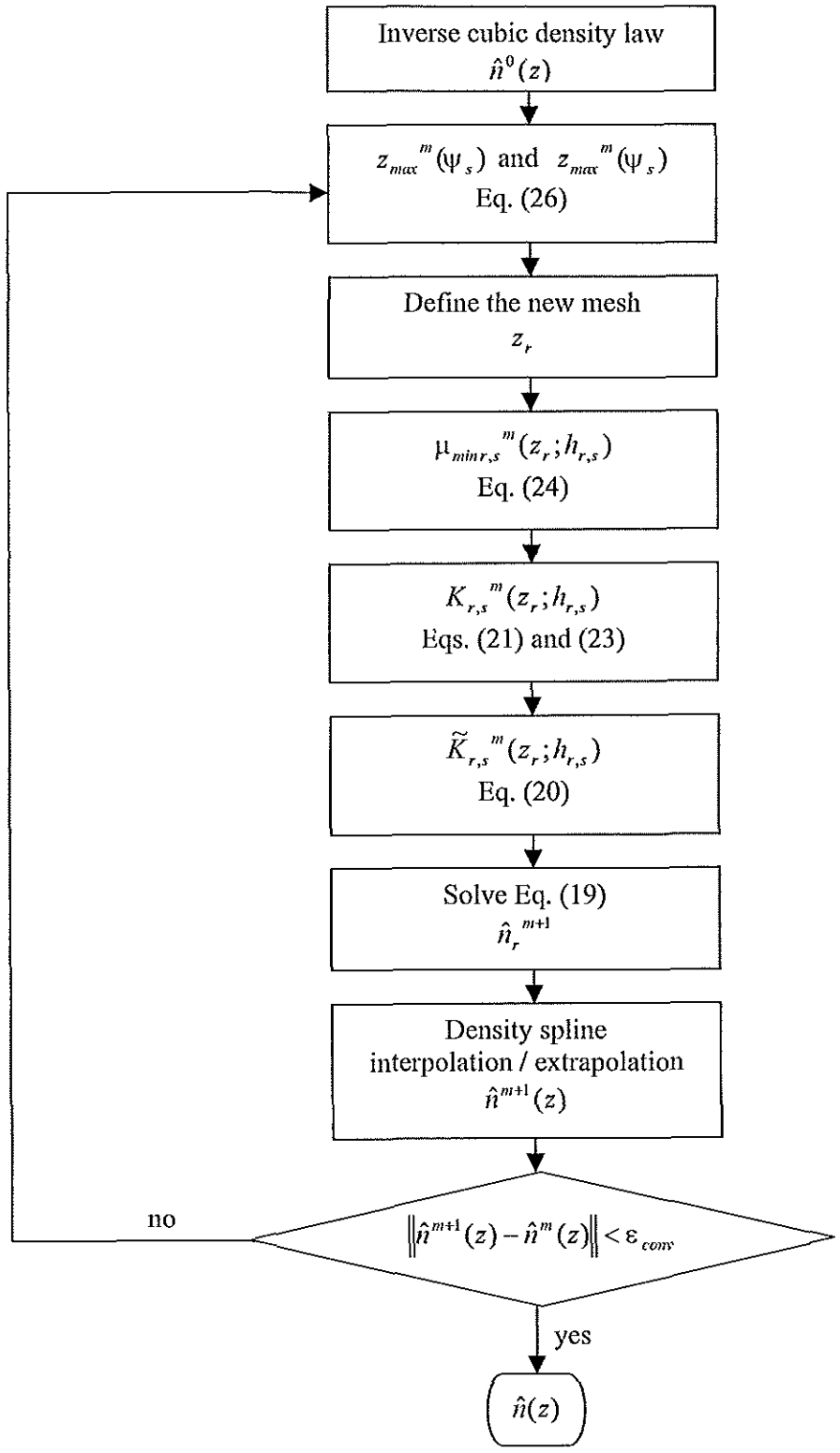
Inverse cubic density law
$\hat{n}^0(z)$
$z_{max}{}^m(\psi_s)$ and $z_{max}{}^m(\psi_s)$
Eq. (26)
Define the new mesh
z_r
$\mu_{minr,s}{}^m(z_r;h_{r,s})$
Eq. (24)
$K_{r,s}{}^m(z_r;h_{r,s})$
Eqs. (21) and (23)
$\tilde{K}_{r,s}{}^m(z_r;h_{r,s})$
Eq. (20)
Solve Eq. (19)
$\hat{n}_r{}^{m+1}$
Density spline
interpolation / extrapolation
$\hat{n}^{m+1}(z)$
no
$\left\|\hat{n}^{m+1}(z)-\hat{n}^m(z)\right\|<\varepsilon_{conv}$
yes
$\hat{n}(z)$

Figure 2

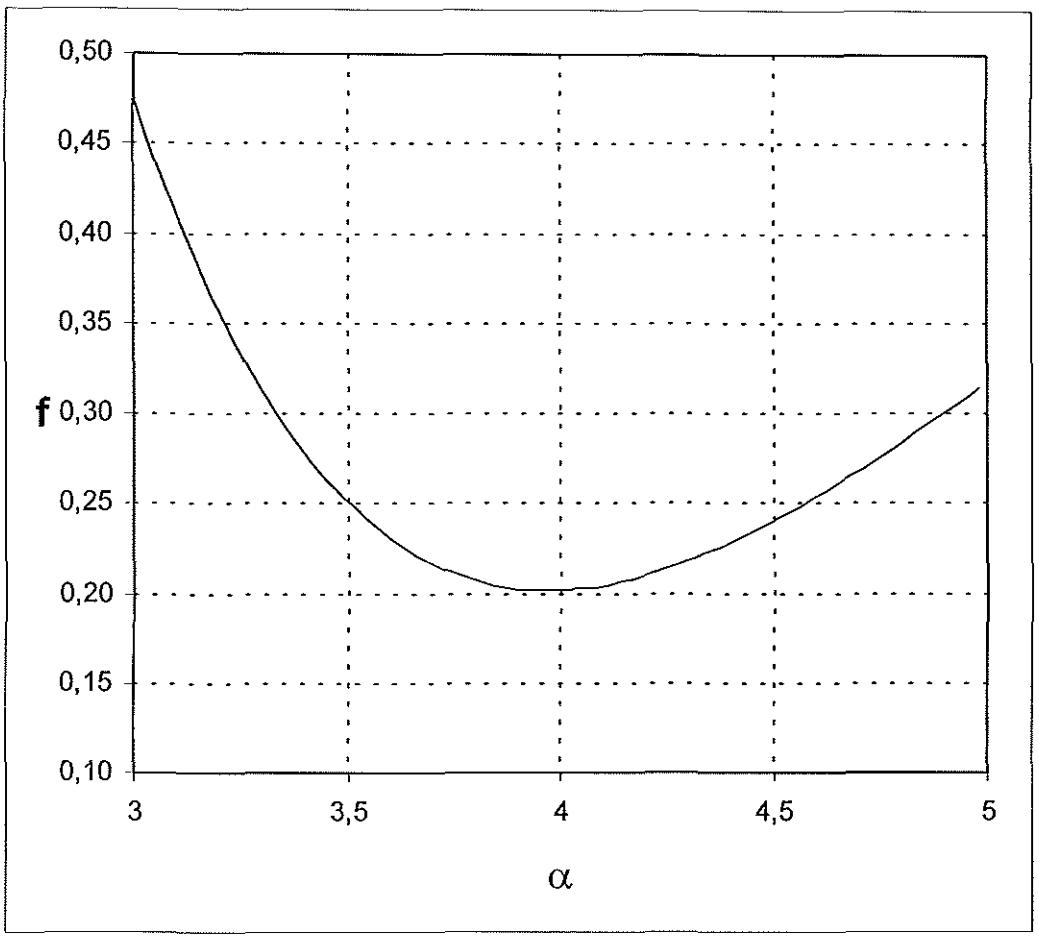

Figure 3

Altitude-95 (km)	*Density Law * ($1.0 \times E{+}31z^{-3}$)*	*Density * Initial Guess*	*Density * First Step Iter.*	*Density * Second Step Iter.*
38.8	171.2584	171.4297	171.3456	171.2635
50.1	79.2864	79.3657	79.3340	79.3241
61.5	42.9753	43.0182	43.0100	42.9800
72.9	25.8448	25.8706	25.8660	25.8468
84.2	16.7322	16.7490	16.7473	16.7331
95.6	11.4447	11.4561	11.4532	11.4482
107.0	8.1700	8.1781	8.1759	8.1720
118.3	6.0345	6.0406	6.0380	6.0350
129.7	4.5830	4.5876	4.5859	4.5848
141.1	3.5620	3.5656	3.5655	3.5624
152.4	2.8231	2.8259	2.8247	2.8233
163.8	2.2752	2.2775	2.2774	2.2761
175.2	1.8603	1.8622	1.8619	1.8609
186.5	1.5406	1.5421	1.5415	1.5410
197.9	1.2901	1.2913	1.2911	1.2905

** Density in 10^{15} m^{-3}, z in km.*

Table 1